

Cochlear imaging in the era of cochlear implantation

From silence to sound

Colophon

About the cover: The cover was designed and drawn by Dr. Jürgen Verbist.

As one of the most famous severely hearing impaired people the world has known, Ludwig van Beethoven was chosen for the illustration. The music, "Freudvoll und Leidvoll", juxtaposes his agony of deafness and the present day joy of hearing in recipients of cochlear implants. The bars represent the evolution of the treatment for sensorineural hearing loss. Early attempts at sound amplification helped Beethoven to break through the silence. However, good understanding of speech was only achieved after the advent of cochlear implants. The challenge for the future is to improve perception of music, to enable the hearing impaired to enjoy Beethoven's masterpieces in all their beauty.

Cochlear imaging in the era of cochlear implantation: From silence to sound
Verbist, Berit

Lay out: Legatron Electronic Publishing, Rotterdam, The Netherlands

Printed by: Ipskamp Drukker, Enschede, The Netherlands

ISBN: 978-90-9025033-5

2010 B. Verbist, Leiden, The Netherlands

All rights reserved. No part of this publication may be reproduced or transmitted in any form or by any means, electronic or mechanical, including photocopying, recording, or any information storage and retrieval system, without permission in writing from the copyright owner.

Cochlear imaging in the era of cochlear implantation

From silence to sound

PROEFSCHRIFT

ter verkrijging van
de graad van Doctor aan de Universiteit Leiden,
op gezag van de Rector Magnificus prof. mr. P.F. van der Heijden,
volgens besluit van het College voor Promoties
te verdedigen op woensdag 10 februari 2010
klokke 16.15 uur

door

Berit Michaela Verbist

geboren te Tienen (België)
in 1970

Promotiecommissie

Promotores: Prof. Dr. Ir. J.H.M. Frijns
Prof. Dr. M.A. van Buchem

Co-promotor: Dr. Ir. J.J. Briaire

Overige Leden: Prof. Dr. A.A. Mancuso (University of Florida, USA)
Prof. Dr. R. Maroldi (University of Brescia, Italy)
Dr. J.J.S. Mulder (UMC, Nijmegen)

The publication of this thesis was financially supported by:

Advanced Bionics

de Nationale Hoorstichting/Sponsor Bingo Loterij

Foundation Imago

Medis medical imaging systems bv, Leiden

Stichting Atze Spoor Fonds

Toshiba Medical Systems Nederland

Aan mijn ouders

Table of Contents

Chapter 1	Introduction	9
Chapter 2	Multisection CT as a Valuable Tool in the Postoperative Assessment of Cochlear Implant Patients <i>American Journal of Neuroradiology 2005; 26: 424-429</i>	19
Chapter 3	Evaluation of 4 Multisection CT Systems in Postoperative Imaging of a Cochlear Implant: A Human Cadaver and Phantom Study <i>American Journal of Neuroradiology 2008; 29: 1382-88</i>	33
Chapter 4	Clinical Evaluation of the Clarion CII HiFocus 1 with and without Positioner <i>Ear & Hearing 2005; 26: 577-592</i>	53
Chapter 5	Consensus Panel on a Cochlear Coordinate System Applicable in Histological, Physiological and Radiological Studies of the Human Cochlea <i>Otology & Neurotology, in press</i>	87
Chapter 6	Cochlear Coordinates in Regard to Cochlear Implantation: a Clinically Individually Applicable 3-dimensional CT-based Method <i>Otology & Neurotology, in press</i>	107
Chapter 7	Autonomous Virtual Mobile Robot for 3-dimensional Medical Image Exploration: Application to Micro-CT Cochlear Images <i>Artificial Intelligence in Medicine 2008; 43: 1-15</i>	125

Chapter 8	Anatomic Considerations of Cochlear Morphology and its Implications for Insertion Trauma in Cochlear Implant Surgery <i>Otology & Neurotology 2009; 30(4): 471-7</i>	153
Chapter 9	Cochlear Morphometry based on 3-dimensional Image Exploration: a MicroCT-MSCT study	169
Chapter 10	Concluding remarks and future perspectives in regard to imaging	187
	Summary	193
	Samenvatting	199
	Curriculum Vitae	205

1

Introduction

Introduction

Treatment of hearing loss was for a long time limited to amplification of acoustic signals. Since the 17th century ear trumpets were widely used to provide passive amplification of sound and to direct sound to the ear, hereby improving the signal to noise ratio. Over the years ear trumpets became more refined by experimenting with shapes and acoustic properties of different materials, but the amplification abilities were not always sufficient to enable persons to engage in conversations or listen to music again. One of the famous users of ear trumpets was Ludwig van Beethoven, who received a selection created for him by the Czech Johann Nepomuk Mälzel, the inventor of the metronome and the panharmonicum. For a short time they were spectacularly successful, but as his deafness worsened their amplification of sound became useless to him. And so it was yet another disappointment in Beethovens struggle to overcome the loss of his hearing sense. A loss, that had led him to live his life in fear, emotional disarray, increasing isolation, and self-neglect. [1]

... I have been hopelessly afflicted, made worse by senseless physicians, from year to year deceived with hopes of improvement, finally compelled to face the prospect of a lasting malady (whose cure will take years or, perhaps, be impossible).

L v Beethoven, Heiligenstaedter Testament

The advent of electricity had a major impact on the development of hearing aids. Alexander Graham Bell was one of the first to investigate the use of electricity for deaf people. Growing up in a family of authorities in elocution who were involved in education of deaf-mute children and deeply affected by the progressive, profound hearing loss of his mother, Alexander Graham Bell became a teacher for the deaf himself and devoted much of his experimental work on the transmission of sound. He has been credited for developing the first hearing aid in 1872, but he never patented this earphone. Further developments however led to the invention of the telephone, a device that could transmit speech electrically and contained the basic elements needed for a hearing aid that electronically amplifies sound.

After innumerable failures I finally uncovered the principle for which I was searching, and I was astounded at its simplicity. I was still more astounded to discover the principle I had revealed not only beneficial in the construction of a mechanical hearing aid, but it served as well as means of sending the sound of the voice over a wire.

AG Bell

Over the last 2 centuries the development of hearing aids has continued and nowadays hearing loss can be treated with small, practically invisible digital processing instruments with electronic characteristics individually suited to a particular type of hearing loss. However, once the damage to the (inner) ear is too large amplification of sound waves will no longer result in neural signals. In that case another approach is required.

Although Volta reported that direct electrical stimulation of the auditory nerve could evoke auditory sensations in humans as early as 1790, techniques to bypass the damaged ear have only been extensively explored since the late 1950s. Count Alessandro Volta had described the hearing experience evoked by two metal rods placed into his ear canals and connected to a battery as “a boom within the head “ and then a sound “a kind of crackling, jerking or bubbling as if some dough or thick stuff was boiling”. He immediately terminated the experiment and never repeated it. [2] However it sparked interest in crude applications of electric stimulation to improve hearing all over Europe for the following centuries. Along the way researchers learned more about the function of the cochlea and its electrical stimulation, but for a long time the hearing sensations were not satisfactory.

Djourno and Eyries adopted the idea that localized stimulation of the nerve fibers is required and in 1957 they inserted a first implant by placing a wire on an auditory nerve, exposed after cholesteatoma surgery. The patient was able to sense environmental sounds, discriminate amongst large changes in frequencies below 1000 Hz, developed limited recognition of common words and improved speech-reading capabilities. The implant failed after several months due to electrode fracture and also the reimplanted device ceased working after some months. [3] Once their work came under the attention of William F House of the House Ear institute in Los Angeles, he was inspired to develop an implant to be inserted in the (deaf) cochlea and stimulate the cochlea at different positions. [4] After testing many different systems of stimulation of this five-wire electrode, the same signal was put into all electrodes. This finally led to the

development of a single channel implant. [5] These developments paved the way to worldwide research on cochlear implantation, [6,7] although skepticism and criticism toward the aim to restore inner ear function was widespread. [8]

Due to endurance of early pioneers and the report of tests conducted in single-electrode cochlear implantees by Bilger in 1977 the benefits of cochlear implantation became recognized. Funding for research, including human studies substantially increased, albeit expectations of their performance were modest.

“... although the subjects could not understand speech through their prosthesis, they did score significantly higher on tests of lipreading and recognition of environmental sounds with their prosthesis activated than without them”

Bilger [9]

This instigated further research and thanks to investigations and developments in the fields of medicine – in particular neurotology-, bio engineering, signal processing, speech science and psychophysics cochlear implant development has taken a huge leap forward in the last 3 decades and has made cochlear implantation common, accepted clinical practice. [10] Multichannel systems (figure 1) replaced the single channel electrode, new and highly effective processing strategies were introduced, electrode designs were refined and rehabilitation programmes for implantees were installed. These developments have improved outcome such that an average cochlear implant patient nowadays reaches high levels of word recognition, open set speech recognition and even the ability to use the phone.

The cochlear implant is the most successful of all neural prostheses developed to date. It is the most effective prosthesis in terms of restoration of function, and the people who have received a cochlear implant outnumber the recipients of other types of neural prostheses by orders of magnitude.

Wilson BS [11]

Due to this successful evolution criteria for cochlear implant candidacy expanded and new challenges had to be faced to meet the growing expectations in regard to outcome.

Whereas in the early days, when only awareness for environmental sound and improvement of lip-reading was expected from cochlear implants, only adults with

postlingual bilateral profound sensorineural hearing loss or deafness were suitable candidates, nowadays, also prelingually deaf children are implanted. Malformed inner ears or partially obliterated cochleas are no longer considered absolute contraindications for implantation. For the latter even special electrodes (double array implant) have been developed. [12] To better approach normal hearing bilateral cochlear implantation has been performed and was shown to provide modest improvements in sound localization and speech perception, especially in noisy environments. A current area of development is combined electro-acoustic stimulation (EAS) in people with some residual hearing. [13] These people seem to benefit from a short implant stimulating high and middle frequencies electrically, while sparing the natural sound perceptions from residual low frequency hearing. Another important issue under investigation is music perception. So far the appreciation of music by cochlear implant users is generally low. [14] Improvements in the representation of pitch and information concerning the perception of timbre might not only lead to musical enjoyment, but it is also essential for the numerous tonal languages that are spoken worldwide, most commonly in East-Asia, sub-saharan Africa and by natives in North- and South America.

The fact that healthy people without or with residual hearing and children are now subjected to this invasive procedure poses high demands to all those involved in the treatment. Especially in relation to the possibility of a need for re-implantation after a number of years – be it due to device failure or because of new developments – and in cases of EAS the risk for insertion trauma is a major concern. In particular, electrode design must combine efficiency and safety and surgical skills must meet the need for atraumatic insertion.

To further investigate these complex issues and to conquer these new challenges a continuous multidisciplinary approach involving different fields of medicine, engineering, speech science and neuroscience will be required. One of the specialties that may contribute to this is radiology. Better insights in the working of cochlear implants on the one side and technical developments in medical imaging on the other side have transformed the role of imaging. Having the potential to provide an objective measure it will play a role both in research and for individual, patient based assessment of cochlear implant patients. The latter includes postoperative evaluation and preoperative selection of suitable candidates.



Figure 1: a) Schematic drawing of a cochlear implant. A cochlear implant consists of an externally worn speech processor and a microphone. The speech processor filters, analyzes and converts the auditory signals captured by the microphone to a digital code. A head piece containing a transmitting coil sends the signal from the speech processor to a subcutaneous implanted receiver to which it is magnetically attached. The receiver contains electronics to decode the signals and generate electrical stimuli. An electrode array is connected to this receiver and inserted into the scala tympani of the cochlea. The electrical stimuli sent to the electrode array will bypass the damaged parts of the cochlea and directly stimulate the auditory nerve. In multichannel arrays the electrode array contains several electrode contacts to ensure well directed stimulation of the tonotopically organized cochlea. b) Cochlear implant (Advanced Bionics HiRes 90k and Auria speech processor). The external and internal components of the implant are shown. The behind the ear part contains the speech processor and a built-in microphone. Alternatively a body worn processor can be used. Implants of other manufacturers have a slightly different appearance, but contain the same components.

In postoperative imaging it no longer suffices to solely confirm intracochlear positioning of a cochlear implant and report eventual breakage of the electrode lead. The study of frequency mapping – the relationship between the perceived frequency and the location of maximal excitation within the tonotopically organized cochlea – requires a more precise evaluation of implant positioning. To evaluate insertion trauma, damage to fine

intracochlear anatomic structures should be made visible. This information is of great value to the surgeon who gets direct feedback on his operation technique, which is especially useful in difficult cases, such as congenital malformed inner ear, or when a new electrode design is used, such as a double array implant in ossifying labyrinthitis.

Preoperative imaging should provide optimal information on the anatomy with its normal variances and pathology of the temporal bone, as well as information on the auditory pathway. The anatomic relations of the middle ear will influence the surgical approach. Precise knowledge of the cochlear anatomy and condition is helpful to individually optimize implantation in regard to electrode design and surgical placement.

This thesis describes the study of cochlear imaging in regard to cochlear implantation.

In **Chapter 2** the potential of multisection computer tomography (MSCT) scan for postoperative imaging of cochlear implants is investigated; a data acquisition protocol is introduced and its value is illustrated in 3 cases.

Chapter 3 evaluates the performance of MSCT systems of 4 different vendors in postoperative imaging of cochlear implants. The visibility of cochlear structures and the electrode array of the cochlear implant were assessed in a human cadaver temporal bone. Quantitative assessment of electrode contact positioning was performed in a phantom study. The spatial resolution of the scanner was evaluated with a point spread function phantom.

Chapter 4 describes the application of postoperative MSCT imaging as an objective measure to study differences in outcome between patient populations who received different electrode designs. A perimodiolar design is thought to be beneficial for speech perception. The clinical outcomes concerning speech perception of 25 patients who received the Clarion CII HiFocus 1 with a positioner (perimodiolar) and 20 patients without a positioner were linked to the intrascalar position and insertion depth, measured on CT and to stimulation levels and intracochlear conductivity pathways.

Chapter 5 presents the results of 2 international consensus meetings held by a panel of researchers with backgrounds in the various fields involved in cochlear implantation and representatives of the different manufacturers of cochlear implants. The aim was to search for an objective cochlear framework, for evaluation of the cochlear anatomy and description of the position of an implanted cochlear implant electrode. The framework should allow accurate comparisons between combinations of previous and forthcoming scientific and clinical studies.

Chapter 6 describes a CT based cochlear coordinate system that fulfills the requirements set by the consensus panel reported in chapter 4, which is easily applicable in individual clinical patients.

In **chapter 7** a method for non invasive measurement of cochlear dimensions is introduced. An autonomous virtual mobile robot (AVMR) was developed for three-dimensional (3D) exploration of unknown tubular-like structures in 3D images. After validation on synthetic environments the AVMR was applied to 8 micro-CT datasets of cochleae. Length and diameter measurements were obtained and compared to manual delineations.

In **chapter 8** the 3 dimensional anatomy of the cochlear spiral is evaluated based on a modification of the method described in chapter 7. The findings in micro CT scans of 8 human temporal bones are correlated to locations of insertion trauma as reported in literature.

Chapter 9 describes cochlear measurements in clinical MSCT scans of 8 isolated human temporal bones performed with above mentioned automatic approach, based on state-of-the-art image processing algorithms. Estimations of cochlear length and size of the scala tympani were compared to measurements on microCT scans of the same temporal bones.

In **chapter 10** concluding remarks are given and the potential role of imaging in regard to cochlear implant research is reflected upon.

References

1. Kubba AK and Young M. Ludwig van Beethoven: A medical biography. *Lancet* 1996, 347; 167-170
2. Volta A. On the electricity excited by mere contact of conducting substances of different kinds, *Royal Soc Philos Trans* 1800, 90; 403-431.
3. Djourno A., Eyries C. Auditory prosthesis by means of a distant electrical stimulation of the sensory nerve with the use of an indwelt coiling. *Presse Med* 1957, 65; 1417.
4. Doyle JH, Doyal JB and Turnbull FM. Electrical stimulation of the eighth cranial nerve. *Arch Otolaryngol* 1964, 80; 388-391.
5. House WF, Berliner KI. Safety and efficacy of the House/M cochlear implant in profoundly deaf adults. *Otolaryngol Clin North Am* 1986, 19: 275-86.
6. Blume SS. Sources of Medical Technology: Universities and Industry, National Academy Press, 1995, chapter Cochlear Implantation: Establishing Clinical Feasibility, 1957-1982.
7. Fourcin A.J, Rosen SM, Moore BC, Douek E E, Clarke GP, Dodson H, Bannister LH. External electrical stimulation of the cochlea: clinical, psychophysical, speech-perceptual and histological findings. *Br J Audiol* 1979, 13(3); 85-107.
8. Kiang NYS, Moxon EC. Physiological considerations in artificial stimulation of the inner ear. *Ann Otol Rhinol Laryngol* 1972, 81(5); 714-730.
9. Bilger RC, Black FO, Hopkinson NT, Myers EN. Implanted auditory prosthesis: an evaluation of subjects presently fitted with cochlear implants. *Trans Sect Otolaryngol Am Acad Ophthalmol Otolaryngol*. 1977, 84(4 Pt 1): 677-82.
10. In "Summary of safety and effectiveness data", FDA: PMA nr P830069, 26 Nov 1984
11. Wilson BS, Dorman MF. Cochlear implants: current designs and future possibilities. *J Rehabil Res Dev*. 2008;45(5):695-730
12. Lenarz T, Lesinski-Schiedat A, Weber BP, Issing PR, Frohne C, Büchner A, Battmer RD, Parker J, von Wallenberg E. The nucleus double array cochlear implant: a new concept for the obliterated cochlea. *Otol Neurotol*. 2001 Jan;22(1):24-32.
13. James C, Albegger K, Battmer R, Burdo S, Deggouj N, Deguine O, Dillier N, Gersdorff M, Laszig R, Lenarz T, Rodriguez MM, Mondain M, Offeciers E, Macías AR, Ramsden R, Sterkers O, Von Wallenberg E, Weber B, Fraysse B. Preservation of residual hearing with cochlear implantation: how and why. *Acta Otolaryngol*. 2005, 125(5):481-91.
14. Drennan WR, Rubinstein JT. Music perception in cochlear implant users and its relationship with psychophysical capabilities. *Rehabil Res Dev*. 2008;45(5):779-89.

2

Multisection CT as a Valuable Tool in the Postoperative Assessment of Cochlear Implant Patients

BM Verbist, JHM Frijns, J Geleijns, MA van Buchem

American Journal of Neuroradiology 2005; 26: 424-429

Summary

A data acquisition protocol for postoperative imaging of cochlear implants by using multisection CT (MSCT) is described. The improved image quality of MSCT allows assessment of the precise intracochlear position of the electrode array and visualization of individual electrode contacts. Such images can aid in fitting the speech processor, especially in difficult cases.

Introduction

Cochlear implantation has become widely available and permits successful treatment of severe or profound sensorineural hearing loss in patients who do not receive adequate benefit from hearing aids. The American Medical Association and the American Academy of Otolaryngology – Head and Neck Surgery have recognized that the cochlear implant is a standard treatment for patients with profound sensorineural hearing loss. [1] An electrode array is inserted into the scala tympani for direct electrical stimulation of spiral ganglion cells of the auditory nerve, thereby bypassing damaged hair cells. Postoperative imaging is performed to confirm intracochlear positioning and integrity of the electrode array and detection of electrode kinking. Plain radiographs, which are inexpensive and not difficult to obtain, are most commonly used for this assessment.

New insights into the mechanism of electrical stimulation that produces hearing have led to new developments in electrode design. The new generation of cochlear implants is designed to be in a perimodiolar position rather than lying along the outer wall of the cochlea. The precurved design of perimodiolar electrodes (also called “modiolus-hugging” electrodes) brings the electrode contacts somewhat closer to the modiolus and thus closer to the spiral ganglion cells than earlier straight designs that follow the outer wall of the cochlea. The closer proximity of the contacts to the nerve fibers to be stimulated is believed to have beneficial effects on stimulus thresholds, power consumption, spatial selectivity, and dynamic range. [2]

Thus, there is a growing interest in precisely documenting the position of the individual electrode contacts in relation to cochlear structures and the insertion depth of the electrode array. Another important issue is the documentation of potential insertion trauma, such as perforation of the basilar membrane, which may lead to degeneration of neuronal elements and scar or bone formation within the cochlea.

Several imaging techniques have been described to achieve this goal in both temporal bone studies and clinical practice. They include conventional radiography (“cochlear view”), [3] (video) fluoroscopy, [4,5] phase-contrast radiography, [6] cone beam CT, [7] fusion of conventional radiographs and CT images by using either electrodes as fiducial markers [8] or stereophotogrammetry (by using a stereo pair of radiographs to compute the 3D locations of individual electrodes), [9] and spiral CT. [10]

Conventional radiography can resolve each electrode contact, but it cannot provide 3D details. Whereas conventional radiography is based on absorption contrast, phase-

contrast radiography is based on phase or refraction effects. A microfocus radiographic tube source is used to ensure a sufficiently high level of spatial coherence of the radiograph. Large projection distances allow further wave propagation and interference effects to occur, resulting in observable changes in intensity (phase contrast) in the image plane. The images provide better visualization of anatomic details of the inner ear and of the structure of the electrode array. [7] Both phase-contrast radiography and cone beam CT, however, have been used successfully *in vitro* only and are not likely to be clinically relevant alternatives in the near future. The main disadvantage of CT in the postoperative assessment of a cochlear implant is image degradation by partial voluming and metallic artifacts rendering individual electrodes indistinguishable. [3,8-10] By using multisection CT (MSCT), we produced *in vivo* images of cochlear implants on which individual electrode contacts can be distinguished. To the best of our knowledge, this is the first report of postoperative imaging of cochlear implants with such spatial detail made on a commercially available clinical scanner.

Imaging Technique

Data acquisition was performed on a MSCT imaging scanner (Aquilion 4, Toshiba Medical Systems Europe; Zoetermeer, the Netherlands) by using the following parameters: four times 0.5-mm section thickness; 0.5 seconds rotation time; 0.75 pitch factor; 120 kV tube voltage; 150 mA tube current; and a 240-mm scan field of view (FOV). Images with a nominal thickness of 0.5 mm were reconstructed by using a 0.3-mm reconstruction increment, 90-mm reconstruction FOV, 512 X 512 matrix, and high-resolution reconstruction algorithm (FC81). The radiation risk of the CT scan is best expressed by the effective dose. The effective dose of the used CT acquisition is about 0.8 mSv, which is well below the annual radiation exposure from natural sources. The dose to the eye lens is of no major concern. The estimated threshold for visual impairment (cataract) of the lens in the average human adult, expressed as the absorbed dose in the eye lens, is 5 Sv for a single exposure and 8 Sv for fractionated exposures. [11] Even repeated diagnostic CT scans do not approach such high levels of absorbed dose to the eye lens. The voxels produced with this technique are practically isotropic (voxel size, 0.47 X 0.47 X 0.50 mm), which allows reformations in any plane with virtually no loss in resolution. The images were transferred to a workstation running a software

package for postprocessing (Easy Vision; Philips, Best, the Netherlands) to generate 2D reformations and 3D reconstructions. Multiplanar reconstructions (MPRs) through the cochlea were made parallel to the basal turn of the cochlea and perpendicular to the modiolus and thus in the plane of the electrode array. A second set of MPRs was made perpendicular to the basal turn and parallel to the modiolus rendering coronal images of the scala tympani and vestibuli. These images might be helpful in the assessment of insertion trauma to the basilar membrane. Three-dimensional reconstructions were made by using a volume-rendering (VR) technique. Window width and window level were adjusted until both the cochlear tissues and the individual electrodes could be visualized.

Case Reports

Case 1

A 2.5-year-old girl with normal language development developed sudden profound sensorineural hearing loss following bacterial meningitis. She did not benefit from hearing aids, and within 6 months she presented with a delay in language development of 10-16 months. MR imaging and CT scanning of the temporal bone were performed. Partial obliteration of the cochleovestibular system due to ossification, more pronounced on the right side than on the left side, was seen. The diagnosis of ossifying labyrinthitis was made. On the basis of these findings, the patient was selected for cochlear implant surgery in the left ear.

Peroperatively fibrous and osseous tissue was removed from the scala tympani, and after several attempts, a Clarion CII cochlear implant (Advanced Bionics Corp., Sylmar, CA) with Hifocus I electrode array (figure 1) was fully inserted. The electrode array was brought into a perimodiolar position by secondary insertion of a so-called positioner, which could not be completely inserted.

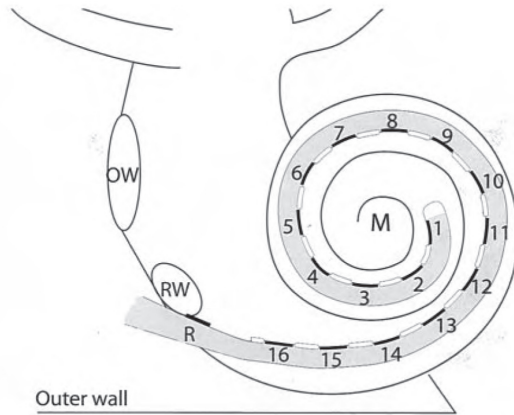


Figure 1. Schematic representation of a HiFocus I (Clarion CII Bionic ear) electrode array, which is inserted into the scala tympani via a cochleostomy near the round window niche (RW). The electrode array has a reference electrode (R) and 16 equidistantly spaced contacts (black lines), numbered from the tip of the electrode array to the basal end, which are facing the modiolus (M). They are positioned on a silastic carrier (gray) and are separated by silastic blebs (white lines). The oval window (OW) and outer wall of the cochlea (outer wall) are indicated.

Postoperative MSCT imaging was performed immediately after the surgery under the same anesthesia as used for the surgery. MPRs and volume-rendered images showed kinking of the tip of the electrode array (figure 2). Accordingly, the two most distal contacts were deprogrammed to anticipate problems in mapping. Because mapping of a cochlear implant is done on a subjective basis, which is difficult to obtain in children of this age, imaging provided essential information to optimize the function of the cochlear implant. Two years after the implantation, the girl's oral language development is within the range of normal for her age.

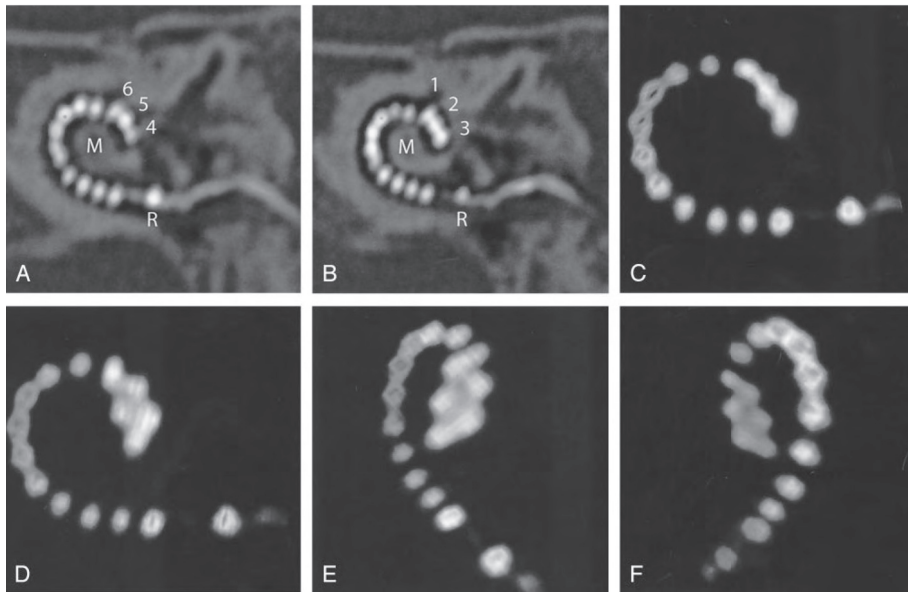


Figure 2. *Case 1.* **A** and **B**, Oblique MPRs of high resolution MSCT images in the plane of the electrode array demonstrate 16 electrode contacts within the scala tympani. The tip of the electrode (contacts 1-3) projects cranial to contacts 4-6, indicating kinking of the electrode array. **C-F**, 3D VR images confirm this finding. On conventional radiography (cochlear view) electrode contacts 1-6 would be superimposed on each other, as compared with image 2C. R indicates reference electrode; M: modiolus.

Case 2

A 25-year-old male patient presented with familial progressive sensorineural hearing loss resulting in postlingual severe deafness (average hearing loss at 1, 2, and 4 kHz, >115 dB). MR imaging and CT scanning of the temporal bone did not show any abnormalities. The patient received a Clarion CII cochlear implant with a Hifocus I electrode with positioner. During the operation, both the electrode array and the positioner could be inserted smoothly. Postoperative MSCT imaging was performed, and MPRs were obtained. The electrode contacts at the basal end of the array are lying in close proximity to the modiolus, confirming the expected medial displacement due to the use of a positioner (figure 3).

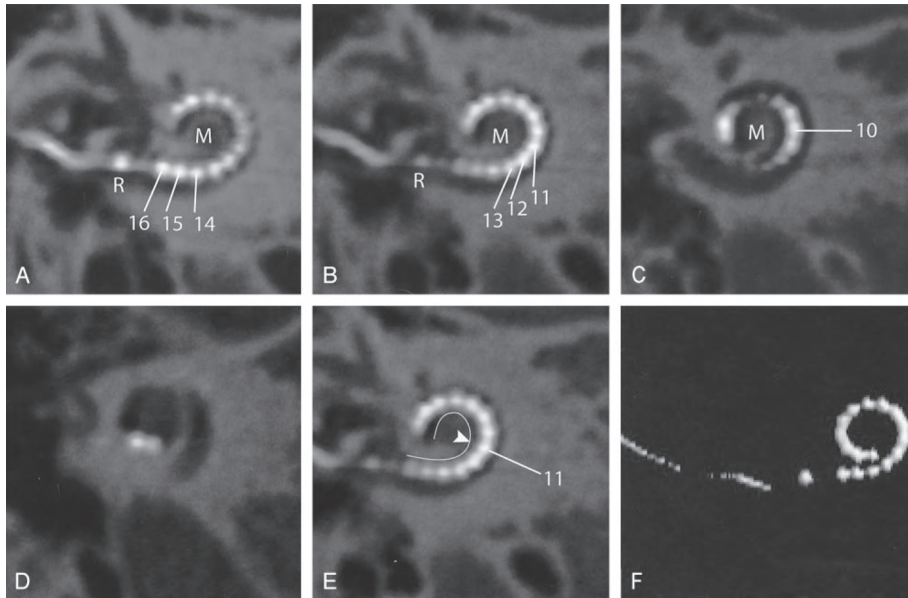


Figure 3. *Case 2.* **A-D**, Oblique multiplanar reformatting of high-resolution MSCT of a HiFocus I electrode array with positioner. The reference electrode (R) is positioned at the level of the cochleostomy. Sixteen individual contacts can be discerned. Contacts 16-12 are positioned in close proximity to the modiolus (M) because of the use of a positioner, which was secondarily inserted along the basal end of the electrode array. On its further course, the electrode array is positioned more laterally within the cochlear lumen. **E**, Same image as figure 2B; the modiolus contour is marked (white line). The more lateral position of the distal electrode contacts starting at electrode contact 11 (arrowhead) is shown more clearly. **F**, 3D VR.

To evaluate the postoperative performance with the implant, speech perception scores were measured in a free-field condition by using the standard CVC (consonant-vowel-consonant) word list (prerecorded female speaker) of the Dutch Society of Audiology at 65 dB SPL and compared with preoperative measurements. The test consists of CVC monosyllabic words, which are presented to the patient in a free-field condition. The score represents the percentage of correctly reproduced phonemes or words. [12] The average preoperative phoneme score was 0%. One year after implantation, the average phoneme and word scores were, respectively, 93.5% and 86%.

Case 3

The third case concerns a 65-year-old female patient with progressive sensorineural hearing loss. She had suffered from deafness for 45 years (average hearing loss at 1, 2, and 4 KHz, >120 dB). Preoperative CT and MR imaging showed no abnormalities within the temporal bones or on the auditory pathway. A Clarion CII cochlear implant with a Hifocus I electrode was inserted without the use of a positioner (because changes in design by the manufacturer). As a result, the proximal electrode array could not be placed in a perimodiolar position. After insertion, the electrode array tended to be pushed back, and only a shallow insertion could be achieved. Reformatted postoperative MSCT images clearly show that the electrode array is positioned along the lateral wall of the scala tympani over its entire length (figure 4).

Phoneme scores on the CVC word test in quiet (free field, sound only, 65 dB hearing loss) measured preoperatively and 1 year after implantation were, respectively, 0% and 86%, and the word score was 73%.

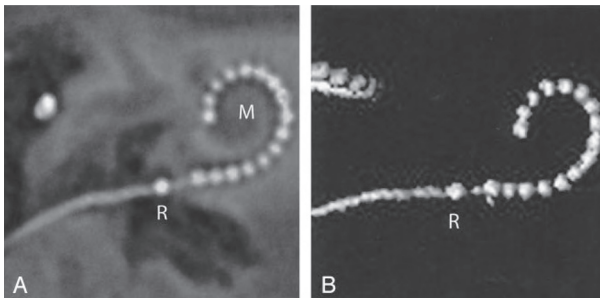


Figure 4. Case 3. **A**, Oblique multiplanar reformatting of high resolution MSCT of a HiFocus I electrode array without positioner. The reference electrode (R) projects proximal to the cochleostomy. All 16 electrode contacts are positioned within the cochlea. The electrode array courses along the lateral wall of the cochlear lumen over its entire length, leading to a less deep insertion than with the positioner (compare figure 3). **B**, On a VR image, a rather shallow insertion of the electrode can be seen. M, modiolus.

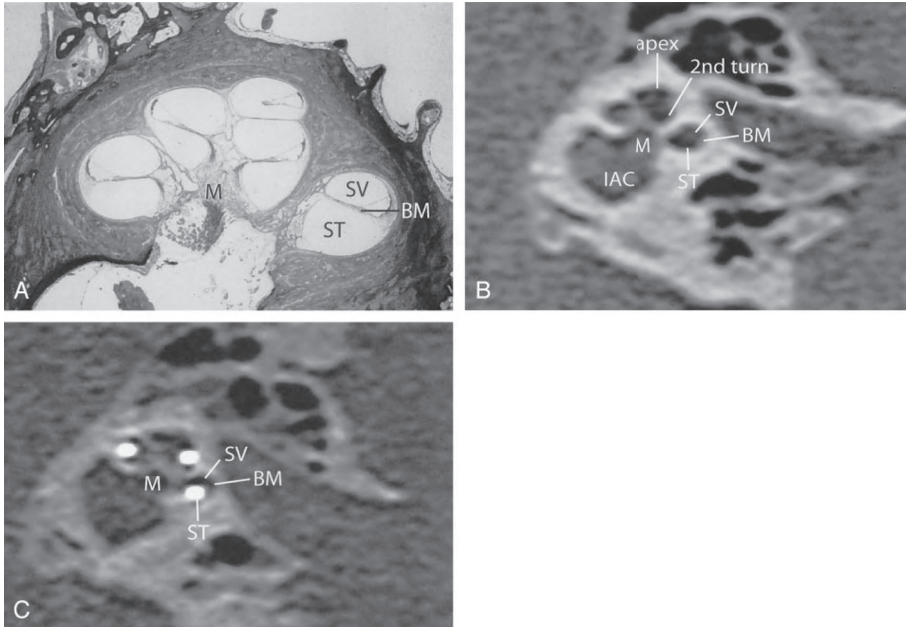


Figure 5. **A**, Midmodiolar cross-section of human cochlea. The basilar membrane (BM) separates the scala tympani (ST) and scala vestibuli (SV). **B**, An oblique coronal MPR of a preoperative MSCT at a midmodiolar level is shown. The scala tympani (ST), the scala vestibuli (SV) and the presumed level of the basilar membrane (BM) are indicated in the basal turn of the cochlea. 2nd turn indicates second turn of the cochlea; apex, apical turn of the cochlea, M, modiolus; IAC, internal auditory canal. **C**, MPR of a postoperative high-resolution MSCT image parallel to the modiolus and perpendicular to the basal turn of the cochlea. Although the basilar membrane (BM) itself cannot be visualized, the position of the electrode contacts does correspond with full insertion of the array in the scala tympani (ST).

Discussion

The patients presented in this report received a Clarion CII Bionic ear cochlear implant with a Hi-Focus I electrode array (in cases 1 and 2 combined with a positioner to achieve a perimodiolar position) (figure 1). This electrode array is one of the new generation cochlear implants, designed to place the stimulating contacts in close proximity to the spiral ganglion cells located within the modiolus. Preferably, postoperative assessment

of this implant should include documentation of the precise location of individual electrode contacts in relation to the modiolus as well as the insertion depth. In this technical note, a MSCT data acquisition protocol that allows detailed evaluation of the final intracochlear position of the electrode array and the individual electrode contacts is described.

To achieve good image quality on postoperative CT images as presented in this article, one has to deal with two problems. The most important one is the image degradation due to artifacts. For accurate visualization of the small electrode contacts and to reduce metallic artifacts, high-resolution scanning and a high-resolution reconstruction filter is required. The other problem is that only part of the electrode array is seen on each section.

The HiFocus I electrode array has 16 contacts, each measuring 0.4 X 0.5 mm with a center-to-center distance of 1.1 mm for neighboring contacts. In addition, there is a reference-contact about 2.5 mm basal to the array of the primary contacts. The contacts and the connecting leads are made of a platinum-iridium alloy (90-10%). To distinguish such small contacts an in-plane and cross-plane resolution of at least 2.5 line pairs per millimeter (lp/mm) is required. For separate visualization of neighboring contacts, a resolution of at least 1.1-1.2 lp/mm is required. The limiting resolution of scanners depends mainly on the scanner design, the reconstruction algorithm (determining mainly the in-plane resolution, measured in the *xy* plane), the smallest available section thickness and the *z* axis filtering algorithm (both determining cross-plane resolution, measured along the *z* axis).

MSCT imaging yields the maximum detail resolution available at present in a clinical setting and provides an (almost) isotropic voxel size when appropriate data acquisition protocols are used. The minimum section thickness of 0.5 mm, and the high-speed multisection cone-beam tomography reconstruction method (MUSCOT) used in our scanner, improve resolution in both the longitudinal and transverse direction. The in-plane visualization of details of 0.4-0.5 mm and cross-plane visualization of details of 0.5-0.7 mm, corresponding with, respectively, 1.0-1.25 lp/mm in plane and 0.7-1.0 lp/mm cross-plane, approaches the requirements for visualization of the individual contacts. Unfortunately, because of blooming, the actual shape of the electrodes cannot yet be visualized accurately. [13] Although we do not have experience with cochlear implants of other manufacturers we expect similar results due to similarity in dimensions and alloy. The multisection scanner used at our institution provides an acquisition configuration

of 4 X 0.5 mm and uses a high-resolution reconstruction algorithm. Other multisection scanners currently on the market provide a similar acquisition configuration, and further improvements are to be expected in the near future. Therefore, we expect similar results can be yielded with other CT scanners, provided a dedicated imaging protocol is used.

To solve the problem regarding the scan plane, reconstructions can be made to optimize the visualization of the electrode array. The quality of reconstructed images depends crucially upon the resolution of the cross-sectional source data. The (near) isotropic volumetric imaging available with MSCT allows one to reconstruct images in arbitrary planes (figures 2A, B, 3A-D, 4A, 5B, C) and to make 3D reconstructions of superior image quality (figures 2C-F, 3F, 4B). Two-dimensional reformations are a useful tool for comprehensive visualization of the electrode array within the complex architecture of the cochlea, because both the electrode contacts and small anatomic structures such as the modiolus and outer cochlear wall can be distinguished.

Oblique axial reformations, parallel to the basal turn of the cochlea and perpendicular to the modiolus, correspond to the plane of the electrode array. They provide a comprehensible image of the precise intracochlear position of the electrode array and its relation to the modiolus (figures 2-4). Accurate evaluation of the exact position of the electrode array might lead to a better understanding of the wide variability in fitting parameters (e.g., *T* levels) and for speech perception in cochlear implant recipients. This will have implications in the development and selection of speech-processing programs and improvement of insertion techniques and electrode design.

Insertion of a cochlear implant bears the risk of rupturing fine intracochlear structures, which might lead to further neuronal losses and osteoneogenesis. [14] Until now, assessment of insertion trauma has only been done by means of histologic studies [4,14,15] or *in vitro* temporal bone imaging. [4,6,7,14] On the basis of the findings in this study, MSCT might become a useful tool for *in vivo* examination of such peroperative intracochlear trauma. Oblique coronal images, reconstructed perpendicular to the basal turn of the cochlea and parallel to the modiolus, can be used for this assessment. Although the osseous spiral lamina and basilar membrane cannot be discerned on these images, the position of the electrode contacts indicates whether the array is situated in the scala tympani or in the scala vestibuli (figure 5). Although subtle traumatic lesions cannot be shown, this is a clear advantage over conventional radiographs and the obtained images are at least comparable to previously reported *in vitro* imaging with cone beam CT. [7]

More gross effects on the inserted array can be evaluated on 3D reformations by using a VR technique. The images are comparable to conventional radiographs but yield the possibility to view the electrode array under arbitrary angles. As shown in case 1, where two contacts were left out of the map (figure 2), imaging findings will influence programming.

Conclusion

The data acquisition protocol presented in this report enables visualization of both the individual contacts and anatomic details of the cochlea within the plane of the electrode array, thus providing useful information to optimize the function of the cochlear implant in individual patients. Until now, CT scanning in cochlear implant recipients was reserved for patients with suspected complications. The technological advances of MSCT might, however, lead to expansion of the clinical applications, provided that dedicated acquisition parameters are used.

References

1. NIH Consensus Statement. Cochlear implants in adults and children. NIH Consensus Development Conference. May 15–17, 1995;13:1–30
2. Frijns JHM, Briare JJ, De Laat JAPM, Grote JJ. Initial evaluation of the Clarion CII cochlear implant: speech perception and neural response imaging. *Ear Hear* 2002;23:184–197
3. Xu J, Xu SA, Cohen LT, Clark GM. Cochlear view: postoperative radiography for cochlear implantation. *Am J Otol* 2000;21:49–56
4. Roland JT, Fishman AJ, Alexiades G, Cohen NL. Electrode to modiulus proximity: a fluoroscopic and histologic analysis. *Am J Otol* 2000;21:218–225
5. Balkany TJ, Eshraghi AA, Yang N. Modiolar proximity of three perimodiolar cochlear implant electrodes. *Acta Otolaryngol* 2002; 122:363–369
6. Xu J, Stevenson AW, Gao DC, et al. The role of radiographic phase-contrast imaging in the development of intracochlear electrode arrays. *Otol Neurotol* 2001;22:862–868
7. Husstedt HW, Aschendorff A, Richter B, et al. Nondestructive three-dimensional analysis of electrode to modiulus proximity. *Otol Neurotol* 2002;23:49–52
8. Whiting BR, Bae KT, Skinner MW. Cochlear implants: three-dimensional localization by means of coregistration of CT and conventional radiographs. *Radiology* 2001;221:543–549
9. Yang SY, Wang G, Skinner MW, et al. Localization of cochlear implant: electrodes in radiographs. *Med Phys* 2000;27:775–777
10. Ketten DR, Vannier MW, Skinner MW, et al. In vivo measures of cochlear length and insertion depth of nucleus cochlear implant electrode arrays. *Ann Otol Rhinol Laryngol* 1998;107:1–16
11. International Commission on Radiological Protection. Recommendations of the International Commission on Radiological Protection. ICRP publication 60. Oxford: Pergamon Press;1990
12. Bosman AJ, Smoorenburg GF. Intelligibility of Dutch CVC syllables and sentences for listeners with normal hearing and with three types of hearing impairment. *Audiology* 1995;34:260–284
13. Hsieh J. Computed tomography: principles, design, artifacts, and recent advances. Bellingham: SPIE—the International Society for Optical Engineering;2003:1–388
14. Richter B, Jaekel K, Aschendorff A, et al. Cochlear structures after implantation of a perimodiolar electrode array. *Laryngoscope* 2001;111:837–843
15. Tykocinski M, Cohen LT, Pyman BC, et al. Comparison of electrode position in the human cochlea using various perimodiolar electrode arrays. *Am J Otol* 2000;21:205–211

3

Evaluation of 4 Multisection CT Systems in Postoperative Imaging of a Cochlear Implant: A Human Cadaver and Phantom Study

BM Verbist, RMS Joemai, WM Teeuwisse, WJH Veldkamp, J Geleijns, JHM Frijns

American Journal of Neuroradiology 2008; 29: 1382-88

Abstract

Background & Purpose: Postoperative imaging of cochlear implants (CIs) needs to provide detailed information on localization of the electrode array. We evaluate visualization of a HiFocus1J array and accuracy of measurements of electrode positions for acquisitions with 64-section CT scanners of 4 major CT systems (Toshiba Aquilion-64, Philips Brilliance-64, GE LightSpeed-64, and Siemens Sensation-64).

Materials & Methods; An implanted human cadaver temporal bone, a polymethyl-metacrylaat (PMMA) phantom containing a CI and a point spread function (PSF) phantom were scanned. In the human cadaver temporal bone, the visibility of cochlear structures and electrode array were assessed by using a visual analogue scale (VAS). Statistical analysis was performed with a paired 2-tailed Student *t* test with significant level set to .008 after Bonferroni correction. Distinction of individual electrode contacts was quantitatively evaluated. Quantitative assessment of electrode contact positions was achieved with the PMMA phantom by measurement of the displacement. In addition, PSF was measured to evaluate spatial resolution performance of the CT scanners.

Results: VAS scores were significantly lower for Brilliance-64 and LightSpeed-64 compared with Aquilion-64 and Sensation-64. Displacement of electrode contacts ranged from 0.05 to 0.14 mm on Aquilion-64, 0.07 to 0.16 mm on Brilliance-64, 0.07 to 0.61 mm on LightSpeed-64, and 0.03 to 0.13 mm on Sensation-64. PSF measurements show an in plane and longitudinal resolution varying from 0.48 to 0.68 mm and of 0.70 to 0.98 mm, respectively, over the 4 scanners.

Conclusion: According to PSF results, electrode contacts of the studied CI can be visualized separately on all of the studied scanners unless curvature causes intercontact-spacing narrowing. Assessment of visibility of CI and electrode contact positions, however, varies between scanners.

Introduction

Multisection CT (MSCT) has proven its efficacy in the postoperative imaging of cochlear implant (CI) patients. [1,2] Like conventional X-ray, CT confirms the intracochlear position of the implant. It has also been shown that malpositioning and kinking can be detected by CT imaging. [1,3-5] In addition, MSCT provides important information on other clinical or research-based issues. By visualizing not only the individual electrode contacts but also the cochlear morphology and fine anatomic structures, valuable information is gained. The positioning of an electrode array, as well as the individual electrode contact-to-modiolus distance, can be assessed. This yields objective measurements facilitating the evaluation of differences in outcome (speech perception) after implantation of different types of electrode arrays. [6,7] New electrode designs, such as the split electrode, can be thoroughly examined. [8] The number of functional electrode contacts and an antegrade or retrograde course of the second array can be determined. Recently, the optimal size and spacing of electrode contacts for a new type of split array were determined with the help of such CT imaging (unpublished data). In addition, in cases of congenital cochleovestibular malformation, CT enables assessment of the surgical result with regard to the number of functional electrode contacts and rotation of the array. In this way, postoperative imaging by MSCT contributes to improvements of implant fitting, development of electrode designs, and assessment of surgical techniques.

Still, reservations toward the application of CT in these patients are widespread. [9-12] Concerns with regard to suboptimal image quality because of metallic artifacts exist, and it is not clear whether recent models of MSCT scanners and applied acquisition protocols produce adequate image quality for reliable assessment of CI placement.

In this study, the visualization of a HiFocus1J electrode array (Advanced Bionics, Sylmar, Calif) and the accuracy of measurements of electrode positions for acquisitions with 64-section CT scanners of 4 major CT systems (Aquilion-64 [Toshiba Medical Systems, Otawara, Japan], Brilliance-64 [Philips Medical Systems, Best, the Netherlands], LightSpeed-64 [GE Healthcare, Milwaukee, Wis], and Sensation-64 [Siemens Medical Solutions Forchheim, Germany]) were evaluated in a human cadaver temporal bone and in a polymethylmetacrylaat (PMMA) phantom.

Materials and Methods

MSCT scans were performed on an implanted human cadaver temporal bone to evaluate the appearance of clinical images. To analyze the performance and resolution of 4 different 64-section CT scanners, point spread function (PSF) was measured for each CT scanner, and images of a CI embedded in a polymethylmetacrylaat (PMMA) phantom of the basal turn of the cochlea were acquired.

Data Acquisition and Image Reconstruction

Scans were performed on 4 64-section systems: Aquilion-64, Brilliance-64, Light-Speed-64, and Sensation-64. All of the manufacturers were asked to provide a specific, optimized protocol for inner ear CI imaging. The protocols were established by the manufacturers own application specialist or by an experienced technician under the authority of the manufacturer and included both an acquisition and a reconstruction protocol. The specialists were present during the scans and able to vary the parameters to obtain an optimal protocol. These protocols were applied for the implanted human cadaver temporal bone, PSF and PMMA phantom.

The main protocol parameters are listed in Table 1. Effective doses were calculated for all provided protocols with ImPACT CT patient Dosimetry calculator (version 0.99x; available at www.impactscan.org) and are included in Table 1. All of the scans were repeated 3 times. Between the scans, both the object and the table were repositioned. A marker was fixed on each object to establish the same positioning in relation to the laser of the gantry in each scan and on each scanner.

The reconstruction fields of view (FOVs) were predefined for each object. A small image reconstruction interval was applied for the PSF phantom (0.1 mm on all of the systems) to accurately calculate the PSF.

CI Electrode

A HiFocus1J electrode array, as is used in clinical practice, was implanted in the cadaver temporal bone and placed in the PMMA phantom. This electrode array consists of 16 electrode contacts, each measuring 0.4 x 0.5 mm with a contact spacing of 1.1 mm. The contacts are numbered from the tip of the electrode toward the base.

Table I. Acquisition and reconstruction protocols and effective radiation dose for cochlear implant imaging on 64-section scanners.

	Aquilion 64	Brilliance 64	LightSpeed 64	Sensation 64
Acquisition Protocol				
Tube Voltage (kV)	120	140	140	120
Tube Current (mA)	200	200	335	135
Beam Collimation (mm)	4 x 0.5	2 x 0.55	32 x 0.625	12 x 0.6
Pitch	0.75	0.5	0.531	0.45
Rotation time (s)	0.5	0.5	0.6	1.0
Scan FOV	240	500	320	500
Dose of Acquisition protocol				
Effective dose (mSv)	1.4	2.0	1.8	1.3
Reconstruction Protocol				
Section thickness (mm)	0.5	0.55	0.6	0.6
Section interval (mm)	0.3	0.3	0.3	0.3
Kernel	FC84	Filter D	BonePlus	U90u
Reconstruction matrix	512 ²	768 ²	512 ²	512 ²
Recon FOV PMMA phantom (mm)				100
Recon FOV PSF phantom (mm)				50
Recon FOV cadaver head (mm)				80

Note: FOV indicates field of view; PMMA, polymethylmethacrylate; PSF, point spread function

***Ex Vivo* Study**

To mimic clinical conditions, a human cadaver temporal bone was scanned. It consisted of a 9 x 9 x 6 cm³ (anteroposterior, cranial-caudal, and right-left, respectively) segment of a human head, with the petrous bone in its center and including the auricle. The cadaver head was formalin fixed. The HiFocus1J electrode implant was inserted by an experienced ear, nose, and throat (ENT) surgeon, following standard operating procedures. During insertion, an unusual resistance was felt. Contrary to clinical practice, the electrode was inserted further, resulting in a slight kinking of the array in the third quadrant of the cochlea (figure 1).

To prevent postimplantation displacement, the electrode was fixed by a single stitch and glue. To prevent CT artifacts from abrupt changes in attenuation, the cadaver temporal bone was placed in a 16 x 16 x 9 cm³ plastic container, submerged in gelatin (Merck, Darmstadt, Germany), and entrapped air was evacuated in a vacuum chamber. Gelatin

was chosen to increase the attenuation of the human cadaver temporal bone to resemble the clinical setting. Axial CT images of the cadaver temporal bone were processed on a Vitrea work station (Vitrea 2; Vital Images, Minnetonka, Minn) according to the clinical protocol: multiplanar reconstructions (MPRs) perpendicular, as well as parallel, to the modiolar axis were made with contiguous 0.5mm sections and subsequently stored. These MPRs were evaluated by 6 observers, 5 radiologists (a head and neck radiologist with 6 years of experience and 5 general radiologists with experience level 1-3 years), and 1 ENT surgeon with a 2-year experience in temporal bone imaging. They were blinded for the scanner brand. All of the images were presented in a random order. Window width and level could be adjusted by the observers. Postoperative imaging of CIs should provide on information about the precise localization of the implant and its individual contacts, as well as the presence of complications. To examine whether the different scanners can provide this information, the visibility of the course and localization of the electrode array, the presence of a complication (kinking), and the visibility of the inner and outer wall of the basal turn of the cochlea per quadrant were assessed by using a visual analogue scale (VAS) from 0 to 10. The distinction of individual electrode contacts was evaluated by using the following quantitative score. If an electrode contact could not be distinguished from the previous or following contact, a score of 0 was given. If the electrode contact was clearly separated from its neighboring contacts, a score of 2 was given. In case electrode contacts could be differentiated at the surface but not in the center, a score of 1 was given (figure 1). For each observer a cumulative score per scan was calculated by summation of the scores of the 16 contacts. Thus, for each electrode array, a score between 0 and 32 was calculated first on images perpendicular to the modiolar axis and, in addition, on images parallel to the modiolar axis. Mean values and SDs of all measurements were calculated. To investigate statistical significant differences, VAS results were analyzed by a paired 2-tailed Student *t* test. To reduce type I errors in multiple comparisons, a Bonferroni correction (for $n=6$ comparisons) was applied. A *p* value lower than .008 was considered significant for each comparison to maintain a global .05 significance level.

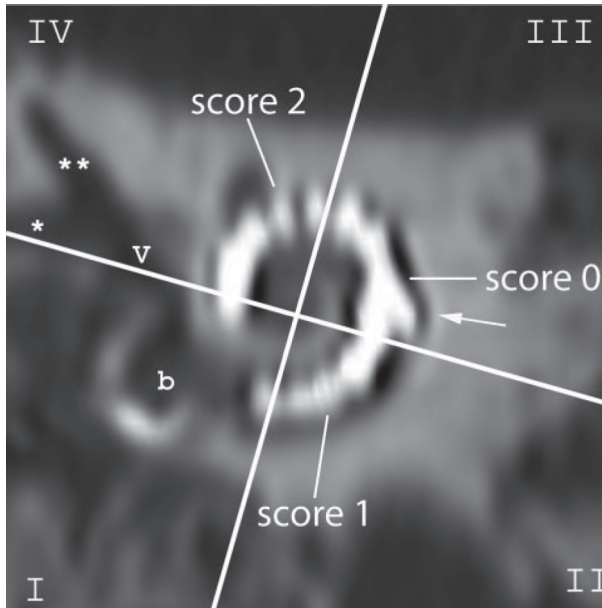


Figure 1. Scoring of the visibility of electrode contacts and anatomical structures: on a MPR perpendicular to the modiolus of a MSCT image of the implanted human cadaver temporal bone, the cochlea is divided in 4 quadrants (crosslines). The quadrants are numbered counterclockwise, and the round window niche is located in the first quadrant (I-IV). A quantitative score from 0 to 2 was given to each electrode contact according to its visibility. Cochlear structures, such as the inner and outer wall, were scored per quadrant. The kinking of the electrode is localized in the third quadrant (arrow). B indicates basal turn of the cochlea at the level of the round window; v, vestibule, * horizontal semicircular canal (SCC); **superior SCC.

PMMA Phantom

To evaluate errors in localization of electrode contacts on CT images, a phantom study was performed. A PMMA phantom, containing a CI, was manufactured (figure 2a). The well-described geometry of the phantom served as a reference for measurements in CT images. It consisted of 2 100- x 100-mm² slabs of 14-mm-thick PMMA. In one of the slabs, a groove was cut by using a 3D milling machine; the second slab served as a cover. The edges of the phantom were rounded to prevent streak artifacts in the reconstructed images. Because the diameter of the electrode carrier reduces from electrode 16 toward the tip, the size of the groove was adjusted along its path to assure a tight fit of the CI.

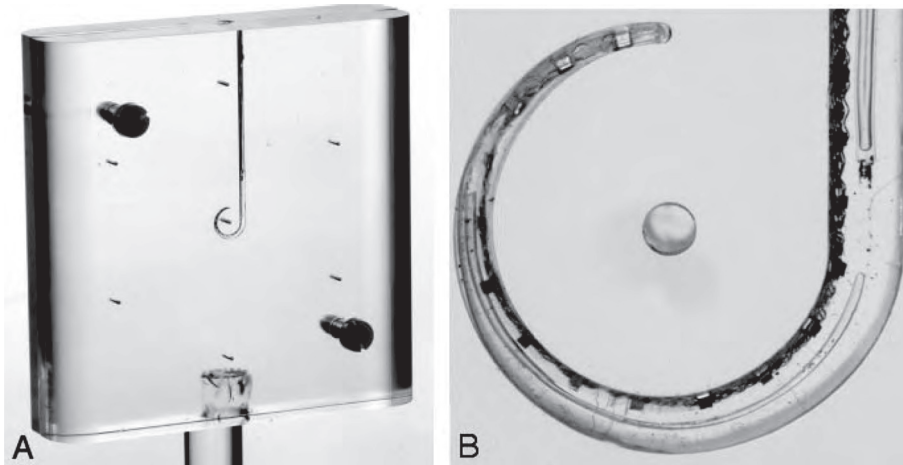


Figure 2. Photograph (A) and 1 high-resolution optical image (B) of the PMMA phantom containing a cochlear implant.

Starting along a straight line, the trajectory was curved from electrode 13 towards the tip such that the CI followed approximately a three-quarter turn. At the center point of this curve and 35 mm from center point, at the corners of a hexagon, holes were drilled as reference markers. To identify the location of the center of the electrode surface within the phantom, a number of high-resolution optical images were acquired until optimal visualization of all of the electrode contacts was achieved (3367 dpi; figure 2b).

On these images, all 16 of the contacts were marked, and their positions were calculated relative to the phantom markers and groove wall. Based on these data, a computer model of the PMMA phantom was created for application in a MatLab based software (MatLab R2006a, MathWorks, Novi, Mich).

This in-house developed software calculated differences between electrode position as indicated by an observer and their known position in the phantom. For these measurements, MPRs were produced with the image plane parallel to the CI on a workstation (Anet64; Toshiba Medical Systems) by 4 observers (figure 3, 1 head and neck radiologist with 6 years of experience and 3 physicists involved in CT). Two datasets were stored: one with a large FOV encompassing the six outer markers and another with a small reconstruction FOV containing the CI only. At first the computer model of the phantom, showing only the position of the seven markers, was fitted to the large FOV MPRs. Subsequently, by using the same center point, fitting parameters were applied to

the small FOV MPR on which 4 observers marked the position of each electrode. The difference between electrode contact position as indicated by the observer and position in the computer model was calculated automatically. From these data, the absolute mean difference per electrode contact was calculated for each scanner.

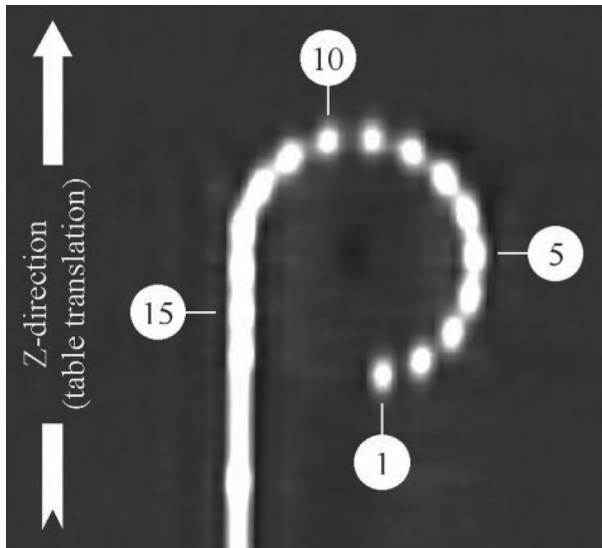


Figure 3. MSCT of the PMMA phantom: 16 electrode contacts are numbered from the tip to the base: electrode numbers 1, 5, 10, and 15 are indicated.

PSF Phantom

For the PSF measurement, a phantom containing an iron bead with a diameter of 0.18 mm was scanned. Spatial resolution was quantified by measuring the full width at half maximum (FWHM) of the PSF curve. FWHM was measured in x- and y-direction (in-plane) and in z-direction (longitudinal).

All of the axial images were analyzed by an in-house developed MatLab-based script. From the axial images, binary images were calculated with a threshold at 1000 Hounsfield Units (HUs). With the binary images, the center of the bead was determined followed by recording of pixel values in three dimensions (x, y, and z) over a distance of 5 mm. To calculate the FWHM in relation to the background, a baseline correction on the resulting curves was performed. The FWHM was calculated for all of the curves. The

mean FWHM for all of the repeated measurements per scanner was calculated in-plane and in the longitudinal direction.

Results

Ex Vivo Study

Assessment results of the human cadaver temporal bone are summarized in Table 2. The average VAS score of the overall impression of the postoperative CT images was lower for Brilliance-64 and LightSpeed-64 relative to Aquilion-64 and Sensation-64 (figure 4). A similar observation was made for the quantitative score of images perpendicular to the modiolar axis. Brilliance-64 and LightSpeed-64 images yielded limited information in the first projection. With the second projection some improvement in detection of individual contacts was obtained (2 points).

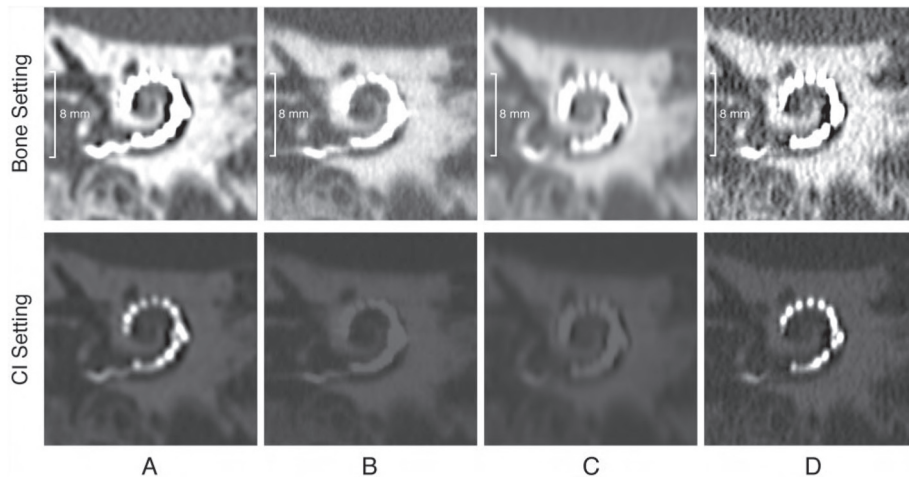


Figure 4. MPR CT images of the human cadaver temporal bone along the plane of the electrode array on Aquilion-64 (A), Brilliance-64 (B), LightSpeed-64 (C) (also seen in figure 1), and Sensation-64 (D). The upper set of images is displayed with W/L 3000/800 and shows cochlear anatomic structures, such as the semicircular canals, well in all of the scanners. The lower set of images shows the chosen manually adjusted window/level setting for visualization of the electrode contacts. This illustrates that a wide range of HUs is essential for visualization of the cochlear implant.

Table 2: Results of the human temporal bone study

scoring parameters	scoring method	Aquilion 64	Brilliance 64	LightSpeed 64	Sensation 64
overall impression	VAS	7.8 (1.0)	3.2 (1.0)	3.0 (1.1)	7.9 (0.7)
axial oblique MPR,	quantitative score	23.2 (2.7)	12.6 (4.4)	8.0 (3.9)	24.2 (4.8)
distinction of electrode contacts					
coronal oblique MPR,	quantitative score	23.7 (3.6)	14.2 (3.7)	10.2 (3.3)	25.6 (3.3)
distinction of electrode contacts					
Kinking	VAS	6.1 (2.1)	1.7 (1.5)	1.3 (1.2)	6.8 (2.0)
inner cochlear wall 4 quadrants	VAS	6.9 (1.3)	4.9 (1.5)	4.1 (2.0)	6.2 (1.1)
		6.6 (1.1)	4.7 (1.3)	4.3 (1.7)	5.7 (1.4)
		6.2 (1.2)	3.9 (1.5)	3.9 (1.1)	5.3 (1.5)
		6.4 (1.4)	3.6 (1.7)	3.9 (1.4)	5.5 (1.9)
outer cochlear walls 4 quadrants	VAS	7.7 (1.1)	6.8 (1.4)	5.5 (1.7)	7.4 (0.9)
		7.6 (1.2)	6.8 (1.1)	5.5 (1.5)	7.4 (1.0)
		7.1 (1.4)	5.2 (1.7)	4.6 (1.6)	6.8 (1.8)
		6.6 (1.9)	4.8 (1.8)	4.1 (1.8)	6.4 (1.9)

Note : VAS indicates visual analogue scale; MPR, multiplanar reconstruction

Kinking of the electrode was recognized in 68 of 72 scans. It was missed on Brilliance-64 images three times and once on a LightSpeed-64 scan by 2 different observers. When recognized, the VAS score of the exact course of the curled segment was highest in Aquilion-64 and Sensation-64 scans.

Assessment of the inner and outer walls of the basal turn of the cochlea showed a higher average VAS score for the outer wall in all of the quadrants and all of the scanners compared with the inner wall. Statistical analysis showed significantly lower VAS ($p < .008$) for Brilliance-64 and LightSpeed-64 compared with Aquilion-64 and Sensation-64.

PMMA Phantom

Differences between the positions of the electrode contacts as indicated by the observers compared with the position according to the computer model of the phantom are listed in Table 3 as mean values of their relative distance, calculated for 4 observers. Displacement of electrode contacts ranged from 0.05 to 0.14 mm (mean, 0.10 mm) on Aquilion-64, 0.07 to 0.16 mm (mean, 0.11 mm) on Brilliance-64, 0.07 to 0.61 mm (mean, 0.18 mm) on LightSpeed-64, and 0.03 to 0.13 mm (mean, 0.09 mm) on Sensation-64.

As graphically shown in figure 5, the resulting differences in relative distance vary along the course of electrode array and differ between the 4 scanners (range, 0.03-0.6 mm). Increase in SD, which is more pronounced at basally located electrode contacts in Brilliance-64 and LightSpeed-64, indicates that observers were less consistent in localization. This is consistent with the fact that they reported to be less confident in these cases. Neglecting the most inaccurate measurements with the highest SD (most basal contacts, 12-16) the displacement of electrode contact position was within the range of 0.03-0.2 mm.

PSF Phantom

PSF measurements on all of the systems reproduced well; the mean difference between repeated measurements was 0.00 ± 0.01 mm. FWHM in the x- and y-directions were closely related for all scans with a mean difference of 0.00 ± 0.01 mm. The in-plane resolution was, therefore, calculated as the mean of x- and y-directions. On all of the scanners in-plane FWHM was better than longitudinal FWHM (Table 4). The in-plane resolution varied from 0.48 to 0.68 mm and the longitudinal resolution from 0.70 to 0.98 mm over the 4 scanners.

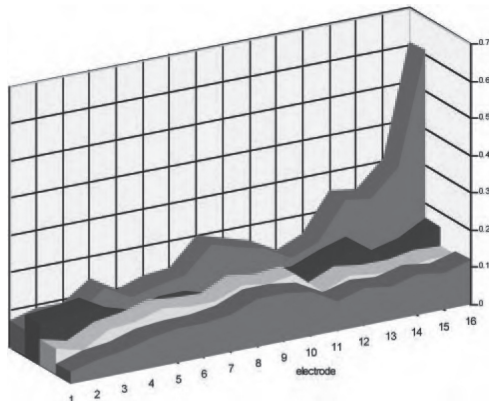


Figure 5. Graphic presentation of the mean differences over 4 observers (y-axis) between electrode position as manually indicated and the position in the computer model (in millimeters). Values are shown per electrode contact (x-axis) for each scanner (Aquilion-64: white, Brilliance-64: dark gray, LightSpeed-64: light gray, Sensation-64: gray). See also Table 3.

Table 3: Results of PMMA phantom measurements

Electrode contact	Aquilion 64	Brilliance 64	LightSpeed 64	Sensation 64
1	0.07 (0.02)	0.11 (0.02)	0.07 (0.02)	0.03 (0.01)
2	0.05 (0.02)	0.12 (0.01)	0.09 (0.03)	0.05 (0.02)
3	0.09 (0.01)	0.13 (0.00)	0.09 (0.03)	0.06 (0.01)
4	0.10 (0.02)	0.09 (0.02)	0.14 (0.02)	0.08 (0.02)
5	0.12 (0.02)	0.07 (0.01)	0.10 (0.04)	0.09 (0.02)
6	0.11 (0.02)	0.09 (0.03)	0.12 (0.01)	0.09 (0.01)
7	0.11 (0.03)	0.09 (0.05)	0.13 (0.02)	0.10 (0.01)
8	0.14 (0.03)	0.07 (0.02)	0.20 (0.04)	0.13 (0.02)
9	0.13 (0.03)	0.08 (0.01)	0.18 (0.03)	0.13 (0.02)
10	0.14 (0.02)	0.10 (0.01)	0.16 (0.03)	0.12 (0.01)
11	0.08 (0.01)	0.10 (0.03)	0.12 (0.02)	0.08 (0.01)
12	0.11 (0.01)	0.13 (0.07)	0.15 (0.02)	0.10 (0.00)
13	0.10 (0.02)	0.15 (0.05)	0.25 (0.10)	0.09 (0.01)
14	0.10 (0.01)	0.10 (0.02)	0.24 (0.11)	0.11 (0.00)
15	0.11 (0.01)	0.12 (0.05)	0.31 (0.15)	0.10 (0.01)
16	0.11 (0.00)	0.16 (0.12)	0.61 (0.35)	0.12 (0.01)

Note: PMMA indicates polymethylmetacrylate

Table 4: Results of PSF measurements

FWHM (in mm)	Aquilion 64	Brilliance 64	LightSpeed 64	Sensation 64
In-plane	0.68	0.52	0.68	0.48
Longitudinal	0.81	0.84	0.98	0.70
Ratio in-plane/longitudinal	0.84	0.62	0.69	0.69

Note: PSF indicates point spread function; FWHM, full width half maximum

Because of a limited available HU range, the maximum HU in the bead was reached on the Brilliance-64, impeding correct measurement of a small part of the top section of the PSF curve. The FWHM values were still calculated as accurately as possible. The maximum amount of improper pixel values was 5; the resulting PSF curve was cut off at the maximum available HU along a distance of 0.4 mm. It was estimated that the HU scale limitation on the Brilliance-64 may have resulted in an overestimation of FWHM values ≤ 0.05 mm.

Discussion

The demands for postoperative imaging in CI surgery became higher over the last years. At first, imaging was used for confirmation of intracochlear position without kinking and integrity of the electrode array. To obtain a better understanding of the postoperative speech perception results and to assess new developments in electrode designs and differences in surgical techniques, a more detailed analysis of the postoperative status was needed. Both the exact position of individual electrode contacts, as well as the morphology of the cochlea, should be visualized. This study was undertaken to evaluate whether it is possible to obtain qualitatively acceptable images of implanted cochleas with 64-section CT scanners of 4 major vendors. Possible limitations are the inherent scanner resolution, image distortion due to metallic artifacts, the scanner-dependent reconstruction algorithm, and the lack of a sufficient wide range of available HUs for displaying structures of high attenuation.

PSF phantom measurements were performed to evaluate whether the inherent resolution of the scanners is high enough to visualize individual electrode contacts. The outcome of the measurements of the in-plane and longitudinal resolution indicates that current CT scanners offer just enough spatial resolution to visualize individual

electrode contacts in the images of the CI evaluated in this study. Because the diameter of the electrode contacts in the investigated CI electrode is somewhat smaller than the measured FWHM of the PSF, we can consider the individual contacts approximately as point sources. In this case, the FWHM indicates the minimum intercontact distance at which the contacts can be distinguished separately in the resulting images. As illustrated in figure 6, an intercontact distance lower than the FWHM results in an intensity distribution that inhibits visualization of individual electrode contacts. Given a longitudinal resolution that ranges from 0.70 to 0.98 mm, it should be possible to visualize the individual electrodes of the HiFocus1J electrode array, which has an electrode spacing of 1.1 mm. However, the CI is curved when following the trajectory of the cochlea, and, as a result, the actual distance between electrodes may become less than the spacing that is measured along the curvature. Separate visualization of electrode contacts may become critical or may even be beyond reach in some scanners, especially closer to the apex, when curvature becomes stronger. For implants with tighter electrode spacing, such as the Contour Advance (Cochlear, Sydney, Australia), with intercontact distance that decreases from base to apex from 0.72 to 0.40 mm, visualization of separate electrodes will present a challenge at the most apical contacts.

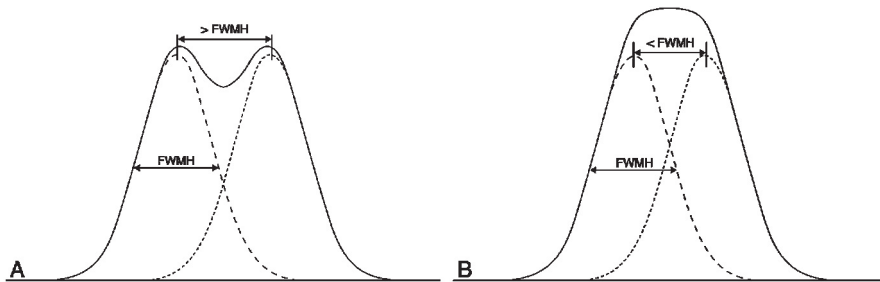


Figure 6. Clinical implications of the PSF: the dotted curves depict the pixel value of a single electrode contact through the center. Summation of these curves renders a curve (black line). When the distance between two electrodes is larger than FWHM, the resulting curve still shows two maximum values, and the electrode contacts can be separated in the image (A). If the distance between two electrode contacts is smaller than FWHM, the resulting curve shows a single peak; the electrode contact can not be visualized separately (B).

Image degradation because of metallic artifacts, measured as displacement of the center of an electrode contact in the PMMA phantom, was dependent on the localization of the contact within the electrode array. The artifacts can be ascribed to scanner resolution and scanner-dependent reconstruction kernel. As shown in the PSF phantom measurements, the z-resolution is somewhat lower than the in-plane resolution. This can contribute to deterioration in separation of individual electrode contacts along the electrode array in the longitudinal direction. In clinical scanning, the precise localization of contacts will differ, depending on the orientation of the CI trajectory relative to the z-direction.

The measurement of the electrode contact position was less consistent and showed higher SD at the most basal contacts [12-16] in Brilliance-64 and LightSpeed-64. This decrease in accuracy is possibly explained by the structural changes of a CI along its length. Whereas in the apex only contacts connected by a fine wire are seen, in the base, several wires, including these connected to apical contacts, are bundled alongside the electrode contacts. The higher amount of metallic material might cause additional distortions. As stated above, this mostly affects the scanners with a lower z-resolution.

It is as yet unclear which maximal error in localization of contacts is clinically acceptable.

Independent of the trajectory of the CI electrode, the visibility of the outer wall of the cochlea was rated better than the visibility of the inner wall or modiolus. This is most probably based on the underlying anatomical substrate. The outer wall is part of the otic capsule, consisting of attenuated bone only. The modiolus or central bony axis of the osseous cochlea contains some neural tissue and shows a distinctly lower attenuation. Therefore, contrast with the perilymph and endolymph in the cochlear lumen will be more distinct for the outer wall than for the inner wall.

Despite the scanty differences in resolution and distortion, the assessment of the human cadaver scans showed a very wide range among the 4 scanners. Both the subjective and quantitative scores showed a clear preference for 2 scanners (Aquilion-64 and Sensation-64). This counts for the overall appreciation of the images, as well as for the visualization of individual electrode contacts and cochlear walls. Other than above mentioned differences in resolution, one of the contributing factors to diversity in image appreciation is the use of different reconstruction kernel types. Various reconstruction kernel types were applied by the manufacturer's specialists, and the following were chosen to be the most appropriate: soft kernel (LightSpeed-64), intermediate kernel

(Aquilion-64 and Brilliance-64), and sharp kernel (Sensation-64). Another limiting factor is the available range of HUs. Because the densities of the evaluated structures differ considerably, a large window width and window level are needed to accurately visualize the electrode contacts (typically 16000/6000). The available range of HUs is -32768 to 32767 for Aquilion-64, -1024 to 2976 for Brilliance-64, -1024 to 3070 for Lightspeed-64, and -10240 to 30710 (extended HU scale) for Sensation-64. Scanners with a restriction in available HU range (Brilliance-64 and LightSpeed-64) received lower scores despite having a FWHM value which is lower than the maximum intercontact distance. Thus, a major cause of the lower appreciation seems to reside in the limited range of available HUs, resulting in an abrupt cutoff of the associated gray values in the images.

The limited HU display capabilities led 4 times to missed kinking. Kinking is a possible complication in implant surgery that influences the stimulation selectivity and can require program changes in the speech processor. Considering the technical abilities of these scanner systems it seems very plausible that an adjustment of the software, that is extension of Hounsfield range, will reduce the described problems in postoperative imaging of CIs.

Of all above mentioned factors related to the performance of the scanners, the wide range of HUs in the images plays the most important role in the overall appreciation of the individual electrode contacts in postoperative imaging of the HiFocus1J electrode array. Thus, the limiting factor is mainly a matter of software improvement and is not related to the fundamental mechanical features of the different scanners.

Conclusion

Imaging protocols for postoperative imaging after cochlear implantation as advised by application specialists or technicians under supervision of the manufacturers of 4 different 64 section CT scanners are presented. Based on the PSF results HiFocus1J electrode contacts can be visualized separately on all of the studied scanners. However, when the curvature of the implant causes narrowing of the intercontact spacing to <1mm, separate visualization of electrode contacts might become critical on LightSpeed-64 (longitudinal resolution for LightSpeed-64, 0.98mm). Assessment of CI visibility, as well as the quantitative assessment of electrode contact positions, varies between

scanners. It seems plausible that software adjustments allowing for a wider range of HUs will be needed in 2 scanners to improve image quality for a possible higher diagnostic value.

Acknowledgements

We thank Frans Prins of the department of Pathology for preparing the human cadaver temporal bone, as well as F.A.W. Peek (department of Otolaryngology) and L.J.M. Kroft, A. Spilt, R. van de Boom, and C.S.P. van Rijswijk (department of Radiology) for evaluating the imaging material. We also thank all of the manufacturers for their cooperation and especially the radiology department of the Erasmus Medical Center, Medical Center Haaglanden, and Utrecht Medical Center for their contributions in obtaining the image material.

References

1. Verbist BM, Frijns JHM, Geleijns J, van Buchem MA. Multisection CT as a valuable tool in the postoperative assessment of cochlear implant patients. *AJNR Am J Neuroradiol* 2005;26:424-429
2. Aschendorff A, Kubalek R, Hochmuth A, et al. Imaging procedures in cochlear implant patients-evaluation of different radiological techniques. *Acta Otolaryngol Suppl* 2004;46-49
3. Tange RA, Grolman W, Maat A. Intracochlear misdirected implantation of a cochlear implant. *Acta Otolaryngol* 2006;126:650-652
4. Jain R, Mukherji SK. Cochlear implant failure: Imaging evaluation of the electrode course. *Clin Radiol* 2003;58:288-293
5. Mecca MA, Wagle W, Lupinetti A, Parnes S. Complication of cochlear implantation surgery. *AJNR Am J Neuroradiol* 2003;24:2089-2091
6. Skinner MW, Ketten DR, Holden LK, et al. CT-derived estimation of cochlear morphology and electrode array position in relation to word recognition in nucleus-22 recipients. *Jaro* 2002;3:332-350
7. van der Beek FB, Boermans PP, Verbist BM, Briaire JJ, Frijns JH. Clinical evaluation of the Clarion CII HiFocus I with and without positioner. *Ear Hear* 2005;26:577-592
8. Cesarini F, Gallizioli M, Solero P, Rolando M, Cassinis MC, Gandini G. Double array cochlear implant: CT findings. *Radiol Med (Torino)* 2002;103:115-118
9. Xu J, Xu SA, Cohen LT, Clark GM. Cochlear view: Postoperative radiography for cochlear implantation. *Am J Otol* 2000;21:49-56
10. Whiting BR, Bae KT, Skinner MW. Cochlear implants: Three-dimensional localization by means of coregistration of CT and conventional radiographs. *Radiology* 2001;221:543-549
11. Chen JM, Farb R, Hanusaik L, Shipp D, Nedzelski JM. Depth and quality of electrode insertion - A radiologic and pitch scaling assessment of two cochlear implant systems. *Am J Otol* 1999;20:192-197
12. Husstedt HW, Aschendorff A, Richter B, Laszig R, Schumacher M. Nondestructive three-dimensional analysis of electrode to modiolus proximity. *Otol Neurotol* 2002;23:49-52

4

Clinical Evaluation of the Clarion CII HiFocus 1 with and without Positioner

FB van der Beek, PPBM Boermans, BM Verbist, JJ Briaire, JHM Frijns

Ear & Hearing 2005; 26: 577-592

Abstract

Objective: To study the clinical outcomes concerning speech perception of the Clarion CII Hifocus 1 with and without a positioner and link those outcomes with the functional implications of peri-modiolar electrode designs, focussing on intrascalar position, insertion depth, stimulation levels and intracochlear conductivity pathways.

Design: The speech perception scores of 25 consecutive patients with the Clarion CII HiFocus 1 implanted with a positioner and 20 patients without a positioner were prospectively determined. Improved multislice CT-imaging was used to study the position of the individual electrode contacts relative to the modiulus and their insertion depth. Furthermore, stimulation thresholds, maximum comfort levels and dynamic ranges were obtained. Finally, these data were associated with intracochlear conductivity paths as calculated from the potential distribution acquired with electrical field imaging.

Results: Implantation with a Clarion Hifocus 1 with positioner showed significantly higher speech perception levels at 3, 6 months and 1 year ($p < 0.05$) after implantation. Basally, the positioner brought the electrode contacts significantly closer to the modiulus, whereas apically no difference in distance toward the modiulus was present. Moreover, the patients with the electrode array in a peri-modiolar position showed deeper insertions. The T-levels and dynamic range were not significantly different between the positioner and nonpositioner patients. Furthermore, the intracochlear conductivity paths showed no significant differences. However, a basal current drain is present for the shallowly inserted nonpositioner patients.

Conclusion: A basally perimodiolar electrode design benefits speech perception. The combination of decreased distance to the modiulus, improved insertion depth and insulating properties of the electrode array have functional implications for the clinical outcomes of the peri-modiolar electrode design. Further research is needed to elucidate their individual contributions to those outcomes.

Introduction

Speech perception is increasing rapidly in recent years for patients with cochlear implants (Ramsden, 2004). This is due to ongoing improvements in both cochlear implant electrode array design and new speech processing strategies. Some of these recent modifications are peri-modiolar electrode designs that theoretically reduce current consumption, increase dynamic range, and give a higher selectivity of stimulation by placing the electrode contacts in closer proximity to the excitable neural elements. Initially, the beneficial influences of a medial position in the scala tympani were suggested by animal experiments (Shepherd, Hatsushika, & Clark, 1993) and by detailed computational models (Frijns, de Snoo, & Schoonhoven, 1995; Frijns, de Snoo, & ten Kate, 1996). A comparison of the Clarion HiFocus 1 electrode in lateral and modiolar hugging position was made in a computational model of the electrical stimulated cochlea (Frijns, Briaire, & Grote, 2001). The findings of this comparison were that at a peri-modiolar position spatial selectivity and dynamic range were favorably influenced at the basal turn, whereas at more apical sites a position near the outer wall was desirable to avoid the possibility of so-called cross-turn stimulation, which we believe produces additional low-pitched percepts that are caused by excitation of nerve fibres originating from the cochlear turn above the location of the stimulating electrode contact.

After different peri-modiolar designs were introduced, temporal bone studies proved the peri-modiolar position of these electrodes (Tykocinski et al., 2000; Fayad, Luxford, & Linthicum, 2000; Richter et al., 2002; Roland, Fishman, Alexiades, & Cohen, 2000; Tykocinski et al., 2000). A clear difference between the Clarion HiFocus 1 design with the partially space-filling Electrode Positioning System (EPS) and the Nucleus Contour was the fact that the HiFocus obtained the peri-modiolar position mainly at the basal turn, whereas the stylet removal positioned the Contour electrode at the apical side toward the modiolar (Balkany, Eshraghi, & Yang, 2002). The effects of the latter electrode design have also been studied with cochlear view radiographs, and a more peri-modiolar position at the apical side was shown (Cohen, Richardson, Saunders, & Cowan, 2003; Cohen, Saunders, & Clark, 2001; Saunders et al., 2002).

The predicted reduction in the electrical current required to activate the auditory system with peri-modiolar electrodes was shown in animals and patients using electrical auditory brain response (EABR) measurements. Thresholds decreased and amplitudes of the wave V increased after bringing electrodes in a peri-modiolar position (Firszt,

Wackym, Gaggl, Burg, & Reeder, 2003; Pasanisi, Vincenti, Bacciu, Guida, & Bacciu, 2002). This effect was more robust basally with the Clarion HiFocus, whereas the Nucleus Contour showed lower thresholds at the apex (Wackym et al., 2004). Moreover, decreases of stapedius reflexes and electrical compound action potentials (eCAP) thresholds were found for the HiFocus using the EPS, being more pronounced basally (Eisen & Franck, 2004; Mens, Boyle, & Mulder, 2003). Furthermore, some studies showed that the Nucleus Contour had lower perception thresholds and lower maximum comfort levels compared with the Nucleus banded electrode, which takes a lateral position within the scala tympany (Parkinson et al., 2002; Saunders et al., 2002). Due to reduced thresholds and maximum comfort levels with the Contour electrode, the dynamic range did not show improvements (Saunders et al., 2002). Additionally, in pediatric recipients a predecessor of the Clarion HiFocus 1 showed lower perception thresholds and maximum comfort levels when implanted with a positioner (Young & Grohne, 2001). In contrast with previous reports, another study did not show significant differences in T-levels between patients with the Nucleus Contour and the Straight-array (Hughes, 2003).

Better frequency selectivity is, in addition to lowered threshold stimulation levels, thought to be associated with improved speech perception. Different methods have been used to obtain estimates of the spatial selectivity, as the longitudinal spread of excitation along the tonotopic cochlea is of utmost importance for the spectral percepts of the patients. Psychophysical studies indicated that patients are able to exploit the tonotopic organization of the cochlea and a correlation was found between electrode discrimination and speech perception (Busby, Tong, & Clark, 1993). However, psychophysical measures of spatial selectivity failed to correlate with the distance of the electrode array to the modiolus (Cohen et al., 2001). Different approaches are needed to measure spatial selectivity without the drawbacks of subjective tests. An important role in measuring spatial selectivity may arise for the telemetry systems of the contemporary cochlear implants (neural response imaging/telemetry, NRI/NRT, of Clarion and Nucleus cochlear implants respectively). These systems can measure both the intracochlear potential during current injection as well as the small biological potentials generated by the auditory nerve. Although spatial selectivity measurements using eCAP are still under development, recent data point out that a closer proximity of the electrode contacts to the modiolus is associated with a narrower excitation pattern (Cohen et al., 2003; Hughes, 2003). Recently, an impedance model has been developed, which can be used to study

the spatial distribution of the injected current (Vanpoucke, Zarowski, Casselman, Frijns, & Peeters, 2004). This impedance model is based on objective measurements obtained with Electrical Field Imaging (EFI) of the Clarion cochlear implant.

Initial clinical evaluations of the Clarion HiFocus 1 (Frijns, Briaire, de Laat, & Grote, 2002) and Nucleus Contour (Tykocinski et al., 2001) showed excellent speech understanding. After implantation with the Nucleus Contour a large variation in the degree of coiling across subjects could be observed. This variation in coiling is presumably surgeon and patient dependent and showed no significant effect on thresholds or speech perception (Marrinan et al., 2004). A recent study showed that the peri-modiolar designed Nucleus Contour electrode contributed to improved speech understanding compared to its straight predecessor (Bacciu et al., 2005).

In 2002 the manufacturer of the Clarion HiFocus with a separate positioner system (Advanced Bionics Corp., Sylmar, CA) withdrew its system from the market. The decision to withdraw the positioner was made after the FDA reported meningitis cases associated with cochlear implantation (<http://www.fda.gov/cdrh/safety/cochlear.html>). More research to reveal the causes of the meningitis of cochlear implant patients followed and recommendations concerning the prophylaxis and treatment were published (Cohen, Roland, Jr., & Marrinan, 2004; Lefrancois & Moran, 2003; Nadol, Jr. & Eddington, 2004; Reefhuis et al., 2003). Afterward, the array was inserted without positioner, as a one-component electrode, after a hypothesis was postulated suggesting that space between the positioner and the electrode could act as a possible pathway for bacteria to enter the cochlea. Although histologic evidence did not support this pathway as part of the pathogenesis of meningitis, a precise explanation for the increased incidence of meningitis is still lacking. The withdrawal of the positioner from the market provided the clinical opportunity to study the influence of the positioner on speech perception. After the withdrawal the implantation procedure in our clinic continued in the same manner, with the exception that the implantation was performed without insertion of a positioner. The electrode array implanted was the same for all patients and furthermore they encountered the same patient selection, implanting surgeon, fitting procedures and rehabilitation.

The positioner group (P-group) was implanted between July 2000 and July 2002. The 25 patients of this group were described earlier (Reference Note). The nonpositioner group (NP-group) was implanted between July 2002 and March 2003. This NP-group consisted of 20 patients. For both groups now, at least 1 yr of follow-up of speech

perception scores is available. In this study differences in speech perception found between the group with the peri-modiolar electrode implanted as designed and the latter group are presented. Additionally, speech perception scores and the radial distances to the modiolus and the insertion depths, determined with MSCT (multi slice computer tomography) for each electrode contact, will be correlated with perception thresholds and dynamic range. Finally, to obtain more insight into the effects of the positioner on intracochlear current pathways, electrical field imaging and modelling measurements (Vanpoucke et al., 2004) are discussed.

Material & Methods

All 45 patients in this study have been implanted in the Leiden University Medical Centre with a Clarion CII HiFocus 1 cochlear implant. After having implanted the first 25 patients with a partially inserted positioner (P-group), the implantation of the next 20 patients was performed in our centre in the same manner only without insertion of this positioner (NP-group). In the group with the positioner (P-group) this positioner was placed between the electrode array and the outer wall. The positioner was designed to have a slightly shallower insertion than the HiFocus electrode array. Furthermore, it was partially inserted with the insertion tool, resulting in a protrusion of the positioner from the cochleostomy of approximately 5 mm. All patients had a full insertion of the electrode array, except for one P-patient, deafened by meningitis. During implantation in this patient a resistance was encountered and the four most basal contacts were not positioned inside the cochlea. The NP-group was limited to 20 patients because, after this group, the patients in our clinic were implanted with the new HiRes90K implant with HiFocus 1J electrode.

After the operation of the ninth patient without a positioner, a trend of stagnation of growth in speech perception was detected through analysis of the initial results of the first six hooked-up NP-patients, with a maximum follow-up of only 2 mos. Additionally, the most basal electrode contacts in those six patients showed higher T-levels than the other contacts. Two factors were considered to be possible causes of these changes: decreased modiolar approximation and shallower insertion. Only the latter could be controlled in absence of the positioner, and it was decided to aim for a deeper insertion in the patients implanted afterward. The jog of the electrode was now placed inside the

cochleostomy instead of just in front of it. No extra resistance was felt during insertion of the electrode array. The results of the NP-group will be presented separately for the group of the first 9 patients, having a shallow insertion (NPshallow, NPs-group) and the second group of 11, intended to have a deeper insertion (NPdeep, NPd-group).

All patients included in this study were postlingually deafened. More demographics of the patient groups are given in Table 1, causative factors in Table 2. The data show, besides significant differences in age, a good similarity in between groups with respect to duration of deafness and preoperative scores. Median preoperative phoneme scores, determined with headphones using standard speech audiometry at the ipsilateral ear, were 0% for all groups. In general the worse hearing ear was chosen for surgery, except for two cases in which unilateral vestibular function and unilateral cochlear patency urged implantation of the better ear.

Speech Material

Speech discrimination scores were assessed during normal clinical follow-up at predetermined intervals, starting one wk after initial fitting. The standard Dutch speech test of the Dutch Society of Audiology, consisting of phonetically balanced monosyllabic (CVC) word lists, was used (Bosman & Smoorenburg, 1995). Although this test is typically scored with phonemes in the Netherlands and Flanders, the data are also shown as word scores, which is a more common reporting method in Anglo-Saxon countries. For tests in noise the standard speech-shaped noise from the same CD was used. To improve test accuracy, 4 lists (44 words) were administered for each quiet and noise condition. All testing was done in a soundproof room, using a calibrated loudspeaker in frontal position at 1-meter distance. Subjects were tested in quiet at speech levels of 65 and 75 dB SPL. When the average phoneme score in quiet was higher than 50%, subjects were also tested in noise at a speech level of 65 dB. Speech scores in noise were assessed at maximally 4 signal to noise ratios (SNR), starting with a SNR of +10 dB and continuing at +5, 0 and -5 dB SNR until the phoneme score was lower than half the score in quiet. However, some patients had to stop before this criterion was reached because they could not tolerate the higher noise levels. For further analysis, the speech recognition threshold (SRT) and phoneme recognition threshold (PRT) were calculated from the acquired data (Hochberg, Boothroyd, Weiss, & Hellman, 1992). The SRT is the SNR at which the patient scored 50% of the phonemes correct. The PRT was defined as the SNR at which the phoneme score was half the individual patients' score in quiet.

Table 1. Patient demographics

N	P-group		NP-group	
	All 25	All 20	NPs (n9)	NPd (n11)
Age at implantation (yr)	44.9 (13.4;14.0-67.0)	59.9 (10.8;40.0-76.0)**	60.1 (7.6;50.0-71.0)**	59.6 (13.3;40.0-76.0)**
Duration of deafness (yr)	18.5 (15.0;0.2-43.0)	16.8 (14.5;0.3-46.0)	16.7 (16.5;0.3-46.0)	18.8 (14.4;2.0-46.0)
Preoperative phoneme scores (%)				
Ipsilateral	6.3 (9.8;0.0-33.0)	7.2 (11.0;0.0-42.0)	2.0 (6.0;0.0-18.0)	11.5 (12.5;0.0-42.0)
Contralateral	4.0 (9.8;0.0-45.0)	2.3 (5.9;0.0-24.0)	0.3 (1.0;0.0-3.0)	3.8 (7.7;0.0-24.0)
Preoperative tone audiogram (%)				
Ipsilateral	111.6 (12.4;85.0-130.0)	117.7 (12.0;83.3-130.0)	119.6 (14.5;83.3-130.0)	104.2 (14.6;85.0-130.0)
Contralateral	116.1 (7.8;103.3-130.0)	109.6 (15.4;85.0-130.0)	116.1 (14.5;90.0-130.0)	116.1 (10.0;101.7-130.0)

Data are averages with standard deviations of the population and minimal and maximal values between brackets. Significant differences, marked (**p0.01), are between the P-group and the marked NP-group.

Table 2. Causes of deafness in the various patient groups

	P-group	NP-group	NPs-group	NPd-group
Hereditary	10	10	4	6
Trauma	1	1	1	0
Antibiotics	1	0	0	0
M. Meniere	1	1	1	0
Meningitis	3	1	0	1
Otosclerosis	0	1	1	0
Unknown				
Progressive	7	5	1	4
Sudden deafness	2	1	1	0
Total	25	20	9	11

Radial Distances and Insertion Depths

With a dedicated MSCT data acquisition protocol, developed at the department of neuroradiology of the Leiden University Medical Center, imaging of the implanted electrode array was obtained (Verbist, Frijns, Geleijns, & van Buchem, 2005). In contrast to previous CT-imaging of implanted electrode arrays, all individual electrode contacts were discernible and their relation to fine anatomic cochlear structures was visible. Initially, the improved MSCT-technique was not available, and postoperative scans of only 15 of the 25 P-patients have been acquired. MSCT-scans of all 20 NP-patients were available for analysis.

Figure 1A shows an electrode array inserted with positioner. Between the basal lateral wall of the cochlea and the electrode, a hypodense area is visible. This corresponds with the location where the positioner is situated. As the positioner takes the space at the outer wall, the electrode is displaced toward the modiolus. Because the positioner is only partially inserted, it does not force the electrode into a peri-modiolar position at the apical end of the cochlea. Moreover, the material properties will tend to straighten the electrode. The radius of the cochlea is smaller than the radius of the electrode array in its natural position and without force toward the modiolus at this apical part of the cochlea the electrode will follow the outer curve. The MSCT-scan shows that more apically the electrode is indeed located close to the lateral wall and that a hypodense space exists between the electrode and the modiolus. Figure 1A only shows the position of the electrode in the basal turn, whereas the apical tip of the electrode is not visible and was projected on another slice.

The electrode inserted without positioner (figure 1B, NPs-patient) tends to be positioned laterally throughout its entire length, leaving more space between the electrode contacts and the modiolus compared with the P-patients. The path following the outer turn is longer than the path the electrode follows with the positioner inserted. This causes a less deep insertion of the electrode when no positioner is inserted. Figure 1(C and D) shows three-dimensional reconstructions of typical implants of the P-group and the NPs-group, respectively. The latter shows a less deep insertion compared with the P-group. After hand-marking the centres of the electrode contacts as well as the modiolar contour the radial distance of each electrode to the modiolus was automatically determined. Interconnecting lines were automatically drawn between successive electrode contacts. The angles between these lines and a reference line along the basal part of the cochlea were calculated. The position of the electrode contact was expressed

as the cumulative angle between those lines. The coordinate system, based on Chen et al. (1999), is illustrated in Figure 1E.

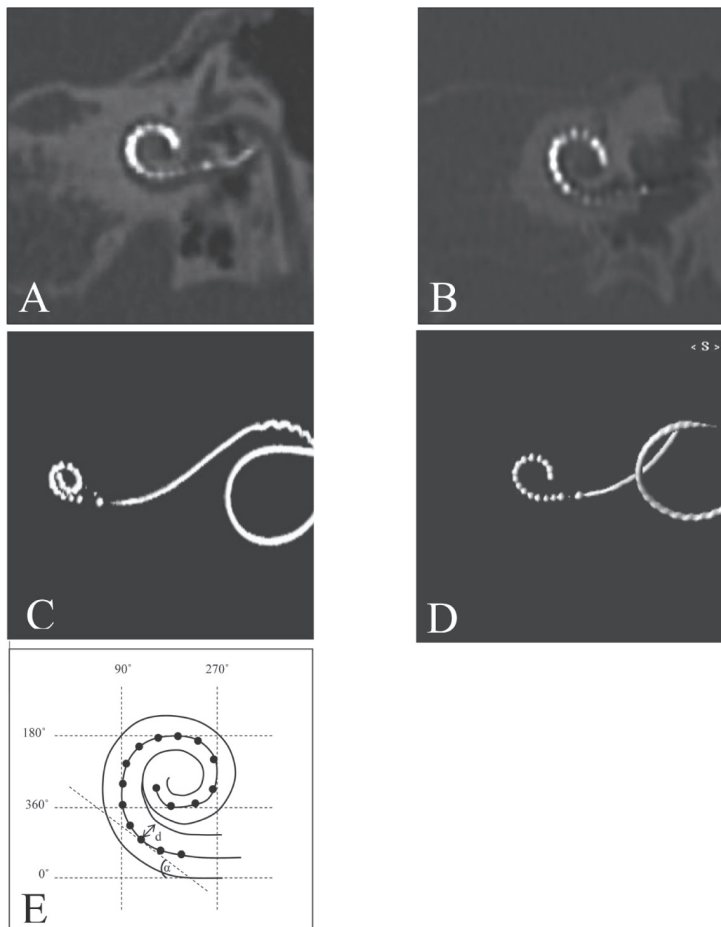


Figure 1. Typical oblique multi-planar reconstructions of MSCT scans of implanted cochleas with (A) and without (B) the use of a positioner show, respectively, a medial and a lateral position of the basal electrode array. Three-dimensional-reconstructions (C&D), using the MSCT scans, show insertion depths of the apical tips (not seen on A) of the same electrode arrays displayed in A and B. The diagram (E) shows the coordinate system used to determine the insertion angle. The angle illustrates the insertion angle of an electrode contact expressed in degrees, and d shows the radial distance from this contact to the modiolus.

T-levels, M-levels & Dynamic Range

All patients in this study used a CIS-strategy. Except for five patients in the P-group, who were hooked-up with a HiRes strategy, the first 3 mos the SCLIN emulation mode with 8 active contacts and 833 pps/contact (75 μ sec/phase) was used. At 6 mos 26 patients of the 45 patients used a HiRes strategy programmed with the BEPS software package, whereas 37 patients were using the HiRes strategy at 1 yr of follow-up (1400 pps/contact, 21 μ sec/phase, ranging from 8 to maximally 16 active contacts). In the Discussion section, we argue that HiRes experience is probably not a contributing factor to any differences in speech perception scores between the P and NP groups. For all electrode contacts the thresholds (T-levels) and the most comfortable loudness levels (M-levels) were determined during fitting following the Leiden fitting strategy (Frijns et al., 2002; Reference Note). The T-levels were obtained in burst mode with an up-down-up method and an up sloping M-level profile was used. The M-levels of the basal electrode contacts were increased with the intention to improve consonant understanding, especially in background noise. Further adjustments were done with running speech. If patients experienced a dominant low-pitched sound, the apical M-levels were reduced.

Both the T- and M-levels included in this study were obtained after approximately 3 mos of implant use in SCLIN emulation mode. T- and M-levels acquired from the five P-patients who always used HiRes were not comparable to those of the SCLIN-patients, as the result of different stimulation rate and pulse duration. Therefore, levels of all the NP-patients but only of 20 of the P-patients are analyzed in this study. The dynamic range was defined as the M-level minus the T-level.

Electrode Impedances and Conductivity Paths

Immediately before hook-up, the standard clinical method for recording impedances using the telemetry facility was used. The impedance of every electrode contact was measured to get some information about the tissue and fluid surrounding the electrode. To obtain a clearer picture of the current pathways in the cochlea, electrical field imaging modeling (EFIM) measurements were performed (Vanpoucke et al., 2004). With these measurements, each electrode contact is consecutively stimulated in monopolar mode and the induced intracochlear potential is captured at all electrode contacts (figure 2A). From the intracochlear impedance map, a leaky resistive transmission line model is derived by using multi-dimensional optimization algorithms. The electrical tissue model is a ladder network with 15 sections (figure 2B). Each section consists of a longitudinal

and a transversal resistor and corresponds physically to the cochlear segment between consecutive contacts. The longitudinal resistors represent the current flow along the scala tympani and the transversal resistors model the current straying out of the cochlea. The model is terminated by a basal resistor. This basal resistor models the current drain from the basal end of the cochlea to the reference electrode located at the implant case. From the model, a tissue impedance can be derived at the stimulation contact, resembling the tissue input impedance seen at a particular stimulation contact. EFIM-measurements were performed in 20 of the P-patients and 16 of the NP-patients after 1 yr of cochlear implant use. In 11 of the 20 P-patients both a CT scan and EFIM measurements were performed. Of the NP-patients, EFIM-measurements obtained after 1 or 2 mos were also available.

Results

Speech Perception in Quiet

The bars in figure 3 show the average scores for the monosyllabic CVC-word tests in quiet for both the P- and the NP-group. The data are displayed as phoneme scores (figure 3A), which is standard for this monosyllabic word test, and are also displayed as word scores (figure 3B) for a better international comparison. One year of follow-up was complete for both the P- and the NP-group. During the follow-up period, both groups show an increase in performance on the speech tests, which is the most rapid in the first weeks after initial fitting. However, after 1 mo, the performance of the NP-group tends to lag behind the P-group, and at 3 mos and 6 mos, the differences in speech perception scores reach significant levels ($p < 0.05$). Also at 1 yr of follow-up, the NP-patients score significantly lower than the P-patients (73% versus 83%, $p < 0.05$). Further analysis of the speech reception scores of the NPs- and the NPd-group only revealed limited differences between both groups (figure 3C). Although initially the speech perception scores tend to increase more rapidly after implantation for the NPs-patients the differences did not reach significant levels at 1 yr ($p > 0.1$).

Demographic factors showed little differences between the P- and NP-groups, except for the age. As shown in Table 1, the average age of the P-group and the NP-group differed by 15 ys. However, in neither group is the age of the patient at implantation correlated significantly with speech perception. This is illustrated in figure 4A, where

speech perception scores at 1 yr were plotted against age of the P- and NP-group and no significant correlations were found ($R^2 < 0.001$, $p > 0.9$ and $R^2 = 0.002$, $p > 0.9$). Both the P-group and the NP-group contain patients with a wide range of duration of deafness, ranging from a couple of months up to more than 40 yrs (Table 1). Interestingly, in both groups, no significant correlation exists between speech perception and the duration of deafness before implantation as shown in Figure 4B ($R^2 = 0.10$, $p > 0.1$ and $R^2 = 0.007$, $p > 0.7$).

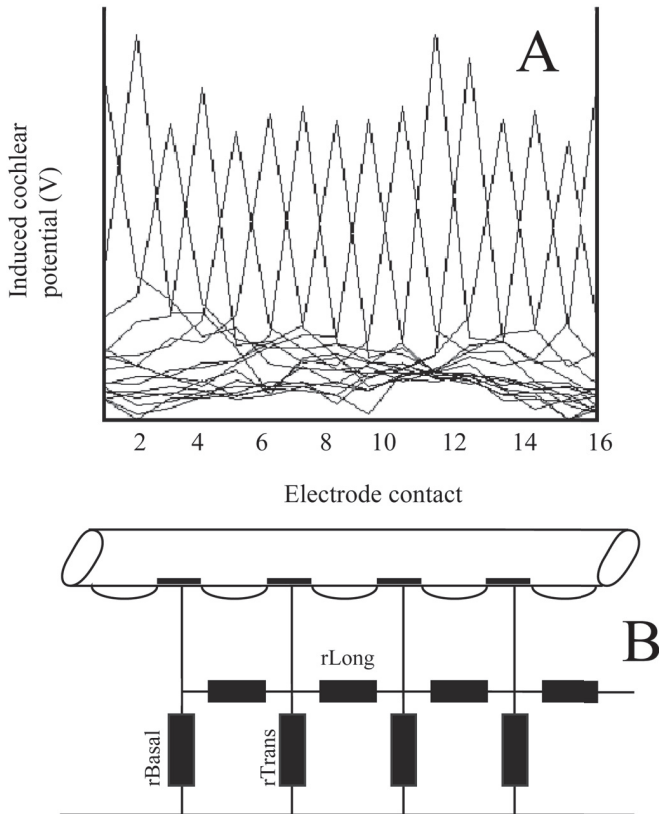


Figure 2. With potentials, captured with electrical field imaging (EFI) (A), resistors are modeled, which reflect the local electrical conductivity of the cochlear tissues. The model consists of 15 longitudinal and 15 transversal resistors, representing the resistance between adjacent electrodes. A basal resistor, representing the resistance between the basal electrode in the cochlea and the reference electrode on the implant casing, terminates the model (B).

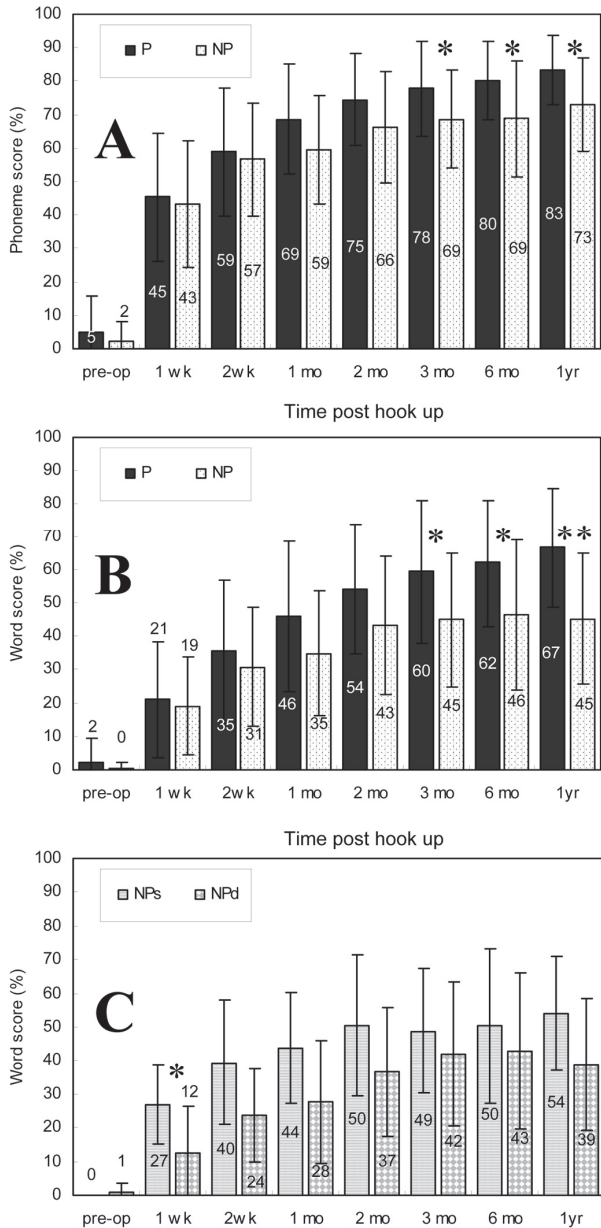


Figure 3. Speech perception on monosyllabic (CVC) words in quiet of the positioner-group (P) and the non positioner-group (NP) plotted as phoneme scores (A) and as word scores (B) as a function of time after hook-up. Word scores of the NP-group are shown for the NPs-group and the NPd-group separately in C. Significant differences between speech perception scores of both groups are marked (* $p < 0.05$; ** $p < 0.01$). The number of patients in the subgroups is shown in Table 3.

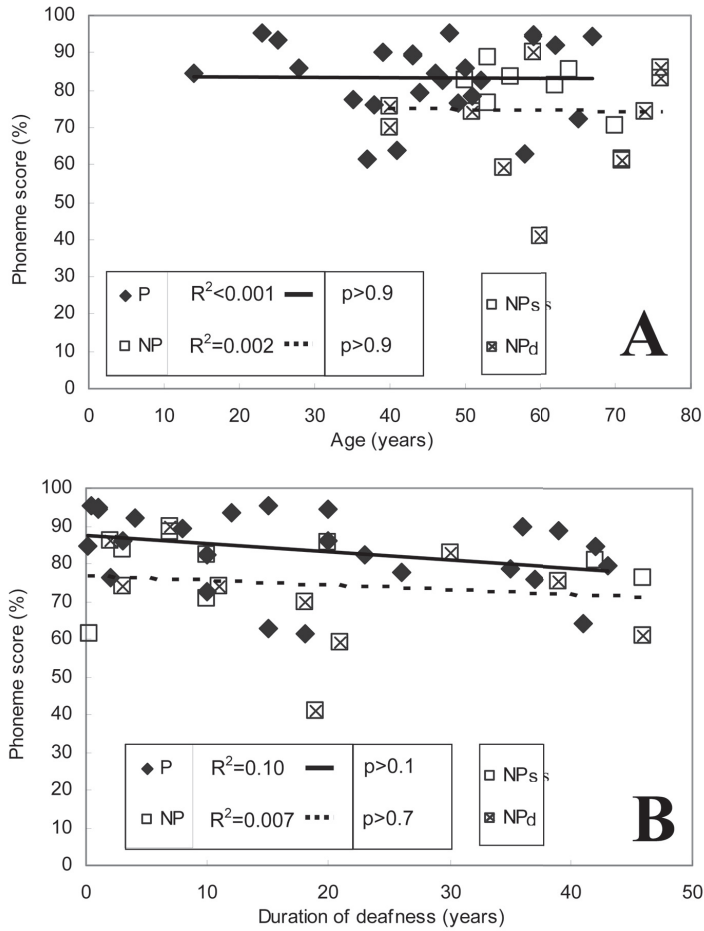


Figure 4. **A**, Phoneme scores on monosyllabic (CVC) words in quiet after 1 yr of follow-up of the positioner-group (P) and the non positioner-group (NP) plotted against the age at implantation. The lack of correlation is shown by trendlines, R^2 and p values. **B**, Phoneme scores after 1 yr of follow-up of the positioner-group (P) and the non positioner group (NP) plotted against the duration of deafness. The lack of correlation is shown by trendlines, R^2 and p values. The number of patient sin the subgroups is shown in Table 3.

Table 3. Number of subjects represented in each part of Figures 3, 4, 5, 6, and 7

Figure 3, A and B		Preop	1wk	2wk	1mo	2mo	3mo	6mo	1yr		
P:	n=	25	25	25	25	25	25	25	25		
P:	n=	20	20	20	20	19	19	19	19		
NPs:	n=	9	9	9	9	9	8	9	8		
NPd:	n=	11	11	11	11	10	11	10	11		
Figure 3C		Preop	1wk	2wk	1mo	2mo	3mo	6mo	1yr		
NPs:	n=	9	9	9	9	9	8	9	8		
NPd:	n=	11	11	11	11	10	11	10	11		
Figure 4, A and B		P:	n=	25							
NP:	n=	19									
NPs:	n=	8									
NPD:	n=	11									
Figure 5A		P:	n=	15							
NP:	n=	20									
NPs:	n=	9									
NPd:	n=	11									
Figure 5 B		0-60	60-120	120-180	180-240	240-300	300-360	360-420	420-480	480-540	540-600
P:	n=	15	15	14	14	14	14	12	8	6	1
NP:	n=	13	19	20	20	20	17	10	8	4	1
NPs:	n=	9	9	9	9	9	6	2	1	0	0
NPd:	n=	4	10	11	11	11	11	8	7	4	1

Figure 5 C													
P:	n=	15											
NP:	n=	19											
NPs:	n=	8											
NPd:	n=	11											
Figure 6, A and C													
P:	n=	12											
NP:	n=	20											
NPs:	n=	9											
NP	d:n=	11											
Figure 6, B and D		0-60	60-120	120-180	180-240	240-300	300-360	360-420	420-480	480-540	540-600		
P:	n=	12	11	11	11	11	11	6	4	5	0		
NP:	n=	13	19	20	20	20	16	6	8	3	2		
NPs:	n=	9	9	9	9	9	5	1	1	0	0		
NPd:	n=	4	10	11	11	11	11	5	7	3	2		
Figure 7, A, B, and D		0-60	60-120	120-180	180-240	240-300	300-360	360-420	420-480	480-540	540-600		
P:	n=	11	11	10	10	9	10	9	6	4	0		
NP:	n=	11	15	16	16	16	13	7	6	4	2		
NPs:	n=	8	8	8	8	8	5	1	1	0	0		
NPd:	n=	3	7	8	8	8	8	6	5	4	2		
Figure 7C													
P:	n=	20											
NP:	n=	16											
NPs:	n=	8											
NPd:	n=	8											

Speech Perception in Noise

Speech scores in noise obtained 1 yr after initial fitting were analyzed. Data were available for all P-patients and 17 NP-patients. Three patients of the NP-group (2 NPs, 1 NPd) did not participate in the speech in noise tests because their phoneme scores in quiet were lower than 50%. First, the phoneme scores measured at +10, +5, 0 and -5 dB SNR were compared between the two groups. The average scores at +10 and +5 dB SNR of the NP-patients were consistently lower than the average scores of the P-group ($p < 0.05$). However, for the 0 dB and -5 dB SNR conditions there were no significant differences between the average group scores. The lack of significance could be due to the fact that a substantial number of poorer performing patients was not tested at 0 and -5 dB SNR because the stop criterion for this test was already met at +5 dB SNR. In addition, for each of the 25 P-patients and the 17 NP-patients the SRT and the PRT (phoneme recognition threshold) were derived to characterize the ability to discriminate speech in noise. The average PRT as well as the average SRT for the P-group (-0.9 dB SNR and +1.2 dB SNR, respectively) were both significantly lower ($p < 0.05$) than the scores for the NP-group (+1.2 dB SNR and +4.9 dB SNR, respectively). Neither the average speech in noise scores nor the PRT and SRT values showed a significant difference between the NPs-group and the NPd-group.

Distance to Modiolus and Insertion Depth

As described in the Materials and Method section, the measurements determined the radial distance from the center of each electrode contact as seen on the MSCT to the modiulus. To obtain the actual distance of the electrode surface to the modiulus the distance from the center to the surface (approximately 0.25 mm) should be subtracted from the measured distance. Moreover, a silicone bleb, located between the contacts at the medial side of the array accounts for approximately 0.15 mm of the measured distance, as the electrode cannot come closer to the modiulus due to mechanical constraints. Furthermore, preliminary results from phantom studies performed in our clinic showed additionally an average error in distance from the modiulus of approximately 0.1 mm. These extra distances are plotted in figure 5 (A and B) as a horizontal dotted line at 0.5 mm from the modiulus. As shown earlier, the positioner is intended to push the basal electrode contacts toward the modiulus (figure 1). This effect was confirmed by the analysis of the MSCT scans, which showed that the basal electrode contacts of the P-group are located closer to the modiulus than those of the NP-group (figure 5A). This

difference is more prominent basally than apically, and the most basal electrode contacts as well contacts 10 and 8 in the middle region show significant differences in distances to the modiulus. Interestingly, the space between the basal contacts and the modiulus in the P-patients shows that the contacts are pushed toward and not firmly pressed onto the modiulus, probably because the partially inserted positioner is not completely space filling.

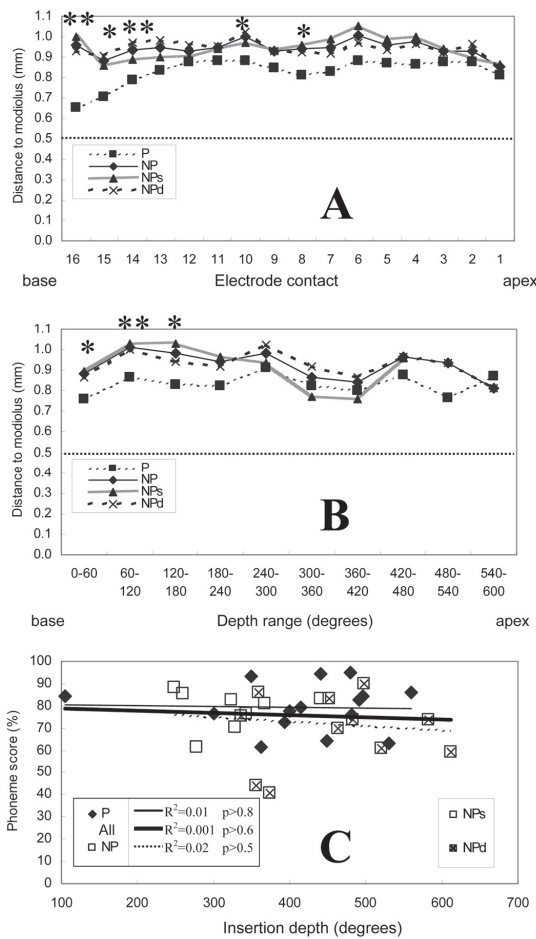


Figure 5. Radial distances of center of electrode contacts to the modiulus, shown per electrode contact (A) and per depth range (B). Significant differences between the P- and NP-groups are marked (* $p < 0.05$; ** $p < 0.01$). Dashed lines reflect the combined contribution to the measured distances of the space between the center and the surface of the contacts, the silicon blebs, located medially on the array between adjacent electrodes, and the average standard error. C, Phoneme scores after 1 yr of follow-up of the positioner group (P) and the non positioner-group (NP) plotted against the insertion depth of the most apical electrode contact. The lack of correlation is shown by trend lines, R^2 and p values. The number of patients in the subgroups is shown for electrode contacts and for the depth ranges in Table 3.

The first 9 NP-patients have a shallow insertion compared to the P-group. The most basal electrode contacts of the NPs-group show a trend to be close to the cochleostomy, with the 16th contact at an insertion angle near 0 degrees (Table 4). Consequently, the electrode contact 16 of those NP-patients is located in the part of the cochlea that is by far the widest part. Therefore, the radial distances of those electrode contacts to the modiolus are larger than those of the same contacts in electrode arrays, which were inserted somewhat further in the cochlea. Moreover, the average location of the apical electrode contacts of the NPs-group is significantly less deep than that of the P-group (327 versus 468 degrees: $p < 0.01$). Although the apical contacts of the NPs- and P-groups are in a clearly different location, the decision to insert deeper made the position of the NPd-group's apical electrode again at a location more comparable to that of the P-group. However, the most basal contact of the NPd-group was located significantly deeper than that of the P-group ($p < 0.01$). All observed differences in insertion depth did not reveal significant correlations with speech perception scores (figure 5C) ($p > 0.5$).

Table 4. Insertion depths of electrode contacts, in degrees as measured on multi slice CT scans

Insertion depths of electrode contacts (degrees)	P-group	NP-group		
	15 of 25	all 20	NPs (n=9)	NPd (n=11)
Most apical	439 (73;105-559)	401 (105;278-612)	327 (60;278-441)*	468 (92;336-612)
Most basal	6 (13;10-35)	35 (41;7-130)*	2 (11;7-25)	65 (35;10-130)

Data are averages with standard deviations of the population and minimal and maximal values between brackets. Significant differences, marked ($p < 0.01$), are between the P-group and the marked NP-group. Position of the cochleostomy can lead to negative values.

To compare the radial distances between groups at the same cochlear location, the electrode contacts were converted to angle of insertion. The radial distances of the electrode contacts to the modiolus for 10 depth ranges are shown in figure 5B. In line with the findings per electrode contact, the radial distances of the electrodes at the 3 basal most depth ranges differ significantly between the P-group and the NP-group (0 to 60 degrees: $p < 0.05$; 60 to 120: $p < 0.01$; 120 to 180: $p < 0.05$), whereas the distances at the apical ranges do not differ significantly ($p > 0.4$). For the different depth ranges in the

cochlea, the radial position of the electrode contacts of the NPs- and NPd-groups were similar.

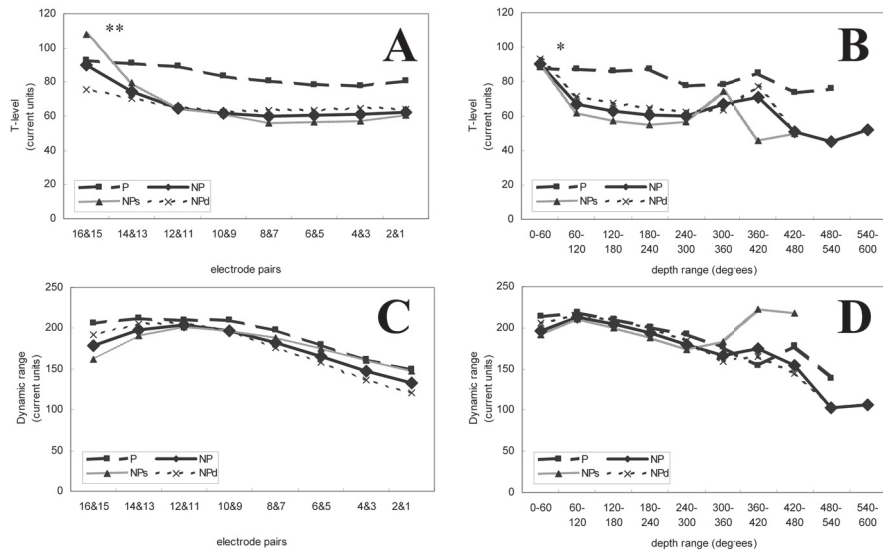


Figure 6. T-levels of the positioner-group (P) and the non positioner-group (NP), shown per electrode contact (A) and per depth range (B). The NP-group is split into the group of the first 9 shallowly inserted patients (NPs) and the last 11 deeper implanted patients (NPd). Significant differences in basal increases in T-levels between the P-group and the NPs-group are marked (* $p < 0.05$; ** $p < 0.01$). C and D show the dynamic range of each group per electrode contact (C) and per insertion range (D). The number of patient in the subgroups is shown for electrode pairs and for the depth ranges in Table 3.

T-levels, M-levels & Dynamic Range

Contrary to the expectations based on the fact that the contacts in the P-group are closer to the nerve fibres in the modiolus, the overall T-levels of the P-group tend to be higher than those of the NP-group, although, this is not statistically significant ($p > 0.3$) (figure. 6A). Wide ranges exist for the T-levels, especially for the P-patients, which can prevent small differences between groups to reach significant levels. Although the inter-individual T-levels vary greatly, the intra-individual T-levels along the array

show great consistency within each group. The T-levels of the P-patients do not show big differences along the array, with slightly higher thresholds basally. The differences along the array are much more profound in the NPs-group, with a sharp increase of the T-levels at the basal side of the array (as seen in figure 6 A). This basal increase in T-level (T-level at contacts 16 and 15 minus T-level at contacts 14 and 13) of the NPs-patients is significantly larger than that of the P-group ($p < 0.01$). The differences in basal T-levels rise between NPs and P are also significant, when the T-levels are plotted per depth range, although with a lower significance level ($p < 0.05$) (figure 6B). In the NPs-group this basal ward increase of T-levels (as a percentage of the average overall level) is significantly correlated with the insertion depth ($p < 0.05$). Together with the reduced growth of speech perception scores, this was an argument to change the operation technique and insert deeper. As was expected, the T-level profile of the NPd-group showed the more even shape of the P-group again (figure 6A). However, the overall T-levels of the NPs- and NPd-groups are at equal levels ($p > 0.9$).

Within each group there is a small but significant negative correlation between the T-levels, averaged per individual, and the speech perception as measured with monosyllabic words ($R = -0.64$, $p < 0.01$, $R = -0.55$, $p < 0.05$, for the P and NP groups, respectively). This means that within groups, patients with lower T-levels tend to have better outcomes. However, this does not hold between groups, as the P-group has better outcomes in spite of slightly higher T-levels.

The M-levels do not show any significant difference between the groups in absolute levels, nor in shape of the profiles. The shape of the M-level profile was set according to our clinical fitting method (Reference Note). Because of the definition of the dynamic range as a subtraction of the M-levels and T-levels, the dynamic range is basally smaller in the NPs-group as a result of the basal increase of the T-levels (figure 6, C and D).

Electrode Impedances and Conductivity Paths

The standard impedance measurements as obtained before initial hook-up show a tendency to be higher at the basal end of the scala tympani for the P-group. More detailed information was obtained with EFI measurements.

Figure 7A shows longitudinal resistances (r_{Long}) along the electrode array as calculated with the EFI-model (Vanpoucke et al., 2004). This r_{Long} shows no significant differences between the patient groups. Differences seen in the depth ranges >360 degrees are mainly due to a limited number of subjects in the subgroups and do not reach significant

levels. The resistances in transversal direction (r_{Trans}) are more than a factor 100 higher than the corresponding r_{Long} values (figure 7B). Therefore, a longitudinal conductivity path along the array will dominate in all groups. As found for longitudinal resistances, the transversal resistances along the array do not show significant differences between the groups. An important factor, as indicated by the EFIM measurements, is the basal resistance (r_{Basal}) (figure 7C), which is at least five times the r_{Long} value in all groups. This is the resistance from the basal contact of the cochlea to the reference electrode contact. This r_{Basal} reveals differences between the subgroups. The basal resistance of the NPs-subgroup is significantly lower than the r_{Basal} of both the P- as the NPd-group. In contrast to the basal resistances, the tissue resistance, the global impedance between a given electrode and ground, does not show significant differences between the P- and NP-group (figure 7D). Moreover, the NPs and NPd show comparable values (not plotted in figure 7D). However, the r_{Tissue} of the NP-patients measured 1 or 2 mos after implantation were lower at the basal side of the cochlea, differing significantly with the data obtained after 1 yr (figure 7D). Also the r_{Long} and r_{Trans} of the NP-group showed this basal increase.

Discussion

In this study, the clinical effects of bringing the HiFocus I electrode array in a perimodiolar position were examined. This study became possible after the withdrawal of the positioner from the market in 2002. Intrascalar position, insertion depth, stimulation levels, and intracochlear conductivity pathways were studied to find an explanation for the decrease in speech perception after implantation without peri-modiolar positioning of the array.

The study shows better speech perception with a perimodiolar electrode design. The learning curve was much steeper in the patients with the perimodiolar electrode (P-group) and their speech recognition reached significantly higher levels from 3 mos up to at least 1 yr. Additionally, significant differences in speech perception in noise were demonstrated. International comparison of the results with other studies showing a perimodiolar position of the Contour electrode contributes to the outcomes is complicated by language-differences (Bacciu et. al, 2005). Comparison of our speech perception results with sparse published data from Dutch cochlear implant users shows that even the NP-patients from this study show speech perception scores which are in

line with or above those using other state-of-the-art cochlear implants (Smootenburg, Willeboer, & Vandijk, 2002). On top of this performance, extra improvement is shown in the patients with the positioner.

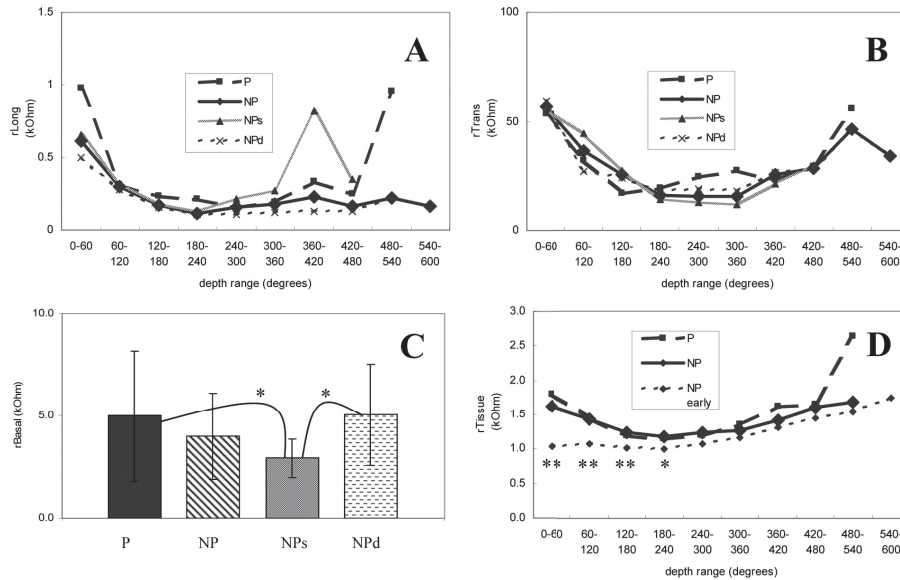


Figure 7. The longitudinal r_{Long} (A) and transversal r_{Trans} (B) resistances per depth range as acquired with the EFI (Electrical Field Imaging) model. C, Basal resistance r_{Basal} represents resistance from the basal electrode contact to the reference contact for all patient groups. Significant differences, marked (* $p < 0.05$; ** $p < 0.01$), are between the P –and the NP-groups, except when indicated differently. D, Average total tissue resistance r_{Tissue} at each electrode contact, one for the P-group and for the NP-group at several months and 1 yr after implantation. Significant differences, marked (* $p < 0.05$; ** $p < 0.01$), are between the NP-early versus the P- and the NP-groups. The number of patients in the subgroups is shown for the depth range in Table 3.

It is of utmost importance to try and understand the causes of the differences found between the groups in this study, especially because the less favourable outcomes were obtained in patients implanted later in time, which at least is not in line with the general trend of continuously improving speech perception with cochlear implants (Ramsden,

2004). Future electrode designs, taking into account these findings, should aim at regaining this improved speech perception.

The first factor analyzed in an attempt to explain the improved speech perception was if the array was really positioned closer to the modiolus in the P-group as intended. This was confirmed with the MSCT scan technique developed in our center (Verbist et al., 2005). In line with the findings of Balkany et al. (2002), the data from this study show that the approximation with the positioner takes place primarily at the basal side of the cochlea, whereas the apical contacts follow the lateral wall. Although this basal decrease to the modiolus is small, it accounts for a considerable part of the free space between the electrode array and the modiolus as seen in the NP-patients. Improved speech perception confirmed the benefits of this position as expected on the basis of computational models of the cochlea (Frijns et al., 2001).

Additionally, with the positioner pushing the electrode towards the inner curvature of the scala tympani, a deep insertion could be reached, with the most basal electrodes still in the most basal region of the cochlea. This position in the cochlea could contribute to the higher speech perception scores in the P-group compared to the NP-group. The potentially beneficial effects of stimulation along the entire cochlea have been suggested earlier (Hochmair et al., 2003), because it could allow for a more natural frequency to place mapping. This might facilitate speech perception, which is in line with the findings reported by Baskent & Shannon (2003). Furthermore, if a certain area in the cochlea has suffered neural cell death, stimulation of other parts of the cochlea is still possible with this large insertion length. After the shallow insertion of the first 9 patients without a positioner, it was aimed to regain the higher speech perception scores as obtained by the P-group through a deeper insertion. Although the threshold for the basal electrode contact decreased with a deeper insertion for the NP- patients, the NPd-patients did not show significant speech perception scores after 1 wk compared to the NPs-patients. Regarding the value of apical stimulation, researchers report contrasting results. Some studies described a significant contribution of the most apical regions to speech perception (Hochmair et al., 2003; Yukawa et al., 2004), but other ones showed improved speech perception with the most apical contacts turned off (Boëx, Kos, & Pelizzone, 2003).

In the present study, there are few (if any) confounding variables that can explain the improved performance in the P-group, rather than the use of the positioner itself. Of course the groups with and without positioner were separated in time, the separation

being marked by the withdrawal of the positioner in July 2002. Although this made randomisation of the patients over the groups impossible, the patient groups were demographically highly comparable (Table 1). Moreover, the selection criteria, the surgeon and the rehabilitation scheme were the same for both groups. The follow-up of both groups took place in a prospective way with the same tests at predetermined intervals. The higher average age at implantation in the NP-group was the only significant demographic difference between the groups. However, this age difference is not likely to explain the differences in speech perception, for no correlation was observed between age at implantation and speech perception within each of the groups. This finding is in line with a recent multi-centre study, which also showed no systematic association of speech perception with age at implantation (UK Cochlear Implant Study Group, 2004). Additionally, the different amount of usage of HiRes programs between the P- and NP-groups is not a very likely explanation for the differences in speech perception in silence. In line with previous research performed in our clinic (Frijns, Klop, Bonnet, & Briaire, 2003) and elsewhere (Friesen, Shannon & Cruz, 2005) the present study did not reveal any significant effect of high rate stimulation or number of electrodes used on speech perception in quiet for both groups ($p > 0.2$ and $p > 0.3$ for the P- and NP-groups, respectively). Moreover, the average time of experience with those HiRes strategies was the same at 1 year (P versus NP: 8 mos).

As reported elsewhere (Reference Note), the duration of deafness is not a predictor of post-operative performance in the P-group. The data in the present study lead to the same observation for the NP-group, excluding the positioner as a cause for the lack of correlation between duration of deafness and performance. This is a surprising outcome, which is in contrast with the majority of previous studies (Gomaa, Rubinstein, Lowder, Tyler, & Gantz, 2003; UK Cochlear Implant Study Group, 2004; van Dijk et al., 1999); and in line with a few others (Hamzavi, Baumgartner, Pok, Franz, & Gstoettner, 2003). Interestingly, the lack of correlation persists in the total group with both P- and NP-patients, even if the three meningitis cases in both groups are excluded from the analysis.

In an attempt to understand the implications of the changed intrascalar position on speech perception, physiological features expected to underlie these implications, such as stimulation levels, were examined in this study. Literature describes lower thresholds and higher amplitudes as seen with acute EABR, eCAP, and stapedius reflex measurements (Cords et al., 2000; Eisen & Franck, 2004; Firszt et al., 2003; Mens et al., 2003; Pasanisi et al., 2002; Wackym et al., 2004,) after modiolar approximation of

the electrode. Moreover, findings for the Clarion Preformed electrode and the Nucleus Contour electrode reported lower perception thresholds (Cohen et al., 2003; Parkinson et al., 2002; Saunders et al., 2002; Tykocinski et al., 2001; Young & Grohne, 2001;). Although the positioner pushed the electrode array toward the modiolus, as confirmed by the post-operative MSCT scans, the threshold and maximum comfort levels were not lower in the P-group (figure 6). A firm explanation for the lack of reduction of the stimulation levels was not found. However, a possible explanation for the stable stimulation levels can be the improved spatial selectivity associated with the basally perimodiolar position. With such a position the stimulation threshold of the nerve fibres closest to the electrode contact may be reduced (as predicted by Frijns et al., 2001), but in the meantime the increased spatial selectivity may cause fewer nerve fibres along the cochlea to contribute to the percept, which, consequently, may still be unperceivably soft. Hughes (2003) also showed stable T-levels with the Nucleus Contour electrode compared to its straight predecessor. As a plausible additional effect, she suggested that temporal integration mechanisms might be responsible for determination of T-levels instead of electrode position in the cochlea.

Since the beneficial effects of the positioner are not due to changes in stimulation levels, other factors must be involved. The improvement in speech perception from a perimodiolar design may then be primarily due to improved spatial selectivity. Better performance in electrode discrimination correlates with improvements in speech perception (Busby et al., 1993) and modiolar approximation produces improvements in the outcomes of psychophysical forward masking measurements (Cohen et al., 2001). Although promising, eCAP measurements, have not been able to link changed spatial selectivity profiles with speech perception (Cohen et al., 2003; Hughes, 2003). Such objective information about the spatial selectivity, obtained with NRI-recordings, was not collected routinely in the patients reported here. Therefore, such data are only available for some individual patients and no conclusions for the groups could be drawn.

The EFIM measurements, reflecting the local electrical conductivity of the cochlear tissues, do not give a clear explanation for the improved speech perception in the P-group. The insulating silastic positioner seems to have a limited effect on the current flow in the cochlea. However, the lack of such an insulating positioner seems to cause lower basal resistance values in the NPs-patients, which might cause injected current to flow easily out of the basal cochlea. This could explain why basal electrodes were less potent in stimulating nerve fibres in the NPs-group, which, in turn, can explain

why these patients have higher thresholds at basal contacts. Deeper insertion of the electrode arrays causes the basal current leak to decrease to the level of the P-patients. Besides the depth of insertion, the time passed since the implantation seems to increase the impedances, whereas repeated measures in the NP-patients showed significant increase in the resistors basally. The higher resistances occur especially in the wider basal part of the cochlea and might be due to postimplantational accumulation of scar tissue. However, densitometry-measurements made in our clinic after 6 mos showed no differences with the CT-scans obtained immediately after surgery. EFIM measurements of resistances obtained after the 1-yr measurements showed stable situations. Because we did not perform the early EFIM measures in the P-patients, we could not confirm if the insulating positioner caused initially higher impedances compared to impedances of the NP-patients, as shown by the trend in the standard impedance measures, or that this occurred due to fibrosis during the first year as likely in the NP-patients.

In the future, more research has to be carried out to find the factors that have functional implications on speech perception with cochlear implants and in which way those factors can be favorably manipulated in future cochlear implant designs. The patients who are currently being implanted with the long HiFocus 1J electrode connected to the same implanted electronics can help to elucidate the effect of deeper insertion. Furthermore, spatial selectivity measurements with NRI/NRT and studies with an improved computational model can presumably give more insight in the role of spatial selectivity in speech perception and how this spatial selectivity can be influenced by future electrode designs.

The data in the present study influenced the design of future electrodes. We believe that it will be beneficial to have an electrode array, which has insulating silastic along the back of the array at the basal side giving it only basally a perimodiolar position, apically a lateral position and a full insertion depth. The HiFocus4L electrode is a single component implant (Frijns, Briaire, Zarowski, Verbist, & Kuzma, 2004), designed to meet these criteria and to regain the speech perception as was achieved with the perimodiolar array with a partially inserted positioner. The clinical results of the patients implanted with these new devices will help to complete more parts of the puzzle.

Conclusion

Speech perception is favorably influenced by a basally perimodiolar electrode position. The change in radial distance, insertion depth and insulating properties probably all contribute to the improved speech perception found with the HiFocus I electrode with separate positioner. These improved speech perception levels should be regained using the insights obtained from the patients implanted with various perimodiolar implants. Further research has to elucidate the individual contributions of the properties of specific perimodiolar designs.

Acknowledgements

This research was financially supported by grants from Advanced Bionics Corp., Sylmar, CA and the Heinsius Houbolt Fund. The authors wish to thank Jay Rubinstein, Boerhaave Professor at the Leiden University Medical Centre in 2003 to 2004, for the valuable comments on an earlier draft of the manuscript and Filiep Vanpoucke of Advanced Bionics Europe, Antwerp, Belgium, for his contribution to the EFI-modeling.

References

- Bacciu, A., Pasanisi, E., Vincenti, V., Guida, M., Barbot, A., Berghenti, M., Forli, F., Berrettini, S., & Bacciu, S. (2005). Comparison of speech perception performance between the Nucleus 24 and Nucleus 24 Contour cochlear implant. *Acta Otolaryngol.*, 124, 1155-1158.
- Balkany, T. J., Eshraghi, A. A., & Yang, N. (2002). Modiolar proximity of three perimodiolar cochlear implant electrodes. *Acta Otolaryngol.*, 122, 363-369.
- Baskent, D. & Shannon, R. V. (2003). Speech recognition under conditions of frequency-place compression and expansion. *J.Acoust.Soc.Am.*, 113, 2064-2076.
- Boex, C., Kos, M. I., & Pelizzone, M. (2003). Forward masking in different cochlear implant systems. *J.Acoust.Soc.Am.*, 114, 2058-2065.
- Bosman, A. J. & Smoorenburg, G. F. (1995). Intelligibility of Dutch CVC syllables and sentences for listeners with normal hearing and with three types of hearing impairment. *Audiology*, 34, 260-284.
- Busby, P. A., Tong, Y. C., & Clark, G. M. (1993). Electrode position, repetition rate, and speech perception by early- and late-deafened cochlear implant patients. *J.Acoust.Soc.Am.*, 93, 1058-1067.
- Chen, J. M., Farb, R., Hanusaik, L., Shipp, D., & Nedzelski, J. M. (1999). Depth and quality of electrode insertion: a radiologic and pitch scaling assessment of two cochlear implant systems. *Am.J.Otol.*, 20, 192-197.
- Cohen, L. T., Richardson, L. M., Saunders, E., & Cowan, R. S. (2003). Spatial spread of neural excitation in cochlear implant recipients: comparison of improved ECAP method and psychophysical forward masking. *Hear.Res.*, 179, 72-87.
- Cohen, L. T., Saunders, E., & Clark, G. M. (2001). Psychophysics of a prototype peri-modiolar cochlear implant electrode array. *Hear.Res.*, 155, 63-81.
- Cohen, N. L., Roland, J. T., Jr., & Marrinan, M. (2004). Meningitis in cochlear implant recipients: the North American experience. *Otol.Neurotol.*, 25, 275-281.
- Cords, S. M., Reuter, G., Issing, P. R., Sommer, A., Kuzma, J., & Lenarz, T. (2000). A silastic positioner for a modiolar-hugging position of intracochlear electrodes: electrophysiologic effects. *Am.J.Otol.*, 21, 212-217.
- Eisen, M.D., & Franck, K.H. (2004). Electrically evoked compound action potential amplitude growth functions and HiResolution programming levels in pediatric CII implant subjects. *Ear Hear.*, 25, 528-538.
- Fayad, J. N., Luxford, W., & Linthicum, F. H. (2000). The Clarion electrode positioner: temporal bone studies. *Am.J.Otol.*, 21, 226-229.
- Firszt, J. B., Wackym, P. A., Gaggl, W., Burg, L. S., & Reeder, R. M. (2003). Electrically evoked auditory brain stem responses for lateral and medial placement of the Clarion HiFocus electrode. *Ear Hear.*, 24, 184-190.
- Friesen, L.M., Shannon, R.V., & Cruz, R.J. (2005). Effects of stimulation rate on speech recognition with cochlear implants. *Audiol.Neurotol.*, 10, 169-184.

- Frijns, J. H. M., Briaire, J. J., de Laat, J. A. P. M., & Grote, J. J. (2002). Initial evaluation of the Clarion CII cochlear implant: speech perception and neural response imaging. *Ear Hear.*, 23, 184-197.
- Frijns, J. H. M., Briaire, J. J., & Grote, J. J. (2001). The importance of human cochlear anatomy for the results of modiolar-hugging multichannel cochlear implants. *Otol.Neurotol.*, 22, 340-349.
- Frijns, J. H. M., Briaire, J. J., Zarowski, A., Verbist, B., & Kuzma, J. Concept and initial testing of a new, basally perimodiolar electrode design. In Myamoto, R (ed.), *Cochlear Implants, International Congress Series*, 1273
- Frijns, J. H. M., de Snoo, S. L., & Schoonhoven, R. (1995). Potential distributions and neural excitation patterns in a rotationally symmetric model of the electrically stimulated cochlea. *Hear. Res.*, 87, 170-186.
- Frijns, J. H. M., de Snoo, S. L., & ten Kate, J. H. (1996). Spatial selectivity in a rotationally symmetric model of the electrically stimulated cochlea. *Hear.Res.*, 95, 33-48.
- Frijns, J. H. M., Klop, W. M., Bonnet, R. M., & Briaire, J. J. (2003). Optimizing the number of electrodes with high-rate stimulation of the clarion CII cochlear implant. *Acta Otolaryngol.*, 123, 138-142.
- Goma, N. A., Rubinstein, J. T., Lowder, M. W., Tyler, R. S., & Gantz, B. J. (2003). Residual speech perception and cochlear implant performance in postlingually deafened adults. *Ear Hear.*, 24, 539-544.
- Hamzavi, J., Baumgartner, W. D., Pok, S. M., Franz, P., & Gstoettner, W. (2003). Variables affecting speech perception in postlingually deaf adults following cochlear implantation. *Acta Otolaryngol.*, 123, 493-498.
- Hochberg, I., Boothroyd, A., Weiss, M., & Hellman, S. (1992). Effects of noise and noise suppression on speech perception by cochlear implant users. *Ear Hear.*, 13, 263-271.
- Hochmair, I., Arnold, W., Nopp, P., Jolly, C., Muller, J., & Roland, P. (2003). Deep electrode insertion in cochlear implants: apical morphology, electrodes and speech perception results. *Acta Otolaryngol.*, 123, 612-617.
- Hughes, M. L. (2003). The relationship between electrophysiologic measures of channel interaction and electrode discrimination ability in cochlear implant recipients. Ph.D.Thesis, University of Iowa, USA
- Lefrancois, R. D. & Moran, L. M. (2003). Bacterial meningitis in children with cochlear implants. *N.Engl.J.Med.*, 349, 1772-1773.
- Marrinan, M. S., Roland, J. T., Jr., Reitzen, S. D., Waltzman, S. B., Cohen, L. T., & Cohen, N. L. (2004). Degree of modiolar coiling, electrical thresholds, and speech perception after cochlear implantation. *Otol.Neurotol.*, 25, 290-294.
- Mens, L. H., Boyle, P. J., & Mulder, J. J. (2003). The Clarion Electrode positioner: approximation to the medial wall and current focussing? *Audiol.Neurootol.*, 8, 166-175.
- Nadol, J. B., Jr. & Eddington, D. K. (2004). Histologic evaluation of the tissue seal and biologic response around cochlear implant electrodes in the human. *Otol.Neurotol.*, 25, 257-262.

- Parkinson, A. J., Arcaroli, J., Staller, S. J., Arndt, P. L., Cosgriff, A., & Ebinger, K. (2002). The nucleus 24 contour cochlear implant system: adult clinical trial results. *Ear Hear.*, 23, 41S-48S.
- Pasanisi, E., Vincenti, V., Bacciu, A., Guida, M., & Bacciu, S. (2002). The nucleus contour electrode array: an electrophysiological study. *Laryngoscope*, 112, 1653-1656.
- Ramsden, R. T. (2004). Prognosis after cochlear implantation. *BMJ*, 328, 419-420.
- Reefhuis, J., Honein, M. A., Whitney, C. G., Chamany, S., Mann, E. A., Biernath, K. R. et al. (2003). Risk of bacterial meningitis in children with cochlear implants. *N.Engl.J.Med.*, 349, 435-445.
- Richter, B., Aschendorff, A., Lohnstein, P., Husstedt, H., Nagursky, H., & Laszig, R. (2002). Clarion 1.2 standard electrode array with partial space-filling positioner: radiological and histological evaluation in human temporal bones. *J.Laryngol.Otol.*, 116, 507-513.
- Roland, J. T., Jr., Fishman, A. J., Alexiades, G., & Cohen, N. L. (2000). Electrode to modiolus proximity: a fluoroscopic and histologic analysis. *Am.J.Otolaryngol.*, 21, 218-225.
- Saunders, E., Cohen, L., Aschendorff, A., Shapiro, W., Knight, M., Stecker, M. et al. (2002). Threshold, comfortable level and impedance changes as a function of electrode-modiolar distance. *Ear Hear.*, 23, 28S-40S.
- Shepherd, R. K., Hatsushika, S., & Clark, G. M. (1993). Electrical stimulation of the auditory nerve: the effect of electrode position on neural excitation. *Hear.Res.*, 66, 108-120.
- Smoorenburg, G.F., Willeboer, C., & van Dijk, J.E. (2002). Speech perception in nucleus C124M cochlear implant users with processor settings based on electrically evoked compound action potential thresholds. *Audiol & Neurotol*, 7, 335-347.
- Tykocinski, M., Cohen, L. T., Pyman, B. C., Roland, T., Jr., Treaba, C., Palamara, J. et al. (2000). Comparison of electrode position in the human cochlea using various perimodiolar electrode arrays. *Am.J.Otol.*, 21, 205-211.
- Tykocinski, M., Saunders, E., Cohen, L. T., Treaba, C., Briggs, R. J., Gibson, P. et al. (2001). The contour electrode array: safety study and initial patient trials of a new perimodiolar design. *Otol.Neurotol.*, 22, 33-41.
- UK Cochlear Implant Study Group (2004). Criteria for candidacy for unilateral cochlear implantation in postlingually deafened adults I: Theory and measures of effectiveness. *Ear Hear.*, 25, 310-335.
- van Dijk, J. E., van Olphen, A. F., Langereis, M. C., Mens, L. H., Brokx, J. P., & Smoorenburg, G. F. (1999). Predictors of cochlear implant performance. *Audiology*, 38, 109-116.
- Vanpoucke, F., Zarowski, A., Casselman, J., Frijns, J. H. M., & Peeters, S. (2004). The facial nerve canal: an important cochlear conduction path revealed by Clarion electrical field imaging. *Otol.Neurotol.*, 25, 282-289.
- Verbist, B. M., Frijns, J. H. M., Geleijns, K., & van Buchem, M. A. (2005) Multisection CT as a valuable tool in the postoperative assessment of cochlear implant patients. *AJNR*, 26, 424-429.
- Wackym, P. A., Firszt, J. B., Gaggl, W., Runge-Samuelson, C. L., Reeder, R. M., & Raulie, J. C. (2004). Electrophysiologic effects of placing cochlear implant electrodes in a perimodiolar position in young children. *Laryngoscope*, 114, 71-76.
- Young, N.M., & Grohne, K.M. (2001). Comparison of pediatric Clarion recipients with and without the electrode positioner. *Otol.Neurotol.*, 22, 195-199.

- Yukawa, K., Cohen, L., Blamey, P., Pyman, B., Tungvachirakul, V., & O’Leary, S. (2004). Effects of Insertion Depth of Cochlear Implant Electrodes upon Speech Perception. *Audiol. Neurootol.*, 9, 163-172.

Reference note

- Briaire, J.J., Frijns, J.H.M. (2003). New insights in the fitting strategy for adults and children. 2003 Conference on Implantable Auditory Prostheses, Asilomar, 189.

5

Consensus Panel on a Cochlear Coordinate System Applicable in Histological, Physiological and Radiological Studies of the Human Cochlea

BM Verbist, MW Skinner, LT Cohen, PA Leake, C James, C Boëx,
TA Holden, CC Finley, PS Roland, JT Roland, M Haller, JF Patrick,
CN Jolly, MA Faltys, JJ Briaire, JHM Frijns

Otology & Neurotology, in press

Abstract

Hypothesis: An objective cochlear framework, for evaluation of the cochlear anatomy and description of the position of an implanted cochlear implant electrode, would allow the direct comparison of measures performed within the various sub-disciplines involved in cochlear implant research.

Background: Research on the human cochlear anatomy in relation to tonotopy and cochlear implantation is conducted by specialists from numerous disciplines such as histologists, surgeons, physicists, engineers, audiologists and radiologists. To allow accurate comparisons between and combinations of previous and forthcoming scientific and clinical studies, cochlear structures and electrode positions must be specified in a consistent manner.

Methods: Researchers with backgrounds in the various fields of inner ear research as well as representatives of the different manufacturers of cochlear implants (Advanced Bionics Corp, Med-El, Cochlear Corp) were involved in consensus meetings held in Dallas, March 2005 and Asilomar, August 2005. Existing coordinate systems were evaluated and requisites for an objective cochlear framework were discussed.

Results: The consensus panel agreed upon a 3-dimensional, cylindrical coordinate system of the cochlea using the “Cochlear View” as a basis and choosing a z-axis through the modiolus. The zero reference angle was chosen at the centre of the round window, which has a close relationship to the basal end of the Organ of Corti.

Conclusions: Consensus was reached on an objective cochlear framework, allowing the outcomes of studies from different fields of research to be compared directly.

Introduction

Over the years researchers from different fields have been particularly interested in unraveling the anatomic substrates of the tonotopic organization of the cochlea, most recently in regard to cochlear implantation. Several techniques for estimation of the exact intracochlear position of a cochlear implant electrode array have been described and applied. Histopathologists, surgeons and radiologists used different methods, each meeting the specific needs in their field of research. However, the existing methods posed several problems regarding objectivity, influence of cochlear size and shape and combined applicability for histological, surgical as well as psychophysical studies. This has traditionally led to different descriptions of electrode positions across and even within sub-disciplines. Therefore there was a need for an objective cochlear framework.

To address these problems two consensus meetings were held in Dallas, March 2005 and in Asilomar, August 2005. A panel of researchers with backgrounds in the various fields (C Boëx, JJ Briaire, LT Cohen, CC Finley, JHM Frijns, C James, PA Leake, PS Roland, T Roland, MW Skinner, BM Verbist), as well as representatives of the different manufacturers of cochlear implants (MA Faltys (Advanced Bionics, Sylmar, California, USA), JF Patrick (Cochlear, Sydney, Australia), C Jolly (Med El, Innsbruck, Austria)), discussed the need for a universal, objective coordinate system.

From a frequency analysis point of view the organ of Corti (OC) is the most important cochlear anatomic structure. It has been used as point of reference in many studies on cochlear anatomy and function. The tonotopic organization of the cochlea, for instance, has been mathematically characterized by Greenwood. He studied the frequency-position relation for acoustic stimulation in various mammalian species. The exponential formula he postulated gives characteristic frequencies of acoustic sensitivity (in Hz) as function of fractional length of the OC (measured from the helicotrema). [1-3] These same frequency distributions are now used in cochlear implants to map the frequency distribution as a function of length along the array, implying that the insertion depth of the electrode array and the position of the individual contacts relative to the OC will determine the perceived pitch in cochlear implant patients. Numerous studies on pitch sensation have, however, shown that the cochlear frequency-position map does not accurately predict the pitch sensation produced by electrical stimulation of an electrode, even if high electrical stimulation rates are used to rule out any influence of the stimulation rate. [4-8] Boëx et al. [7] showed that pitch sensations were found to

be more than 1 octave (using insertion angle) or more than 2 octaves (using insertion lengths) lower than predicted by Greenwood's frequency position.

One possible factor contributing to the down shift of pitch in relation to Greenwood's function is the site of neural activation. Peri-modiolar cochlear implants are designed to stimulate the auditory nerve at the level of the spiral ganglion instead of the peripheral process. [9,10] It has been reported that there is an angular offset between the position of the basilar membrane and that of the associated ganglion cells, particularly in the apical third of the cochlea. [11,12] Sridhar et al. [10] determined the spiral ganglion map by tracing the fiber trajectories in temporal bones and found that the fibers in the extreme base and apex do not follow a radial trajectory. To overcome the shorter length of the spiral ganglion in relation to the OC there is a compression of the frequency map at low frequencies. [10,13] Thus the shift would become pronounced only at a deep insertion (beyond 450 degrees insertion depth in CView[®] (see below), personal communication Cohen, based on analysis of data provided by Pat Leake).

Since the length of the OC cannot be directly determined in most temporal bone and imaging studies an objective cochlea framework closely related to the OC is needed. This framework should be easily applicable for all subspecialties involved in cochlear research and patient care. By introducing such a cochlear coordinate system, results from a given field could be more easily translated to or combined with results from other fields of hearing research. The consensus panel discussed the requirements for such a framework and evaluated existing coordinate systems in this context.

Rationale of the various components of a cochlear framework

Angular or linear measurement

Cochlear implant insertion depth has been described either in terms of linear distance (in mm) or insertion angle (in degrees).

From the surgeon's and histopathologist's view much is to be said for the use of linear measurements. Such a measurement provides the surgeon with an immediate estimate of the result, e.g., in terms of the number of contacts inserted into the cochlea. Results in a longitudinal system can potentially be correlated to a fixed structure such as the OC or the electrode array. Yet, as described above, difference in stimulation site and compression of the spiral ganglion relative to the OC would possibly require

corrections, especially at the apex and extreme base. Moreover, it is necessary to have reliable measures of both the length of the OC and the intracochlear position of the array. However, as mentioned before, the length of the OC cannot be determined in most temporal bone and imaging studies and there is a great intersubject variability of cochlear length as well as differences in OC length. [12,14-19] The actual values differ between authors. Sato reported a mean cochlear length of 37.1 ± 1.6 mm in males and of 32.3 ± 1.8 mm in females. [20] The inter-gender variability reported by Sato was not confirmed in Ketten's and, later, in Skinner's and Stakhovskaya's studies. [13,16,17] Moreover, the intracochlear trajectory of an electrode array differs between straight designs and perimodiolar designs. Two implants with the same insertion depth measured in mm along the array but with a different position in relation to the outer wall of the scala tympani, will potentially reach considerably different characteristic frequencies. If, however, the insertion length can be correlated to the OC, a much better result will be obtained: thus longitudinal insertion depth expressed as percentage length along the OC is a viable alternative approach.

Others favour the use of angular measurements in which allowance is made for individual cochlear dimensions as well as intracochlear trajectories of cochlear implant electrodes. Based upon temporal bone studies, Bredberg correlated angular measurements to the distance along the basilar membrane (along the organ of Corti). [14] He referred to an origin at the helicotrema. According to Kawano et al. [12] the use of the helicotrema (= apex modioli) as a reference to define an axis could lead to significant error since the OC is eccentric to the helicotrema. Kawano et al. therefore used only points in the OC coordinate set without an axis of revolution. This resulted in slightly shorter percentage lengths. An estimate of the characteristic frequency associated with the position of each electrode can be derived from the data of Bredberg and the formula of Greenwood. Stakhovskaya et al have shown that measurements of the percentage distance of the OC and spiral ganglion required to reach specific angles of rotation along the cochlea exhibited considerably less intersubject variability than the absolute distances in millimeters. [13]

A consensus was reached on a cylindrical coordinate system because of the above-mentioned reasons and the already widely applied angular coordinates. Requisites for a cylindrical coordinate system are a plane of rotation, location of the z-axis, including the locations of zero for the z-axis and zero degrees for the angle.

Plane of rotation

In both histological and radiological studies, approaches have been described for measurement of cochlear volume [13,21] and angle [7,22,23]. These approaches have a plane of rotation along the basal turn of the cochlea in common. In this x-y plane, a polar coordinate system can be applied and angular measurements can be performed.

In conventional X-rays this was achieved by the introduction of the Cochlear View by Marsh and coworkers. [23] This modification of the Stenver's view results in an optimal view of the cochlea, perpendicular to the basal turn and along the modiolar axis. Recent technological advances in the field of computer tomography imaging allow reconstructions to be made in any desired plane without loss of image quality. Multiplanar reconstructions or minimum intensity projections along the basal turn of the cochlea and perpendicular to the modiolus result in the equivalent of the "Cochlear View". [21,24]

Histological cochlear dissections are often performed in the plane of the basilar membrane, for instance to perform fiber tracings [13]: this procedure equals the Cochlear View plane for the basal turn and approximates it for the higher turns, which are separated during the procedure.

The panel agreed upon using the Cochlear View as described by Xu and colleagues [25] as a basis for a grid system for the morphological assessment of the inner ear.

Origin of the z-axis

As long as measurements are performed in a 2-dimensional polar coordinate system, the height of the cochlea is not taken into account, which could lead to underestimation of the insertion depth. To obtain direct information on the vertical trajectory of the cochlear lumen and its contents, the framework has to be extended with the 3rd dimension.

The z-axis, perpendicular to the Cochlear View plane, needs to be placed through the center of the modiolus to prevent locations in the cochlear duct that are very close to the modiolus from jumping by 180°, to the other side of the z-axis. Kós, Boëx et al [26] corrected for misaligned x-rays by shifting the center of rotation for their angular measurements to circumvent these angular jumps, and in this way they mimicked positioning the z-axis through the center of the modiolus.

In volume images, an axis through the center of the modiolus can be directly applied. Skinner and coworkers have found that the best choice of axis position occurs when it is matched to the tightest coiling of the cochlea in the upper 1.5 turns.

Along this z-axis an origin has to be defined. There are two main options for the origin of the z-axis, either at the level of the basal turn or in the most apical turn at the helicotrema. The origin needs to be defined accurately and reproducibly. Because the basal turn is not completely flat and the OC is not visible in all recording techniques, this does not seem to be an easily reproducible option. The location where the defined z-axis leaves the bony modiolus, on the other hand, is well visualized and is presumably located at the height of the helicotrema. This point will be used to set the origin of the z-axis. The direction towards the apex is considered positive.

Extension of the framework into a 3-dimensional cylindrical coordinate system, by adding a z-axis through the centre of the modiolus with its origin at the helicotrema, ensures that all spatial information is represented.

Zero reference angle

The main discussion, and also the point where most existing methods differ, is the zero reference angle. For frequency mapping purposes the zero angle ideally would be placed at the basal end of the OC or the spiral ganglion cells (SG). Histopathologists can directly visualize these structures and they can be identified on high resolution images such as micro CT and orthogonal-plane fluorescence optical sectioning (OPFOS) microscopy. However, with currently available clinical imaging techniques the OC or SG cannot be seen. Therefore, an anatomical structure with a known relationship to the basilar membrane would be a desirable landmark. The round window is very close to the end of the OC. Based on registered micro-CT, OPFOS microscopy and CT images of an isolated temporal bone, Skinner et al measured the distance from the midpoint of the proximal basal turn of the cochlea at the level of the anterior round window to the end of the OC to be 2.7mm or 12°. This corresponds well to the mean length of the hook region (2.5mm). [27]

In order to use an easily visualized landmark in close relationship to the basilar membrane, the panel agreed that the zero angle would be chosen at the level of the centre of the round window. In accordance with the right-hand rule, positive angles will be used in the right ear and negative values in the left ear.

The cochlear coordinate system

In summary the defined coordinate system uses the Cochlear View, the plane through the basal turn of the cochlea and perpendicular to the modiolus as plane of rotation. The z-axis is placed through the center of the modiolus, with its origin at the level of the helicotrema. As zero reference angle, the centre of the round window is used (figure 1).

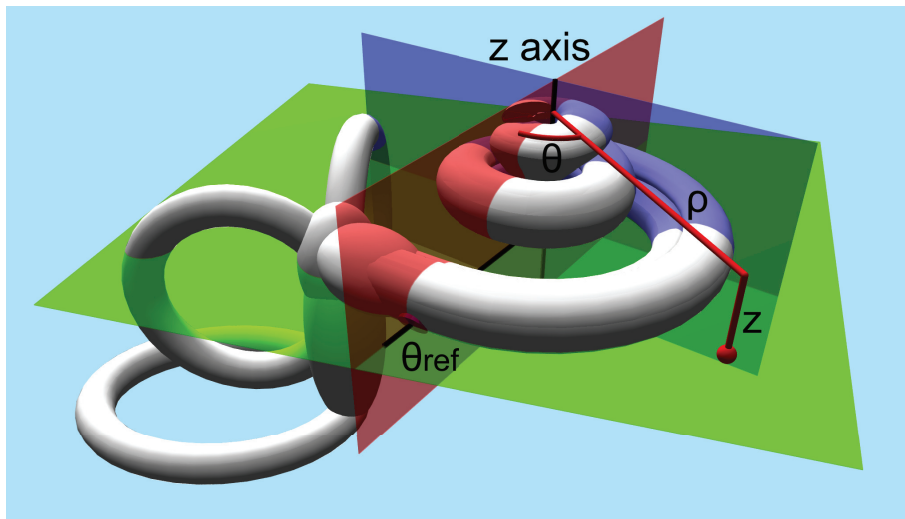


Figure 1. Schematic drawing of the defined cochlear coordinate system: the plane through the basal turn of the cochlea and perpendicular to the modiolus is chosen as the plane of rotation (green plane). The z-axis is placed through the center of the modiolus (crossing of the red en blue plane), with its origin at the level of the helicotrema. As 0 reference angle (θ_{ref}) the centre of the round window is chosen (red plane). Measurements will be defined by rotational angle θ and distance to the modiolus ρ .

By convention measurements will render positive values in the right ear and negative values in the left ear.

The coordinate system does not depend on a mathematical function. Even with different approaches to modelling the human cochlea it can be applied in order to provide comparisons of outcomes. Whether a non-parametric method is used, the cochlear spiral is fitted by the Archimedian spiral [16] or with the helico-spiral model – which has been claimed to provide a closer fit [28] the consensus coordinate system still can be applied.

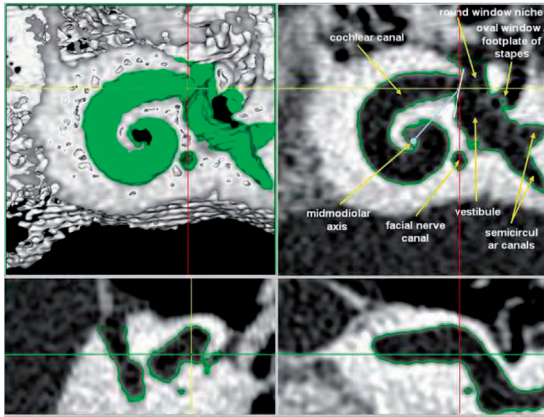


Figure 2. 3D coordinate system according to Washington University in St. Louis: images from the volume render ortho tool in ANALYZE of the body donor’s Volume Zoom 3D volume. Upper left panel is a rendering of the 3D volume thresholded to display only bone with the upper turns of the cochlea cut away; it represents the boundary of the fluid/tissue containing spaces that are surrounded by bone. The other 3 panels are gray scale images of the intersecting orthogonal sections for the selected point on the rendered image, marked by the intersection of the yellow and red lines on the rendered image. The green outline in the other 3 panels shows this boundary between bone and fluid/tissue containing spaces. Upper right panel’s image is perpendicular to the modiolar axis (light blue dot) and shows the demarcation of the vestibule and the cochlear canal (white line) as well as the zero degree rotation line (light blue line).

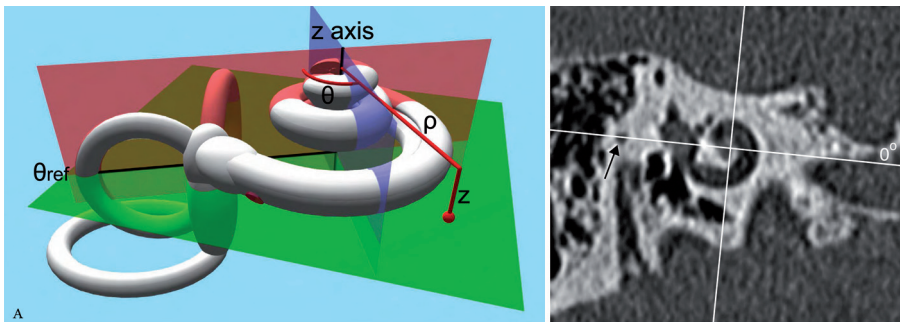


Figure 5. CT-derived cochlear coordinates: **A)** a schematic drawing shows that the x,y,z –axes are applied comparable to figure 1. The zero degree reference angle (θ_{ref}) is however chosen at the top of the horizontal SCC. **(B)** 1 reformatted CT image out of a stack of images through the cochlea is shown. The x,y-axes are shown in red and blue respectively. The x-axis is positioned through the most lateral point of the horizontal SCC, which serves as the 0°-angle in the 3 coordinate system.

Existing coordinate systems

3D template-based method (Washington University in St. Louis)

Computed tomography images provide much more cochlear anatomic detail than conventional X-rays and allow for direct visualization of the round window and even fine intracochlear anatomic structures, such as the modiolus and the walls of the cochlear duct. For a long time, however, it seemed that image degradation on postoperative imaging after cochlear implantation due to metallic artifacts could not be dealt with successfully. Skinner, Ketten and co-workers [16,29] were the first to report on assessment of the intracochlear implant position based on spiral computed tomography imaging *in vivo*. Two methods were used to estimate (linear) insertion depths. First a 3D calculation of length based on individual spiral fits to 2D CT mid-modiolar images was performed. The Archimedian spiral, providing a close fit for the midline of the mammalian cochlear canal, was used to model the human cochlea. [16] Second, automated computerized calculations from 3D visualization of the array obtained by segmenting for electrode attenuation properties were employed. Wang's unwrapping algorithm [30] was designed to track the center of mass of a curvilinear structure in predetermined, small steps. Co-registration of a preoperative and a postoperative dataset and segmentation of the electrode array with substantial interactive profiling of individual scans and reconstruction need to be done to perform these measurements. The results proved that significant variations in cochlear anatomy and array distribution among implant patients, which may impact implant performance, can be reliably detected and quantified by using *in vivo* high-resolution CT and 3-D reconstructions.

Recently Skinner and Whiting and co-workers [27,31] described a new technique for determining the position of cochlear implants, applied to spiral CT. A preoperative and a postoperative volume CT scan are co-registered. This composite image is then compared with a template from three image volumes (standard clinical spiral CT, micro-CT and OPFOS microscopy) from a single normal-hearing donor cochlea. This improved the selection of the midmodiolar axis and the judgment of the position of each electrode within the cochlea. The angular rotation zero degrees starting point is a line joining the midmodiolar axis with the center of the beginning of the cochlear canal (figure 2). The distance from this zero degree starting point to the basal tip of the body donor's organ of Corti is 2.7mm (mean length of the hook region 2.55mm).

This method is a 3-dimensional coordinate system making use of co-registration of patient CT data and a template of one single body donor ear. The zero degree angle refers to the anterior margin of the round window. The software package used is already extended to include a recording point at the centre of the round window. This additional point provides an individual correction factor to the consensus coordinate system.

CView[®]

Marsh and coworkers [23] introduced the Cochlear View. On these 2-dimensional images a grid system is applied to allow for angular measurements of insertion depth. The technique was developed by Cohen et al. [22] in order to extract angular position information from digitized X-ray images and to express these angles, approximately relative to the basal end of the organ of Corti. This method was applicable to cochleae of different sizes but assumed an electrode trajectory characteristic of the “straight” Banded Nucleus array. The method was subsequently modified and extended by Cohen et al. [32] in order to become independent of the electrode array and to estimate the distances of electrode bands from the modiolus. These methods as described briefly in Xu et al. [25] and Cohen et al. [22] use a reference line drawn through the apex of the superior semicircular canal (SSCC) and the center of the vestibule, passing close to the round window. Mean spirals of the inner and outer walls of the scala tympani (obtained from Silastic[®] molds of temporal bones) and of the outer wall of the otic capsule (processed from digitized serial sections of a cochlea) were calculated. The latter can be visualized on both preoperative and postoperative X-rays. By scaling the registered spirals and adjusting X and Y positions, a best fit of the otic capsule outer wall spiral to the image is obtained in a software package called CView[®]. Therefore, the spiral template reflects the variation of cochlear size. A line is drawn from the estimated spiral center point perpendicular to the reference line through the SSCC. The intersection of the two lines defines the “geometric” zero degree angle. Superposition of Kawano’s data [12] after scaling gave an estimation of the angular position of the basal end of the OC. Based upon these measurements, the zero angle for the Cochlear View construction was corrected by 10° to approximate the basal end of the OC [32] (figure 3 A-C).

This allowed for direct application of the Bredberg and Greenwood data. Two additional angles were obtained (relative to geometric zero), corresponding to the mean entry points for Banded Nucleus arrays implanted through the round window (13.5°) and through a cochleostomy just apical of the round window (23.8°). The angle representing the “apical” side of the round window would, therefore, be less than 23.8°.

Based on recent data from Skinner et al., Cohen (personal communication) considers that the angular correction relating the “geometric zero” to the basal end of the organ of Corti, in CView, should probably be nearer to five degrees than to ten degrees. However, further data would be required to confirm the appropriateness of such a change.

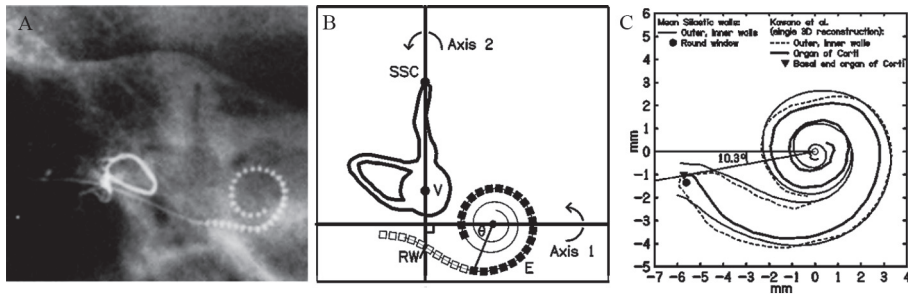


Figure 3. CView[®]: (A) Cochlear View image, (B) schematic drawing of a cochlear coordinate system based upon anatomical landmarks. A reference line is drawn through the superior semicircular canal (SSC) and the centre of the vestibule (V). Based upon Silastic[®] molds of the scala tympani, inner and outer wall spiral functions were calculated. In addition, from analysis of a temporal bone, a third registered spiral was produced to represent the outer wall of the otic capsule (not shown). This spiral is scaled and shifted on the x-y plane in order to achieve a best fit to the image of the bony outer wall visible on the X-ray, thus determining the center of the cochlear spiral. A second reference line is drawn from the center point, perpendicular to the first reference line, thus defining a “geometric” zero angle. Kawano’s data on the length of the Organ of Corti (OC), superimposed on the figure, enabled estimation of the position of the basal end of the OC (C). This point lay at approximately 10° relative to the “geometric” zero, and was used as the origin for calculation of percentage length along the organ of Corti and, thus, characteristic frequency via the Greenwood equation. (Note, in (B), that although the array tends to penetrate the outer wall of scala tympani, it remains inside the bony outer wall.)

CView[®] uses a 2-dimensional coordinate system in the Cochlear View, providing angular measurements approximately from the tip of the OC. Its plane of rotation forms the basis for the universal cochlear framework. From X-ray data it is not possible to visualize the round window directly. Comparison to outcomes of insertion angles measured in 13 patients with this method and with the previously described method

showed highly correlated outcomes, reflecting the common conceptual framework of these methods. [27]

Postoperative 2D method (Geneva)

Using the above described Cochlear View Kós, Boëx et al. [26] performed both linear and angular measurements of insertion depth. A geometric zero angle was used as a point of reference and the center of the spiral was defined in the first turn (360°) as well as in the second turn (720°) (figure 4). The geometric zero used by this group was the point at which the electrode array, inserted through the round window, crossed the reference line between SSC and V (as used in CView). It approximates the center of the round window and differs from the geometric zero used in CView (by approximately 13.5°).

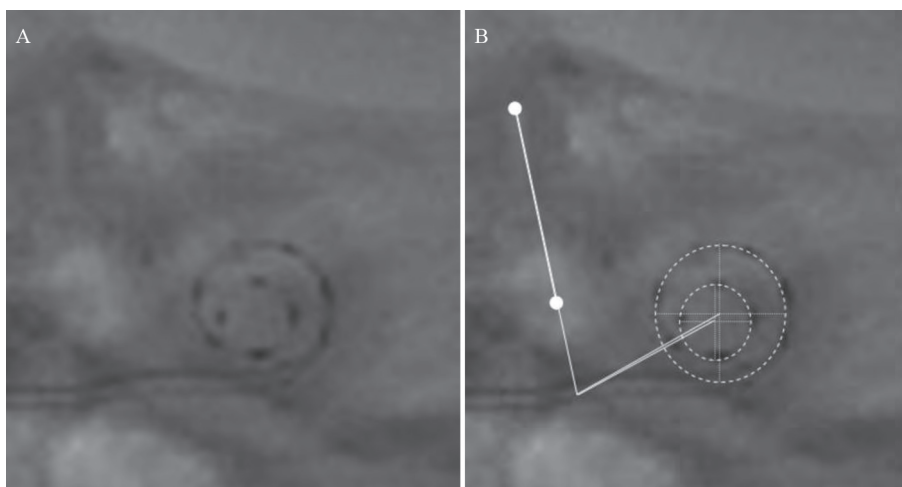


Figure 4. Angular measurements as performed by Boëx et al: a modified Stenvers (Cochlear View) X-ray is performed (**A**) and a geometric zero reference was determined by the point at which the electrode array crossed the SSC/V reference line described by Cohen et al and Xu et al. This corresponded approximately to the round window (and differed from the geometric zero of Cohen et al and Xu et al.). The line going through this point to the center of the first turn of the spiral made by the electrode array, is used as the zero degree reference line for electrodes belonging to the first turn. For electrodes belonging to the second turn of the spiral of the electrode array a line going through the estimated site of the round window to the center of the second turn of the spiral made by the electrode array, is determined as the 720° line (**B**).

In this modification of the previous method, the authors attempt to include a z-axis through the center of the modiolus. Consequently, misalignment due to suboptimal positioning of the patient was approximately corrected for. In order to compare results with those obtained with other techniques, an appropriate angular correction factor should be applied.

Histology-based system (UCSF)

Stakhovskaya, Leake and co-workers performed calculations of characteristic frequencies of the OC and SG versus angle of rotation from the round window. [13] In this histopathological study the OC was directly visualized. Surface preparations were obtained of the isolated cochleae through the middle of the modiolus, in a plane oriented as nearly parallel as possible to the radial nerve fibers on each side of the basal turn equal the Cochlear View plane. The zero degree reference point was chosen at 1mm from the basal end of the OC. This point was chosen because the initial portion of the OC curves inferiorly and would project as a continuous zero or close-to-zero degree value and would be difficult to see in imaging studies.

In the histopathological approach the grid system is applied as defined in the consensus and the zero angle is chosen on the directly visualized OC at 1 mm from the basal end of the OC. It is estimated that this approximates the position of the border of the round window adjacent to the vestibule, which can be seen in imaging studies.

CT-based 3D-coordinate system (Leiden)

Verbist et al reported an acquisition protocol for multi detector row tomography allowing for visualization of individual electrode contacts and fine anatomic inner ear structures in the human cochlea in a clinical setting. [24] A multiplanar reconstruction through the basal turn of the cochlea is made, rendering a stack of images in the desired plane of rotation. The z-axis is defined through the center of the modiolus. Since the normal anatomy at the level of the round window can be distorted by surgery (according to the chosen approach for the cochleostomy) the zero angle is chosen at the top of the horizontal semicircular canal (figure 5). Preliminary results in 25 patients show that taking into account a correction of $34.6^\circ \pm 0.8^\circ$ (2 SD) insertion depth measurements can be made in relation to the center of the round window.

This grid system is developed to be applied in a clinical situation where only a postoperative scan might be available. The zero degree angle is chosen outside the cochleostomy region, but the relationship to the round window has been established.

Summary and conclusion

Research on the human cochlear anatomy in relation to tonotopy and cochlear implantation conducted by histologists, surgeons, physicists, audiologists, radiologists and others has prompted the need for a universal cochlear coordinate system to achieve comparable measures between histological, surgical and psychophysical findings. To attain a widely accepted standard, researchers with backgrounds in the various fields of inner ear research as well as representatives of the different manufacturers of cochlear implants (Advanced Bionics Corp, Med-El, Cochlear Corp) were involved in consensus meetings held in Dallas, March 2005 and Asilomar, August 2005.

Over the years several coordinate systems have been introduced. Since they use different landmarks in their definition of coordinates, the outcomes differ and cannot be easily converted to each other. This is partly due to inherent differences in visualization of soft tissue structures within the cochlea between histopathological studies and different imaging techniques. Therefore the consensus panel formulated an objective framework, applicable in all fields and on both preoperative and postoperative cochleae. The basis of the framework is formed by the Cochlear View, which has been used in all discussed coordinate systems. The extension into a 3-dimensional cylindrical system by placing a z-axis through the center of the modiolus with its origin at the helicotrema ensures optimal spatial information. This can be achieved clinically, in cochlear implant patients, with the use of high resolution imaging. With the evermore widespread availability of multislice CT scanners the requested resolution to apply the 3D framework will come in reach of many clinicians in the near future. [33] The 3D-framework may not seem of direct added value to surgeons for intraoperative feedback. However, if applied to pre- and postoperative imaging, it will render anatomic information for operation planning as well as information of the surgical result. By choosing the round window as the zero degree angle of rotation, a reference point visible in all fields and techniques and in close relationship to the end of the OC has been defined. Accurate comparisons between all methods should now become possible, provided that correction angles to the round window are available.

The value of coordinatesystems for preoperative planning and postoperative evaluation of the precise intracochlear positioning of a cochlear implant has been shown in several reports in the literature. Both 2-dimensional [34,35] and 3-dimensional [13,17,36] coordinate systems provide angular insertion depths. This information, used in conjunction with the frequencymap developed by Stakhovskaya et al. [13], provides a basis for more accurate assignment of frequencybands to stimulation sites in fitting individual cochlear implant users. [34]

For assessment of cochlear anatomy and scalar position of cochlear implant electrode contacts 3-dimensional coordinate systems have been applied quite successfully. [17,36,37] The z-coordinate reflects the height of a specific anatomic structure or electrode contact in relation to the plane of the basal turn of the cochlea. It therefore provides information on the risk for or the presence of insertion trauma, which has been reported to be correlated with outcome in terms of word recognition scores. [36,38] Thus a 3-dimensional coordinate system can contribute to assessing surgical technique and to correlating the surgical result to psychophysical findings.

As described above the consensus cochlear coordinate system is merely an extension of the existing 2-dimensional CView[®] method of Xu and Cohen by adding a z-axis, which defines the third dimension. As such it does not differ from and it will provide the same information (insertion depth and scalar position) as described for other 3-dimensional coordinate systems in literature. Its ultimate role however is to serve as a widely agreed upon coordinate system of reference between the numerous, slightly variable approaches by providing the requisite information to allow the use of the center of the round window as a 0 degree reference angle.

References

1. Greenwood DD. A cochlear frequency-position function for several species--29 years later. *J Acoust Soc Am* 1990;87:2592-2605
2. Greenwood DD. Critical bandwidth and consonance in relation to cochlear frequency-position coordinates. *Hear Res* 1991;54:164-208
3. Greenwood D. Critical Bandwidth and Frequency Coordinates of Basilar Membrane. *J Acoust Soc of Am* 1961;33:1344-56
4. Blamey PJ, Dooley GJ, Parisi ES, Clark GM. Pitch comparisons of acoustically and electrically evoked auditory sensations. *Hear Res* 1996;99:139-150
5. Tong YC, Clark GM. Absolute Identification of Electric Pulse Rates and Electrode Positions by Cochlear Implant Patients. *J Acoust Soc Am* 1985;77:1881-1888
6. Collins LM, Zwolan TA, Wakefield GH. Comparison of electrode discrimination, pitch ranking, and pitch scaling data in postlingually deafened adult cochlear implant subjects. *J Acoust Soc Am* 1997;101:440-455
7. Boëx C, Baud L, Cosendai G, Sigrist A, Kos MI, Pelizzone M. Acoustic to electric pitch comparisons in cochlear implant subjects with residual hearing. *J Assoc Res Otolaryngol* 2006;7:110-124
8. Dorman MF, Spahr T, Gifford R, et al. An electric frequency-to-place map for a cochlear implant patient with hearing in the nonimplanted ear. *J Assoc Res Otolaryngol* 2007;8:234-240
9. Briaire JJ, Frijns JH. The consequences of neural degeneration regarding optimal cochlear implant position in scala tympani: a model approach. *Hear Res* 2006;214:17-27
10. Sridhar D, Stakhovskaya O, Leake PA. A frequency-position function for the human cochlear spiral ganglion. *Audiol Neurootol* 2006;11 Suppl 1:16-20
11. Ariyasu L, Galey FR, Hilsinger R, Byl FM. Computer-Generated 3-Dimensional Reconstruction of the Cochlea. *Otolaryngol Head Neck Surg.* 1989;100:87-91
12. Kawano A, Seldon HL, Clark GM. Computer-aided three-dimensional reconstruction in human cochlear maps: Measurement of the lengths of organ of Corti, outer wall, inner wall, and Rosenthal's canal. *Ann Otol Rhinol Laryngol.* 1996;105:701-709
13. Stakhovskaya O, Sridhar D, Bonham BH, Leake PA. Frequency map for the human cochlear spiral ganglion: implications for cochlear implants. *J Assoc Res Otolaryngol* 2007;8:220-233
14. Bredberg G. Cellular pattern and nerve supply of the human organ of Corti. *Acta Otolaryngol* 1968;Suppl 236: 1-135
15. Wright A, Davis A, Bredberg G, Ulehlova L, Spencer H. Hair cell distributions in the normal human cochlea. *Acta Otolaryngol Suppl* 1987;444:1-48
16. Ketten DR, Vannier MW, Skinner MW, Gates GA, Wang G, Neely JG. In vivo measures of cochlear length and insertion depth of nucleus cochlear implant electrode arrays. *Ann Otol Rhinol Laryngol Suppl.* 1998 ;175:1-16
17. Skinner MW, Ketten DR, Holden LK, et al. CT-derived estimation of cochlear morphology and electrode array position in relation to word recognition in nucleus-22 recipients. *JARO* 2002;3:332-350

18. Ulehlova L, Voldrich L, Janisch R. Correlative study of sensory cell density and cochlear length in humans. *Hear Res* 1987; 28: 149-151
19. Hardy M. The length of the organ of Corti in man. *Am J Anat* 1968;62:291-311
20. Sato H, Sando I, Takahashi H. Sexual Dimorphism and Development of the Human Cochlea - Computer 3-D Measurement. *Acta Oto-Laryngologica* 1991;111:1037-1040
21. Escude B, James C, Deguine O, Cochard N, Eter E, Fraysse B. The size of the cochlea and predictions of insertion depth angles for cochlear implant electrodes. *Audiol Neurootol* 2006;11 Suppl 1:27-33
22. Cohen LT, Xu J, Xu SA, Clark GM. Improved and simplified methods for specifying positions of the electrode bands of a cochlear implant array. *Am J Otol* 1996;17:859-865
23. Marsh MA, Xu J, Blamey PJ, et al. Radiologic Evaluation of Multichannel Intracochlear Implant Insertion Depth. *Am J Otol* 1993;14:386-391
24. Verbist BM, Frijns JHM, Geleijns J, van Buchem MA. Multisection CT as a valuable tool in the postoperative assessment of cochlear implant patients. *AJNR Am J Neuroradiol* 2005;26:424-429
25. Xu J, Xu SA, Cohen LT, Clark GM. Cochlear view: Postoperative radiography for cochlear implantation. *Am J Otol* 2000;21:49-56
26. Kos MI, Boex C, Sigrist A, Guyot JP, Pelizzone M. Measurements of electrode position inside the cochlea for different cochlear implant systems. *Acta Oto-Laryngol* 2005;125:474-480
27. Skinner MW, Holden TA, Whiting BR, et al. In vivo estimates of the position of advanced bionics electrode arrays in the human cochlea. *Ann Otol Rhinol Laryngol Suppl* 2007;197:2-24
28. Yoo SK, Wang G, Rubinstein JT, Vannier MW. Three-dimensional geometric modeling of the cochlea using helico-spiral approximation. *IEEE Transactions on Biomedical Engineering* 2000;47:1392-1402
29. Skinner MW, Ketten DR, Vannier MW, Gates GA, Yoffie RL, Kalender WA. Determination of the position of nucleus cochlear implant electrodes in the inner ear. *Am J Otol* 1994; 15:644-651
30. Wang G, Vannier MW, Skinner MW, Kalender WA, Polacin A, Ketten DR. Unwrapping Cochlear Implants by spiral CT. *IEEE Trans Biomed Eng* 1996;43:891-900
31. Whiting BR, Holden TA, Brunnsden BS, Finley CC, Skinner MW. Use of Computed Tomography Scans for Cochlear Implants. *J Digit Imaging* 2008 Sep;21(3):323-8
32. Cohen LT, Xu J, Tycocinski M, Saunders E, Raja D, Cowan R. Evaluation of an X-ray analysis method: comparison of electrode position estimates with information from phase contrast X-ray and histology. 5th European Symposium on Paediatric Cochlear Implantation, Antwerp, Belgium 2000.
33. Verbist BM, Joemai RMS, Teeuwisse WM, Veldkamp WJH, Geleijns J, Frijns JHM. Evaluation of 4 multisection CT systems in postoperative imaging of a cochlear implant: A human cadaver and phantom study. *AJNR Am J Neuroradiol* 2008;29:1382-1388
34. Rebscher SJ, Hetherington A, Bonham B, Wardrop P, Whinney D, Leake PA. Considerations for design of future cochlear implant electrode arrays: Electrode array stiffness, size, and depth of insertion. *J Rehab Res Devel* 2008;45:731-747
35. Connor SEJ, Bell DJ, O’Gorman R, Fitzgerald-O’Connor A. CT and MR Imaging Cochlear Distance Measurements May Predict Cochlear Implant Length Required for a 360 degrees Insertion. *AJNR Am J Neuroradiol* 2009;30:1425-1430

36. Finley CC, Holden TA, Holden LK, et al. Role of electrode placement as a contributor to variability in cochlear implant outcomes. *Otol Neurotol* 2008;29:920-928
37. Verbist BM, Ferrarini L, Briaire JJ, et al. Anatomic considerations of cochlear morphology and its implications for insertion trauma in cochlear implant surgery. *Otol Neurotol* 2009;30:471-477
38. Aschendorff A, Kromeier J, Klenzner T, Laszig R. Quality control after insertion of the nucleus contour and contour advance electrode in adults. *Ear Hear* 2007;28:75S-79S

6

Cochlear Coordinates in Regard to Cochlear Implantation: a Clinically Individually Applicable 3-dimensional CT-based Method

BM Verbist, RMS Joemai, JJ Briaire,
WM Teeuwisse, WJH Veldkamp, JHM Frijns

Otology & Neurotology, in press

Abstract

Setting: Cochlear implant/tertiary referral center.

Subjects: 25 patients implanted with an Advanced Bionics HiRes90K HiFocus1J CI.

Study Design/main outcome measures: A 3-dimensional cylindrical coordinate system is introduced using the basal turn of the cochlea as the x,y-plane and the center of the modiolus as the z-axis. The 0°-angle is defined by the most lateral point of the horizontal semicircular canal. It is applied to both pre-and postoperative CTs in 25 patients. The angular position of the round window (RW) is examined. Interobserver reproducibility is tested by localization of all electrode contacts within the coordinate system. To observe realignment over time electrode coordinates in postoperative images were projected on preoperative images. Additionally, comparison to existing imaging-related coordinate systems was made.

Results: The angular position of the center of the round window is $34.6^{\circ} \pm 0.4^{\circ}$ (SD) with an intraclass coefficient (ICC) of 1.00. The ICC for interobserver reproducibility of the 16 electrode contacts ranged from 0.74-1 for the rotational angle (φ) and 0.77-1 for the distance to the modiolus (ρ). In 21 out of 25 patients a perfect match or minimal displacement of up to 3 electrode contacts was seen. Comparison to existing systems showed good correlation.

Conclusion: A 3 dimensional cochlear coordinate system easily applicable in clinical patients is described, which fulfills the requirements set by an international consensus.

Introduction

Imaging of cochlear implants (CI) has become more demanding over the past decades. Whereas in the early years imaging served for confirmation of the intracochlear position and integrity of an implant, nowadays far more detailed information is sought for. The results of CI regarding speech perception vary considerably between implantees. Parameters known to influence the performance are duration of deafness, preoperative speech recognition abilities, age at implantation, electrode design and speech encoding strategies. [1-4] A recent report also indicated that electrode location and insertion depth are of major influence on the performance. [5] These have been studied intensely by amongst others histopathologists, physicist and ENT surgeons. To better understand the role of the positioning of electrode contacts along the organ of Corti it now becomes important to correlate histopathological *ex vivo* studies [6], computer simulations [7] and animal studies [8] with clinical imaging studies. The imaging parameters of importance are insertion depth and electrode contact – to –modiolar distance. Recently also the amount of cochlear trauma induced by electrode insertion has become an area of interest. To evaluate this high resolution volume imaging is required to obtain as much anatomical detail as possible as well as a cochlear coordinate system that can be applied in all clinical patients and renders data comparable to results in all fields of research involved. Such a coordinate system has to fulfill several requisites, which were formulated in 2 consensus meetings held by researchers with a background in the various fields of inner ear research as well as representatives of the different manufacturers of cochlear implants. [9,10] The panel agreed upon a 3-dimensional cylindrical coordinate system with its x,y-plane along the basal turn and the z-axis through the center of the modiolus. The 0-degree reference point should be related to the round window. Additionally the coordinate system must be applicable on both implanted and non implanted ears. In such a system all spatial information of the cochlea and the implant are present and the insertion depth of an implant can be expressed in angular measurements. Thus it can be used to examine prediction of optimal insertion depth thereby providing direct information to the surgeon. Post-operatively it provides a mean for assessment of cochlear trauma due to insertion and optimization of implant fitting based on its position within the cochlea. The first imaging related coordinate system has been described by Xu et al. [11] They applied a 2-dimensional coordinate system to conventional radiographs (cochlear view). Skinner et al. [12] developed a method for

application of a 3-dimensional coordinate system to CT images making use of fusion with very high resolution images of a template temporal bone.

Our goal was to develop an easily applicable 3-dimensional coordinate system for the assessment of the cochlea in individual clinical patients without the use of a predefined template and examine whether it fulfills the requirements set by the consensus panel. The coordinate system's applicability and the inter -and intraobserver reproducibility will be examined on multi detector row computed tomography (MDCT) images of 25 patients. The results are compared to coordinate systems described by Cohen and Xu and Skinner and coworkers. [11-14]

Materials and Methods.

Patients

First 25 patients were selected in alphabetical order from the cochlear implant database at our institution within the period October 2006 to June 2007. All patients were treated for severe sensorineural hearing loss (SNHL) or deafness with cochlear implantation (17 on the right side, 8 on the left). The age ranged from 1 year and 7 months to 83 years. Duration of deafness before implantation ranged from 1 to 58 years. One patient had a congenital ear malformation (incomplete partitioning and enlarged vestibular aqueduct. The etiologies of deafness included meningitis (n=3), nonsyndromic familial (n=8), nonsyndromic congenital (n=4), syndromic congenital (n=1), congenital infections (rubella and lues) (n=2), (acoustic) trauma (n=1), otosclerosis (n=1), progressive SNHL (n=2), Meniere disease (n=2) and of unknown origin (n=1). Subjects received a HiRes90K HiFocus 1J cochlear implant (Advanced Bionics, Sylmar, California, USA).

Image acquisition and reconstruction

All patients (n=25) underwent preoperative computer tomography (CT) scanning as part of the standard work up for cochlear implantation. Postoperative scans were obtained 1 day after the implantation of a HiRes90K HiFocus 1J electrode array. This electrode array consists of 16 electrode contacts, with contact 1 at the apex and contact 16 at the base of the electrode. The scans were performed on a multi detector row CT (Aquilion 4 or 16, Toshiba Medical Systems, Otawara, Japan) using the following parameters for both scanners: 4 X 0.5mm section thickness; 0.5 seconds rotation time; 0.75 pitch

factor; 120 kV tube voltage; 150mA tube current; and a 240mm scan field-of-view (FOV) as described by Verbist et al. [15] Images with a nominal thickness of 0.5mm were reconstructed by using a 0.3mm reconstruction increment, 90mm reconstruction FOV, 512 X 512 matrix and a high resolution reconstruction kernel. Multiplanar reconstructions (MPR) were obtained in preoperative scans and in postoperative scans (n=25). The MPRs were defined by a line parallel through the center of the modiolus and an orthogonal line parallel to the basal turn of the cochlea; this emulates the cochlear view as described by Xu and Cohen. [11,13,14] The MPRs were stored as consecutive slices with a slice thickness of 0.5mm. On these images the 3-dimensional cylindrical coordinate system was applied.

3D coordinate system and its implementation in computed tomography

Using an in-house developed MATLAB-software (MATLAB R2006a, MathWorks, Novi, Mich) program the 3-dimensional cylindrical coordinate system was applied to the MPRs of the cochleovestibular system. To define the coordinate system the most lateral point of the horizontal semicircular canal is registered by the user, this serves as a landmark for the 0° angle. (figure 1) By scrolling through the images the slice on which the modiolus is visualized the last time is identified and used to set the origin of the z-axis (at the level of the helicotrema, as agreed in the consensus). Positions indicated by the user within the cylindrical coordinate system are expressed in angular position (φ) and the radial distance (ρ).

Relationship between the organ of Corti and the chosen 0°-angle in the 3D coordinate system

The relationship between the defined 0°- baseline and the most basal part of the organ of Corti was examined. Since the organ of Corti itself cannot be directly visualized, the round window – known to have a fairly stable relationship to the end of the organ of Corti [16] – was used as a point of reference. The anterior and posterior lip of the round window were marked on all preoperative scans (n=25) by 4 observers and their position within the coordinate system was stored by the program. The values for the center of the round window were calculated ($\text{angle}_{\text{posterior lip}} + \text{angle}_{\text{anterior lip}}/2$).

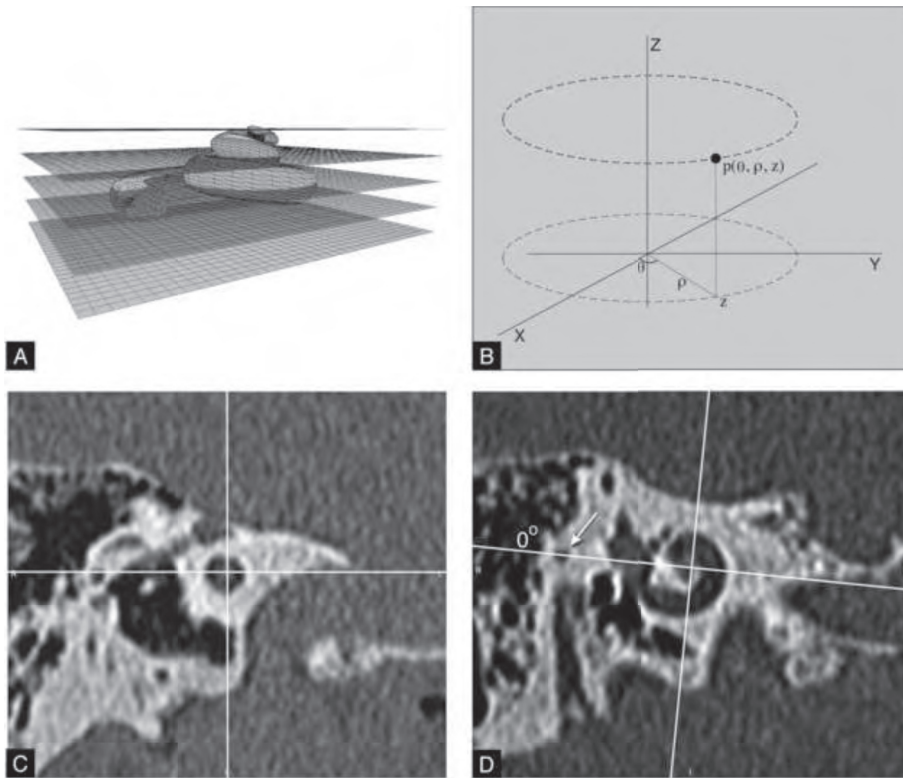


Figure 1. CT-based 3D cochlear coordinate system: a stack of reformatted CT images is made along the plane of the cochlear basal turn as shown schematically in (A). A 3D cylindrical coordinate system (B) can then be applied: the z-axis is placed through the modiolus and the 0° -angle is defined by the most lateral point of the horizontal SCC (arrow) (C, D).

Reproducibility of the CT-based 3D-coordinate system (interobserver)

To test the inter observer reproducibility of the coordinate system 4 observers applied the 3-dimensional coordinate system on all postoperative scans. Next the center of the 16 electrode contacts was marked and their position within the coordinate system was stored. The mean values and standard deviations were calculated over all observers.

Reproducibility of CT-based 3D-coordinate system over time (realignment)

In order to test the realignment of the newly applied coordinate system electrodes registered in the postoperative images were projected in the preoperative images. First the 3D coordinate system was applied to the postoperative scans and all 16 contacts

were marked. The slice on which the contact is optimally visualized was chosen and the center of the contact was indicated with a circle. Next the coordinate system was applied to the preoperative scan and the colour-coded markers were inserted. (figure 2) The resulting images were graded from I to III: a) grade I if the center of the contacts projected in the cochlear lumen, b) grade II if the center of 1 or more contacts project on the border of the cochlear lumen and c) grade III in case the center of 1 of more contacts project outside the cochlear lumen onto the otic capsule.

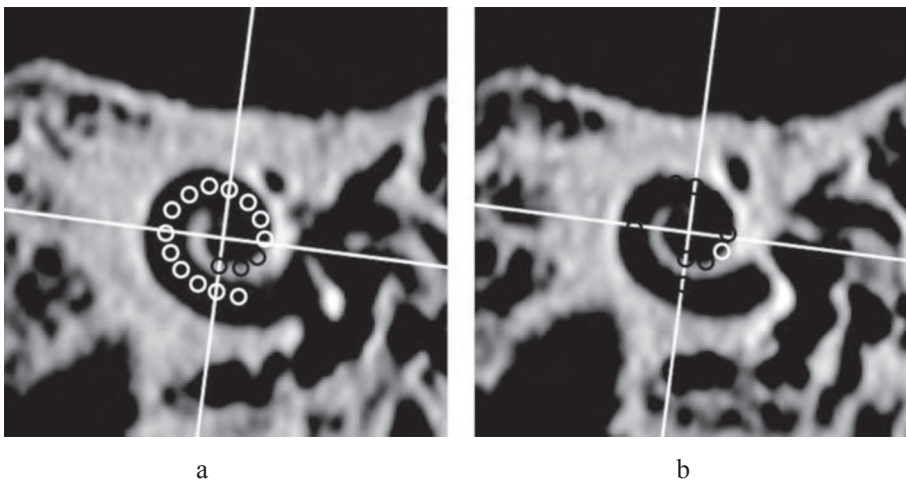


Figure 2: realignment of the CT-based 3D cochlear coordinate system: markers indicating the position of 16 electrode contacts were obtained from postoperative images and inserted into preoperative CT images (white: contacts marked in the current image, black: contacts marked on another image). In (a) all white markers project in the cochlear lumen (grade 1), corresponding to a perfect fit of the coordinatessystem applied on pre-and postoperative images. In (b) the center of the white marker projects outside the cochlear lumen (grade 3).

Statistical analysis

Interobserver variability was evaluated by two-way ANOVA analysis with random effects. Both the observers and the patients were modeled as random variable. Accordingly, the intraclass correlation coefficient (ICC) was calculated. The ICC expresses the variance by patients (due to variation between patients) as a proportion of the total variance (i.e. the sum of the patients' variance and the observers' variance). The ICC is a measure

of repeatability. Ideally, the ICC coefficient is close to 1 meaning that the variation by observers is low compared to the variation between patients.

Correlation to coordinate system described by Xu and Cohen

To investigate the relationship between the described method and existing methods the coordinate system as used in cochlear view [14] was applied to the preoperative CT datasets. To obtain an image comparable to x-ray images on which this 2-dimensional coordinate system is applied, a thick averaged MPR including the total cochleovestibular system was reconstructed. To account for variations in cochlear size mean spirals of the inner and outer walls of the scala tympani (obtained from Silastic[®] molds of temporal bones) and of the outer wall of the otic capsule (processed from digitized serial sections of a cochlea) are fitted to the cochlea in CView[®]. These mean spiral wall functions were made available by L Cohen and incorporated in newly developed software in MATLAB. The registered spiral of the outer wall of the otic capsule was scaled and rotated to obtain a best fit on the thick averaged MPRs of preoperative scans of each patient. The center of this spiral determines the z-axis. Next the apex of the superior semicircular canal and the estimated center of the vestibule were marked to apply the x,y-axes. (figure 3) Also the new defined cylindrical coordinate system was applied on the thick averaged MPR placing the x-axis through the superior SCC. Both the translation of the z-axis and the angular distance between the baseline 0°-angles of both coordinate systems were calculated. Measurements were performed by 3 observers.

Correlation to coordinate system described by Skinner et al

In order to compare the position of our 3D coordinate system to the method described by Skinner et al. [12] our CT datasets were analyzed by T Holden. The software package used, included a recording point at the center of the round window. In this way the difference between the 0° degree starting point used by Skinner et al. - defined as a line joining the midmodiolar axis in the middle of the cochlear canal entry – and the center of the round window were registered. Also the position of electrode contacts 1 and 16 were marked and stored. Using the φ of the round window in both coordinate systems a correction factor was determined for each individual patient. This correction factor was applied on the electrode contacts to achieve normalized electrode contact positions which enable comparisons of results in both coordinate systems. The difference between the two systems was determined for electrode contacts 1 and 16.

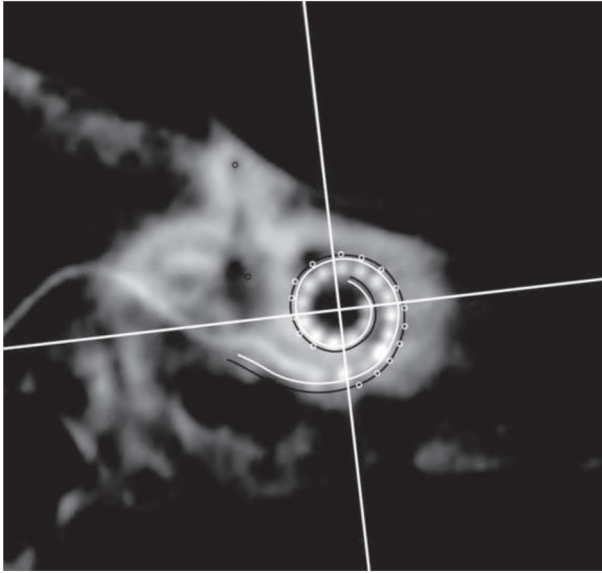


Figure 3. Application of the coordinate system described by Cohen, Xu and coworkers on our datasets: mean spiral cochlear wall functions were applied to a thick averaged MPR of a preoperative CT-dataset showing anatomical landmarks such as the superior SCC and the vestibule in 1 image. The center of outer wall spiral determines the z-axis. A line drawn through the superior SCC and vestibule determines the x,y-axes.

Results

Relationship between the round window and the chosen 0° -angle in the 3D cylindrical coordinate system

Figure 4a shows the mean rotational angle from the horizontal SCC to the calculated center point of the round window per observer. To evaluate the inter rater agreement two-way ANOVA analysis was used and a perfect agreement (ICC of 1.00) was found. The mean rotational angle (\pm -SD) was $34.6 \pm 0.4^\circ$ (range 28.3 - 40.7°).

The mean vector length (\pm -SD) from the z-axis to the calculated center of the round window was 5.92 ± 0.09 mm (range 5.29 - 6.52 mm, ICC of 0.72) (figure 4b).

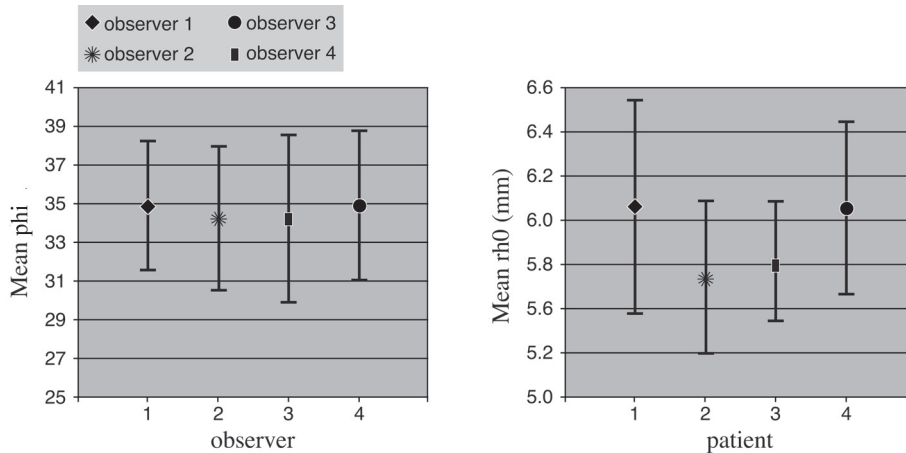


Figure 4. Mean angulation (a) and vector length (b) of the calculated center point of the round window for 4 observers. Error bars indicate the standard deviation.

Reproducibility of the CT-based 3D-coordinate system

Using two-way ANOVA analysis the ICC for each of the 16 electrode contacts localized by the 4 observers was calculated. The results are graphically shown in figure 5 a, b. ICC values for ϕ range from 0.74 (ϕ of contact 16) to 1 and the ICC for ρ ranges from 0.77 to 1.

Reproducibility of the CT-based 3D-coordinate system over time (realignment)

On postoperative scans all contacts showed an intracochlear position. After fusion of the electrode position and the preoperative scans 12 out of 25 patients showed a perfect match of preoperative and postoperative images (grade 1). In 9 patients minimal partial projection of 1 to 3 contacts outside the cochlear lumen were seen (grade 2). Almost all of those contacts were located at the apex or in the second half of the basal turn of the cochlea. Four patients were graded stage III since the center of 1 or more contacts projected outside the lumen. In 3 cases this concerned the most apical electrode contact and in one case contact 8.

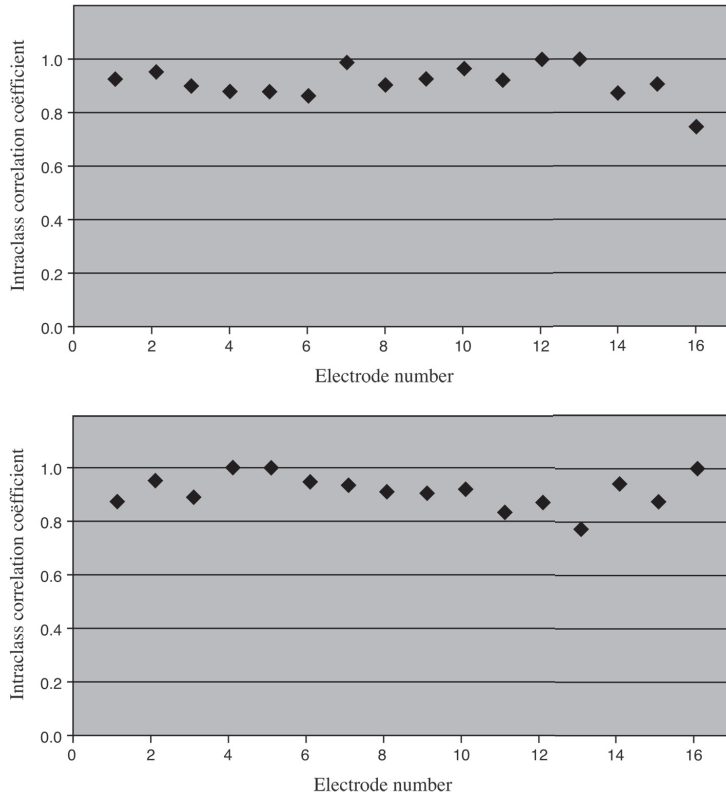


Figure 5. Reproducibility of the CT-based 3D-coordinate system: the ICC for φ (a) and ρ (b) of 16 electrode contacts localized by 4 observers.

Correlation to coordinate system described by Xu and Cohen

A systematic difference with minimal spreading between the two methods was found. Measurements obtained by 3 observers revealed a mean difference in orientation of $23.3^\circ \pm 2.3^\circ$. The mean difference in translation was $0.38\text{mm} \pm 0.14\text{mm}$ (SD).

Correlation to coordinate system described by Skinner et al

The mean difference (\pm SD) between the position of contact 1 and contact 16 measured by the 2 methods on the same patient data was $-3.29^\circ \pm 11.9$ and $3.96^\circ \pm 6.9$ SD, respectively.

Discussion

The cochlea is a complex structure with interindividual differences in size and form. Precise individualized assessment of its morphology has become of utmost importance for research applications and clinical patient care in regard to cochlear implantation. If this information can be obtained preoperatively the choice of an implant as well as the surgical approach and insertion depth could be tailored to the patients needs. Postoperative precise documentation of the location of an implant in relation to the 3-dimensional cochlear anatomical structures would be helpful to evaluate for insertion trauma to the cochlea and to optimize the function of the implant. In this study a 3-dimensional CT-based coordinate system which is easily applicable in daily clinical practice is tested and validated in comparison with existing imaging-based cochlear coordinate systems.

The coordinate system is linked to CT images. Computed tomography enables to image a volume and thus to add the third dimension into imaging studies. Moreover computed tomography provides detailed direct visualization of the cochlear anatomy. Thus, the anatomical landmarks to define the coordinate system can be discerned. Provided (near) – isotropic imaging is done, multiplanar reconstructions can be performed without loss of image quality. In this way the x, y – axes are placed in the plane of the basal turn of the cochlea emulating the cochlear view described by Marsh and Xu. [11,17] Since the CT-derived cochlear view is the result of post processing, malpositioning of the patient can be corrected for and the images can be reformatted until the desired result is obtained. The third dimension is added by a z-axis placed through the center of the modiolus at its tightest point in the apical 1.5 turns of the cochlea. In this 3-dimensional cylindrical coordinate system all spatial information is represented. The fact that the coordinates are individually applied without the use of any template ensures that eventual variations in the direction of the z-axis are taken into account. For indeed, it has been shown in a micro-CT study that the elevation (z-coordinate) of the basilar membrane along the cochlear duct has a non-monotonous path and varies between ears. [18]

The 0-degree reference angle was determined at the most lateral point of the horizontal semicircular canal. In this, the coordinate system differs from others reported in literature. [12,14,19] Ideally the 0°-baseline of the x-axis should be chosen at the end of the basilar membrane (BM). In clinical imaging however, the basilar membrane cannot

be visualized directly. The round window, known to have a close relationship to the end of the basilar membrane, could serve as a nearby anatomical landmark. Although the round window can be clearly identified on CT-images, some problems arise in clinical situations where only a postoperative scan is available. The normal anatomy can be distorted according to the surgical approach of the cochleostomy. Whereas in most cases the cochleostomy is performed anteriorly to the round window, some surgeons prefer to remove the anterior lip of the round window as well. For a-traumatic insertion a direct round window approach is favored. Therefore a well-defined anatomical structure with a close relationship to, but outside the cochlea was chosen: the most lateral point of the horizontal SCC. In this way the coordinate system becomes independent of surgical approach. Moreover, this part of the semicircular canal runs approximately perpendicular to the plane of the reconstructed axial oblique image. The position of the 0° – landmark will therefore only be minimally affected by the chosen slice level on which it is marked. Our data show an angular distance of this landmark to the center of the round window of $34.6 \pm 0.4^\circ$ (SD) with an excellent interobserver agreement (ICC 1.00). A possible drawback of this approach is that it might be difficult to be applied in severe cases of ossifying labyrinthitis with total obliteration of the vestibule and semicircular canals. However in our experience these cases are rarely good candidates for implantation of a single array cochlear implant. Also in patients with severe congenital inner ear malformations the anatomical landmarks will be obscured or absent. In such cases neither of the image based coordinate systems, referring to the vestibular system, will render reliable data. The standard deviation of the mean vector length to the round window (0.09 mm) corresponds to about 2 pixels. Given the the total size of the round window this seems within clinically acceptable limits (figure 6).

To be eligible as a cochlear coordinate system the reproducibility and realignment of a grid system also has to be solid. The interobserver reproducibility showed good to excellent intra class coefficients. To establish the reproducibility of the CT-based method in one individual over time, inpatient comparisons were made by matching preoperative and postoperative images. Our results show a perfect match or minimal displacement of up to 3 electrode contacts in 21 out of 25 patients. All contact centers overlapping the lateral wall of the cochlea are located at the apical side of the electrode. A possible explanation is that minimal overlay along the lateral wall might be the result of volume averaging. Additionally, the size of the cochlear lumen decreases gradually. Using a slab thickness of 0.5mm in the MPRs, a slight shift in the fusion of pre -and

postoperative images may result in a mismatch at the level of the most apical electrode contact.

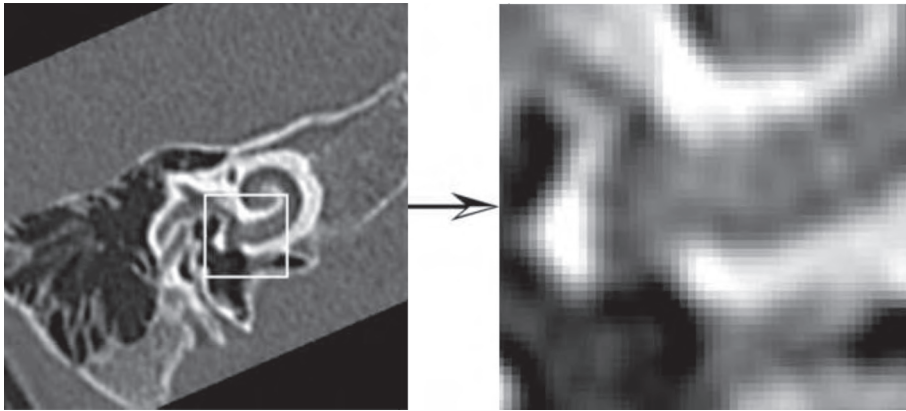


Figure 6. A magnification of a CT image at the level of the round window illustrates the relation between the pixelsize and the size of the round window.

Above mentioned results show that reliable and reproducible measurements of insertion depth and electrode location can be made. For patient-specific preoperative planning estimations of optimal (angular) insertion depth can be made on preoperative CT studies.

To ensure comparability of results obtained with our method and data from previous and forthcoming studies based on other coordinate systems we applied landmarks as described in Cview[®] to our data and had run them through the softwarepackage described by Skinner and coworkers. In the Cview[®] method the 0° rotation angle refers to the basilar membrane. The mean rotation between the 2 systems is $23.3^\circ \pm 2.3^\circ$. This is in line with the expected result based on the reported relationship between the round window and the BM of 10.3° by Cohen and the angular distance of $34.6^\circ \pm 0.4$ between the most lateral point of the horizontal SCC and the round window. The mean difference in translation between the 2 methods is beyond the maximal resolution of the scanner.

In comparison to the method described by Skinner et al mean contact positions differed $-3.29^\circ \pm 11.9^\circ$ SD for contact 1 and $3.96^\circ \pm 6.9^\circ$ SD for contact 16. The wider standard deviation at the apex might result from slight differences in the position of

the z-axis. Differences due to this will become more pronounced at deeper insertion angles where the distance of the electrode contacts to the modiolus (ρ) becomes smaller. Whereas the definition of the z-axis is based on 1 template in the method described by Skinner et al, the CT-based 3D-coordinate system uses individually defined z-axes. Keeping in mind the inter-individual variations of cochlear form and size this might be the underlying cause for this observation.

In this study an in-house developed custom made application in MATLAB was used for automatization of measurements. However, the presented CT-based coordinate system is easily applicable in daily clinical practice. In a recent study it has been shown that multislice CT scanners of major CT scanner manufacturers meet the technical requirements to visualize cochlear implants. The visualization of individual electrode contacts depends on scanner software (available range of gray values (Hounsfield units)) and the inter-contact distance. [20] Viewing stations feature oblique multiplanar reconstruction possibilities. Once the “cochlear view” reconstruction is made the most lateral point of the horizontal semicircular canal is looked for by scrolling through the volume of images. From this point angular measurements can be made and good estimates of optimal (on preoperative images) or achieved (on postoperative images) insertion depth can be obtained.

Conclusion

A 3-dimensional cochlear coordinate system easily applicable on both pre- and postoperative images of commercially available MSCT scanners without the need of cochlear templates and not influenced by postoperative round window distortion is presented. This coordinate system fulfills the requirements set by an international consensus. Taking into account a correction factor of $34.6^\circ \pm 0.4^\circ$ (SD) to the center of the round window, comparison to existing imaging based coordinate systems is possible.

Acknowledgment

We thank Laurie Cohen and Tim Holden for their advice and for making comparison to their respective coordinate systems possible. We also thank Tessa de Jager for her help in analyzing the data.

Reference List

1. Naito Y, Hirano S, Honjo I, et al. Sound-induced activation of auditory cortices in cochlear implant users with post- and prelingual deafness demonstrated by positron emission tomography. *Acta Oto-Laryngol* 1997;117:490-496
2. Nishimura H, Hashikawa K, Doi K, et al. Sign language 'heard' in the auditory cortex. *Nature* 1999;397:116
3. Gomma NA, Rubinstein JT, Lowder MW, Tyler RS, Gantz BJ. Residual speech perception and cochlear implant performance in postlingually deafened adults. *Ear Hear* 2003;24:539-544
4. Rubinstein JT, Parkinson WS, Tyler RS, Gantz BJ. Residual speech recognition and cochlear implant performance: effects of implantation criteria. *Am J Otol* 1999;20:445-452
5. Finley CC, Holden TA, Holden LK, et al. Role of electrode placement as a contributor to variability in cochlear implant outcomes. *Otol Neurotol* 2008;29:920-928
6. Stakhovskaya O, Sridhar D, Bonham BH, Leake PA. Frequency map for the human cochlear spiral ganglion: implications for cochlear implants. *J Assoc Res Otolaryngol* 2007;8:220-233
7. Briaire JJ, Frijns JH. The consequences of neural degeneration regarding optimal cochlear implant position in scala tympani: a model approach. *Hear Res* 2006;214:17-27
8. Shepherd RK, Hatsushika S, Clark GM. Electrical-Stimulation of the Auditory-Nerve - the Effect of Electrode Position on Neural Excitation. *Hear Res* 1993;66:108-120
9. Verbist BM, Skinner MW, Cohen LT, et al. Consensus panel on a cochlear coordinate system applicable in histological, physiological and radiological studies of the human cochlea. *Otology & Neurotology*, in press
10. Verbist BM, Briaire JJ, Ferarini L, et al. Pre- and postoperative assessment of cochlear implantees by means of multidetector row computed tomography . Conference on implantable auditory prostheses, Lake Tahoe, Ca, July 12-17, 2009.
11. Xu J, Xu SA, Cohen LT, Clark GM. Cochlear view: Postoperative radiography for cochlear implantation. *Am J Otol* 2000;21:49-56
12. Skinner MW, Holden TA, Whiting BR, et al. In vivo estimates of the position of advanced bionics electrode arrays in the human cochlea. *Ann Otol Rhinol Laryngol Suppl* 2007;197:2-24
13. Cohen LT, Xu J, Xu SA, Clark GM. Improved and simplified methods for specifying positions of the electrode bands of a cochlear implant array. *Am J Otol* 1996;17:859-865
14. Cohen LT, Xu J, Tycocinski M, Saunders E, Raja D, Cowan R. Evaluation of an X-ray analysis method: comparison of electrode position estimates with information from phase contrast X-ray and histology. 5th European Symposium on Paediatric Cochlear Implantation, Antwerp, Belgium, June 4-7, 2000.
15. Verbist BM, Frijns JHM, Geleijns J, van Buchem MA. Multisection CT as a valuable tool in the postoperative assessment of cochlear implant patients. *AJNR Am J Neuroradiol* 2005;26:424-429
16. Bredberg G. Cellular pattern and nerve supply of the human organ of Corti. *Acta Otolaryngol* 1968;Suppl 236:1-135

17. Marsh MA, Xu J, Blamey PJ, et al. Radiologic Evaluation of Multichannel Intracochlear Implant Insertion Depth. *Am J Otol* 1993;14:386-391
18. Verbist BM, Ferrarini L, Briaire JJ, et al. Anatomic considerations of cochlear morphology and its implications for insertion trauma in cochlear implant surgery. *Otol Neurotol* 2009;30:471-477
19. Kos MI, Boex C, Sigrist A, Guyot JP, Pelizzone M. Measurements of electrode position inside the cochlea for different cochlear implant systems. *Acta Oto-Laryngol* 2005;125:474-480
20. Verbist BM, Joemai RMS, Teeuwisse WM, Veldkamp WJH, Geleijns J, Frijns JHM. Evaluation of 4 multisection CT systems in postoperative imaging of a cochlear implant: A human cadaver and phantom study. *AJNR Am J Neuroradiol* 2008;29:1382-1388

7

Autonomous Virtual Mobile Robot for 3-dimensional Medical Image Exploration: Application to Micro-CT Cochlear Images

L Ferrarini, BM Verbist, H Olofsen, F Vanpoucke, JHM Frijns, JHC Reiber,
F Admiraal-Behloul

Artificial Intelligence in Medicine 2008; 43: 1-15

Summary

Objective: In this paper, we present an autonomous virtual mobile robot (AVMR) for three-dimensional (3D) exploration of unknown tubular-like structures in 3D images.

Methods and Materials: The trajectory planning for 3D central navigation is achieved by combining two neuro-fuzzy controllers, and is based on 3D sensory information; a Hough transform is used to locally fit a cylinder during the exploration, estimating the local radius of the tube. Nonholonomic constraints are applied to assure a smooth, continuous and unique final path. When applied to 3D medical images, the AVMR operates as a virtual endoscope, directly providing anatomical measurements of the organ. After a thorough validation on challenging synthetic environments, we applied our method to eight micro-CT datasets of cochleae.

Results: Validation on synthetic environments proved the robustness of our method, and highlighted key parameters for the design of the AVMR. When applied to the micro-CT datasets, the AVMR automatically estimated length and radius of the cochleae: results were compared to manual delineations, proving the accuracy of our approach.

Conclusions: The AVMR presents several advantages when used as a virtual endoscope: the nonholomic constraint guarantees a unique and smooth central path, which can be reliably used both for qualitative and quantitative investigation of 3D medical datasets. Results on the micro-CT cochleae are a significant step towards the validation of more clinical computed tomography (CT) studies.

Introduction

The advances in imaging modalities such as magnetic resonance imaging (MRI) and computed tomography (CT) allow us nowadays to investigate the inner human body through high-resolution volumetric data. Non-invasive visualization, analysis, and exploration of inner organs are becoming essential tools both for medical research and daily clinical work. However, the amount of images involved in any comprehensive study is massive: manually browsing and analyzing such datasets is a prohibitive, time-consuming task. Thus, there is a pressing need for (semi-) automatic methods to support physicians in their image analyses.

Regardless of the different approaches one might take, the underlying idea is simple: given a medical dataset, one wants to accurately detect the organ of interest, analyze its structural and/or functional properties, and present the results. Virtual endoscopy has become a standard technique to allow an intuitive and non-invasive exploration of internal tubular structures such as blood vessels, airways, or the colon: in order to give a comprehensive internal view of the organ, the detection of a central path along the tubular structure is often required. In Ref. [1], the authors presented an automated central-path tracker based on minimal paths and distance maps, and applied it to virtual colonoscopy for the detection of colorectal polyps. Virtual bronchoscopy was presented in Ref. [2]. A skeleton was first detected from a segmented bronchial-tree, and subsequently pruned and smoothed. The problem of virtual angioscopy was tackled in Ref. [3]: the authors developed a navigation tool, based on depth-map scene analysis, to explore CT images of blood vessels. Virtual endoscopy of coronary arteries was presented in Ref. [4]: the authors showed the advantages of combining different imaging modalities, and integrate them in a virtual reality system to improve both the quantitative analysis of coronary arteries, and the presentation of the results to the physicians. The main approaches presented in literature for virtual endoscopy have their limitations: approaches based on front-propagation have to make sure that the front does not leak out the lumen of interest while searching for the central line [5]; methods based on skeletonization always require extra steps to prune the skeleton from spurious branches, assure connectivity and smooth the path; finally, highly autonomous branch-following methods, such as the navigation method in [3], are usually computationally expensive, and therefore difficult to apply in daily clinical and research environment, where large amounts of data need to be processed.

For its successful application in the clinic, a virtual endoscopy system requires: (1) a smooth and unique trajectory through the organ, (2) a real-time interaction with the explored environment, and (3) a minimal user-interaction. Moreover, the system should be usable in different applications, and must allow a quantitative analysis of the structure under investigation.

In this manuscript, we present a virtual endoscopy system based on advanced autonomous mobile robot navigation. Mobile robots have been extensively used in several fields in which human beings could not safely operate: exploration of ocean's depths, blasting operations, search for survivors within debris, planet explorations, etc. Even in the medical field, small camera-robots have been designed to provide visual feedback of internal organs [6]. Literature on autonomous mobile robots is copious: the primary task of a mobile robot is to move in its environment avoiding collisions with obstacles. Fuzzy controllers are often used for specific tasks like wall-tracking, goal seeking (i.e. reaching a certain location), central navigation. [7-10] In methods based on map-explorations, the mobile robot continuously updates a map of the environments while moving around: new areas to be explored are chosen depending on the map. [11-13] Methods based on artificial neural networks and reinforcement learning have been proposed, in which the mobile robot is rewarded every time a certain goal is achieved [14]: this approach is particularly useful when the robot has to accomplish multiple-tasks related with each other.

In a previous work, we showed the potential of applying virtual mobile robots for the automated exploration and analysis of medical images. A virtual car-like vehicle was implemented for the fully automatic contour detection of the left ventricle in 2D MR slices of the heart. [15] In this paper, we present a virtual flying mobile robot for autonomous central navigation in three-dimensional (3D) tubular structures in medical images. The novelty of our research lies in merging together two well established fields of research, namely virtual endoscopy and autonomous mobile robots, to provide a completely new framework for medical image exploration. We show how the advantages achieved in the robotic field, like inherent properties of nonholonomic kinematics and trajectory planning, can elegantly overcome some critical issues normally encountered in virtual endoscopy. The robot, equipped with several modules (sensory system, virtual camera, trajectory planner, and radius-estimator) and subject to nonholonomic constraints, always provide a smooth and unique final trajectory. Moreover, the virtual camera provides immediate feedback during the exploration, while the radius-estimation

module allows quantitative analysis of the environment. The trajectory planner is based on our 3D extension of a neuro-fuzzy system previously used for two-dimensional (2D) navigation of real robots. [9]

We apply our solution to a challenging analysis, the investigation of post-mortem micro-CT cochlea dataset, showing how expert's results can be reliably reproduced. The accurate analysis of micro-CT datasets is extremely valuable in the field of cochlear implants, representing a first step towards validation of studies based on clinical CT. The method presented in this manuscript provides a reliable tool for a semi-automatic analysis of micro-CT data. Our current implementation does not deal with multiple branches: thus, the method is most suitable for applications (such as the cochlea) in which no bifurcation is expected: nevertheless, the method can still be applied in clinical datasets presenting branches (such as carotid arteries), when the interest is limited to the analysis of one branch.

The manuscript is organized as follows: in section 2 we provide a description of the virtual mobile robot and its modules; in section 3 several experiments with challenging synthetic environments are presented. Section 4 covers the application of the virtual mobile robot to the micro-CT cochlear datasets. After a thorough discussion, the paper ends with some concluding remarks.

Method

The autonomous virtual mobile robot (AVMR) is an autonomous flying object, fully characterized by its structure, kinematics, and trajectory planner. During the exploration of tubular structures, the AVMR has to keep a central position, provide internal views of the environment, and estimate local radius. The design of the AVMR is modular: a *Structure* module includes the geometrical properties and the sensory system; information retrieved by the sensors are fed into a *Radius Estimation* module, and into a *Trajectory Planner* module: the former is responsible for the local estimation of the structure's radius, while the second provides the desired direction in order to keep the central position and orientation. The desired direction is given as input to a *Kinematics & Feasibility* module (together with the geometrical properties), responsible for the movement of the AVMR. The virtual environments explored by the AVMR are

binary datasets, in which 0s represent empty space, and 1s represent obstacles (walls of corridors, etc.).

Geometrical properties and sensory system

The structure of the AVMR is fully described by its geometrical properties and sensors. Considering a coordinate system fixed on the robot, the AVMR dimensions are defined as: *length* L along the local x vector, *width* W along the local y axis, and *thickness* T along the local z axis. On the front side of the AVMR, a steering vector points to the desired direction: in the local system, this vector is fully described by two angles, f and q , respectively on the xy and xz local planes.

While moving through an environment, the AVMR senses its surrounding via virtual range sensors. Each sensor is characterized by its relative position and direction in the local coordinate system on the AVMR. The sensing is simulated by propagating a line through the environment until an obstacle is found, or a maximum distance is reached (if set): the sensors return distance information from the detected obstacle. The AVMR is equipped with (see figure 1):

- N_f frontal sensors: local position $(L,0,0)$, direction identified by two angles (respectively on the local xy and xz planes);
- N_r right sensors, separated along the local x axis by a distance $d_r = L/N_{rp}$ (N_{rp} equals the number of locations for the sensors). For each location $(k(L/N_{rp}), -(W/2), 0)$, $k = 0.1 \dots (N_{rp} - 1)$, $(180 / \alpha) + 1$ sensors are defined, each identified by one angle on the yz plane; N_l left sensors similarly defined (only, with $W/2$);
- N_t top sensors, separated along the local x axis by a distance $d_t = L/N_{tp}$ (N_{tp} equals the number of locations for the sensors). For each location $(k(L/N_{tp}), 0, (T/2))$, $k = 0.1, \dots (N_{tp} - 1)$, $(180 / \beta) + 1$ sensors are defined, each identified by one angle on the yz plane; N_b bottom sensors similarly defined (only, with $-(T/2)$)

Finally, the AVMR is provided with a virtual camera located on the front side of the robot, and orientated along the AVMR's local x axis. During the exploration the camera provides internal views of the environment, based on 3D rendering.

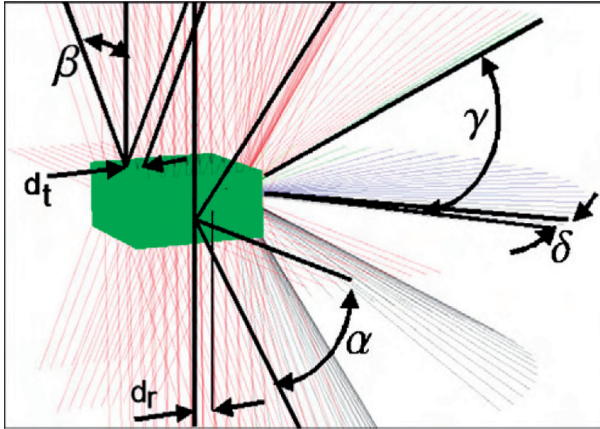


Figure 1. The robot is equipped with frontal and lateral sensors. Right (and left) lateral sensors are separated by an angle α , and located at a distance d_r from each other. Top (and bottom) sensors are characterized by an angle β , and a distance d_t . Frontal sensors are characterized by two angles: γ and δ .

Kinematics & feasibility

At each step during the exploration, the AVMR is given a desired direction for the steering vector. The module responsible for detecting such a direction is the *Trajectory Planner* presented in the next section. As a first step, the direction is tested for feasibility, in order to avoid collisions with obstacles. The angles describing the steering vector are constrained, to assure a certain level of smoothness in the final trajectory: $\phi \in [\phi_{min}, \phi_{max}]$, $\theta \in [\theta_{min}, \theta_{max}]$. During an off-line training session, the AVMR learns the minimum corridors it can move in. The range of 3D directions ($[\phi_{min}, \phi_{max}] \times [\theta_{min}, \theta_{max}]$) is discretized into a set of possible 3D corridors (each having a radius equal to a chosen safety distance): the AVMR uses its range sensors to build up a table of minimum distances for each corridor. Such a table is the prior-knowledge the AVMR uses during its explorations. Given a desired direction, the corresponding corridor is determined: distances retrieved through the sensors are compared with the minimum distances corresponding with the chosen corridor. If the corridor is not suitable, the AVMR looks for the closest feasible corridor to the given direction: if none is found, the AVMR stops its exploration.

Once a feasible desired direction has been found, the AVMR moves simulating a flying vehicle subject to nonholonomic constraints. The AVMR's kinematics is fully

described by its geometry, position and orientation, speed, and desired direction. Nonholonomic constraints are easily formulated in the 2-dimensional (2D) space: given the current position (x^t, y^t) , the speed v , the desired direction (Φ) , and current orientation (η) , next position and orientation are given by:

$$x^{t+1} = x^t + v \cos(\Phi) \cos(\eta) \Delta_t \quad (1)$$

$$y^{t+1} = y^t + v \cos(\Phi) \sin(\eta) \Delta_t \quad (2)$$

$$\eta^{t+1} = \eta^t + v/L \sin(\Phi) \Delta_t \quad (3)$$

In order to apply these formulae in the 3D space, at each step a new plane is identified by the local x axis and the steering vector: on this plane, a new coordinate system is defined, in which equations (1)-(3) can be used. The origin of the new xy plane is located on the origin of the robot's local system, and the new x axis is orientated along the robot's local x axis. In such conditions, η_t always equals 0, and (x^t, y^t) always equals (0,0). The new Φ angle is defined on the new xy plane.

Trajectory planner

The Trajectory Planner module is used to automatically guide the AVMR during its exploration, keeping it in a central position and orientation. The 3D neuro-fuzzy controller (NFC) presented in this work is based on a previous work from Ng and Trivedi: [9] in their work, the authors developed a NFC to guide a real robot while exploring corridors. From the navigation point of view, real robots moving on the floor represent a 2D problem. We extended their approach to guide our AVMR in 3D tubular structures: at each step, the 3D navigation problem is split into two 2D problems: one on the local xy plane, and one on the local xz plane. The AVMR uses its range sensors to estimate its position and orientation (related to the corridor) on each plane: these information are fed into two NFCs which independently provide the desired direction the AVMR should take on the given plane, to adjust its position and orientation (Φ and θ for xy and xz local planes, respectively). Combining the two angles, one obtains the desired steering vector in 3D.

On a given plane (i.e. the xy local one), the AVMR estimates its distance from the walls (D_l and D_r), and its orientation $\Psi(\Psi \in [-\pi/2, \pi/2]$; $\Psi=0$, perfect alignment with the corridor; $\Psi = -\pi/2$, robot going towards the right wall (see figure 2a). Each sensor contributes to the evaluation of either D_l or D_r (see figure 2b). Given the sensor's

orientation in the local system, $s=[s_x, s_y]$, the sensor is associated with D_l if $s_y>0$, and with D_r if $s_y<0$. The corresponding detected distance d is weighted by $\frac{s_y}{|s|}$; D_l and D_r are the weighted averages of the sensors with $s_y>0$ and $s_y<0$ respectively. For the estimation of the orientation Ψ , only the lateral sensors are used ($s_x = 0$), as shown in Figure 2.c. Given D_l and D_r , a relative measure is evaluated:

$$d_{rl} = \frac{D_r - D_l}{D_r + D_l}, \quad d_{rl} \in [-1, 1]; \quad (4)$$

d_{rl} is -1 when the virtual robot is close to the right wall, and 1 when close to the left wall: d_{rl} and Ψ are fed to the NFC. The general scheme is reported in figure 3 (*top*): the input variables are first fuzzyfied via membership functions; the fuzzy variables are then given to a multi-layer feed-forward neural network (rule neural network (RNN)), which maps them on five output membership values; these five values are finally defuzzified by a weighted-average function into one crisp output: the desired angle for the xy local plane. Each component is now described in details.

Input/Output membership functions

The input variable d_{rl} is fuzzyfied via five membership functions: *VeryNegative*, *Negative*, *Zero*, *Positive*, *VeryPositive* (see figure 3a). A high value for the *VeryNegative* (*VeryPositive*) function indicates that the robot is very close to the right (left) wall. The second input variable, Ψ , is fuzzyfied through three membership functions: *Right*, *Center*, *Left* (see figure 3b). Finally, the desired angle for the xy local plane (ϕ) can be strongly oriented to the right (*SR*), oriented to the right (*R*), pointing straight (*PS*), to the left (*L*), or strongly to the left (*SL*): these functions are shown in figure 3c.

RNN

The RNN has 8 input nodes, two hidden layers with 20 and 10 nodes respectively, and 5 output nodes. Each hidden node is modeled with a bias input and a sigmoid function. The aim of this network is to map the 8 fuzzy values associated with d_{rl} and Ψ , into 5 fuzzy values associated with the output variable ϕ . The training of RNN follows the description given in [9]. A set of *parent rules* is used to represent boundary conditions for the controller: aiming at a stable system, it is essential to introduce one rule for the stable condition in which the AVMR is in perfect alignment with the corridor, in the central position, and in which the desired action is to simply keep the current steering angle; the

other rules govern the system in its most unstable conditions. The set of rules (see table 1) is learnt through back-propagation [16]: the AVMR can then interpolate through them while moving through a corridor.

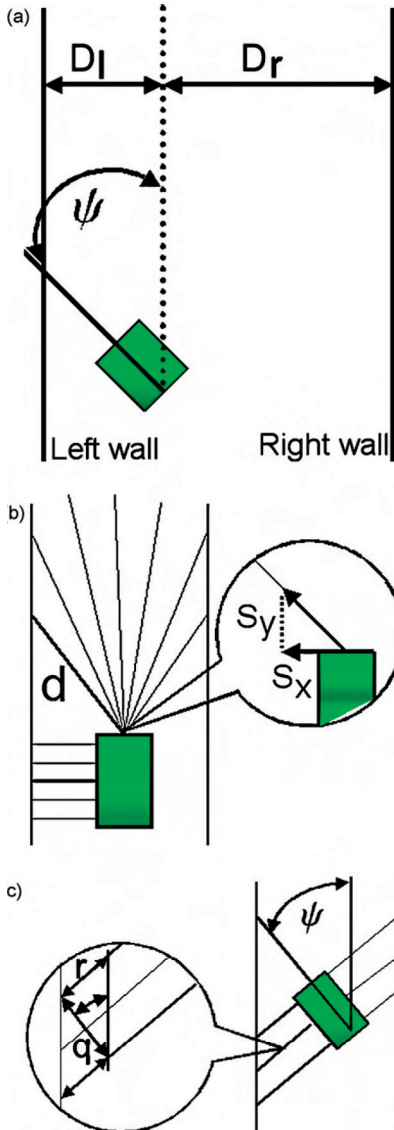


Figure 2. (a) Projecting the sensor information on the local planes (i.e. the local xy plane), the robot evaluates its relative position. (b) To estimate the distance from the left (right) wall, distances d detected by the range sensors are weighted by the local y component of the corresponding sensor (S_x, S_y), and averaged together; (c) considering any pair of lateral sensors, one can easily estimate the orientation $\psi = \text{atan}(r/q)$: the final estimation is the average of the possible pairs.

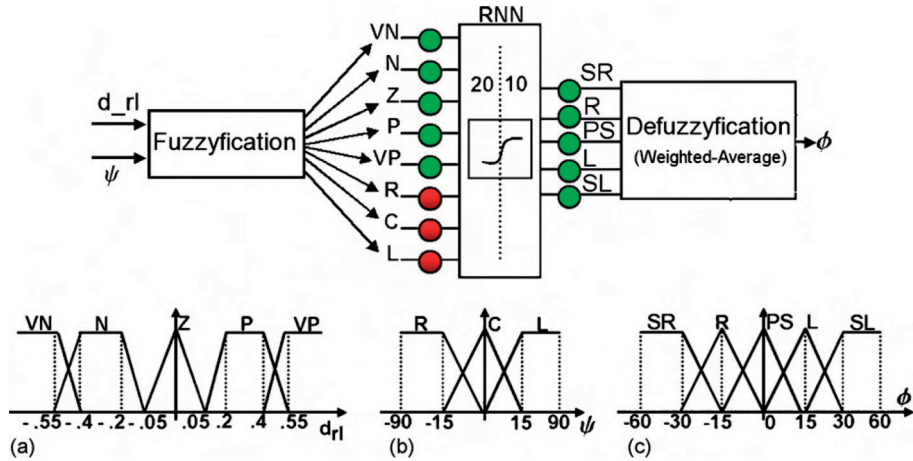


Figure 3. (top) The general scheme for the NFC responsible for the local xy plane. Input variables are the relative position and orientation of the robot; the output variable is the desired direction for the next step. (bottom) (a) Membership functions to fuzzify the rl variable: *VeryNegative* (very close to the right wall), *Negative*, *Zero* (centered), *Positive*, *VeryPositive* (very close to the left wall). (b) Membership functions to fuzzify the ψ variable: *R* (robot pointing towards the right wall), *C* (robot pointing straight), *L* (robot pointing towards the left wall). (c) Membership functions for the output variable: the desired direction can be *StronglyToTheRight* (SR), *ToTheRight* (R), *PointingStraight* (PS), *ToTheLeft* (L), and *StronglyToTheLeft* (SL).

Defuzzyfication

The output of the RNN is defuzzyfied following the weighted-average

$$\Phi = \frac{\sum_{i=1..5} \omega_i * V_i}{\sum_{i=1..5} V_i} \quad (5)$$

where ω_i is the fuzzy value for the i th output membership function (SR,R,PS,L,SL) and V_i is the function's center (SR(-60), R(-15), PS(0), L(15), SL(60)).

Table 1. Table of basic fuzzy rules: the first row represents the stable condition.

Input					Output								
vn	n	d_n			Ψ			ϕ					
		z	p	vp	l	c	r	hl	l	c	r	hr	
0	0	1	0	0	0	1	0	0	0	0	1	0	0
0	1	0	0	0	1	0	0	0	0	0	1	0	0
0	1	0	0	0	0	0	1	0	1	0	0	0	0
0	1	0	0	0	0	1	0	0	0	1	0	0	0
1	0	0	0	0	1	0	0	0	1	0	0	0	0
1	0	0	0	0	0	0	1	1	0	0	0	0	0
1	0	0	0	0	0	1	0	1	0	0	0	0	0
0	0	0	1	0	1	0	0	0	0	0	0	1	0
0	0	0	1	0	0	0	1	0	0	1	0	0	0
0	0	0	1	0	0	1	0	0	0	0	0	1	0
0	0	0	0	1	1	0	0	0	0	0	0	0	1
0	0	0	0	1	0	0	1	0	0	0	0	1	0
0	0	0	0	1	0	1	0	0	0	0	0	0	1

Radius estimation

During the exploration, the AVMR estimates the cross-sectional radius of the tubular structure: the locations sensed through the lateral sensors form a cloud of points, which represent the structure locally. In [17], the authors present an efficient Hough transform for fitting cylinders in clouds of points: the first step is to look for potential directions through the cloud of points; for each direction, one builds up a plane perpendicular to the cylinder axis and projects the 3D points on the plane; finally, a 2D Hough transform for circles is applied on the plane to identify the optimal radius. In our work, we consider the current direction of the AVMR as the best guess for the cylinder axis; we then project the cloud of points on the local yz plane, and fit a circle through a standard 2D Hough transform: this gives us the estimated radius for the cylinder. The length of the AVMR is an important parameter for the radius estimation: when fitting a cylinder, one would like to acquire surface points along the direction of the structure. A longer robot would acquire points along a longer part of the tube, improving the signal-to-noise ratio. On the other hand, if the radius in the structure varies quickly (i.e. if it decreases quickly), detecting points on a long tract might lead to a wrong local estimation (i.e. underestimation of the

radius). Finally, while looking for the best 2D circle on the plane, we have to restrict the search for the radius in a certain range $[r_{min} - r_{max}]$.

The successful navigation of the AVMR in a given virtual environment is therefore governed by few key parameters: the robot's dimensions, its nonholonomic kinematics' constraints (i.e. maximum steering angle), and its sensory system.

Experiments

While exploring a tubular environment, the AVMR has to (1) keep a central position, (2) explore the entire tube, and (3) estimate the radius locally. Few key parameters characterize the system: AVMR's dimensions, maximum steering angle, maximum sensory distance. We generated challenging synthetic environments to assess the effects of these factors on the AVMR's performances: in each experiment, the ideal central line was known, as well as the radius at each location along the central path; thus, for each exploration we could evaluate the average error in detecting the central line, the percentage of covered length, and the error in estimating the radius. The synthetic environments were designed to represent realistic situations in medical datasets: anatomical structures with changing radius, and volumetric images with noise (either normally distributed, or localized).

A set of *Straight-Tubes* with variable radius was used to study the effects of the AVMR's dimensions (figure 4a); *U-Tubes* with different curvatures were used to investigate the effects of nonholonomic constraints (figure 4b); the effect of noise (both as normally distributed and localized) was also tested on the *U-Tubes*. Finally, a set of spirals was used to test the AVMR's performances when all the previous factors are present: changes in radius, curvature, etc. (figure 4c).

The sensory system was the same for all the experiments; referring to figure 1, we have: $\alpha = 45^\circ$ (ranging within $\pm 90^\circ$), $d_l = L/10$, adding up to $N_l = 50$ *left* (and $N_r = 50$ *right*) sensors; $\beta = 45^\circ$ (ranging within $\pm 45^\circ$), $d_t = L/10$, adding up to $N_t = 30$ *top* (and $N_b = 30$ *bottom*) sensors; $\gamma = 30^\circ$, $\delta = 5^\circ$, both ranging within $\pm 60^\circ$ (adding up to $N_f = 125$ frontal sensors).

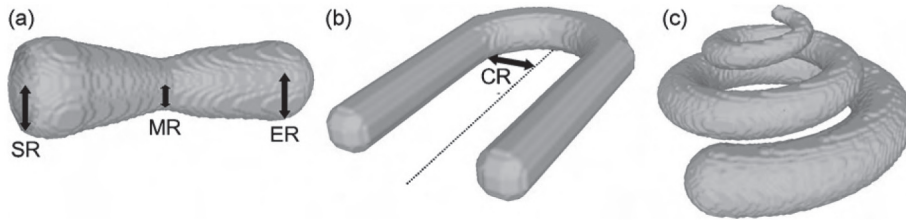


Figure 4. Synthetic datasets used for validation. (a) In *straight tubes*, the radius changes linearly between its value at the starting point (SR), middle point (MR), and end point (ER). (b) *U-tubes* are characterized by different curvature radii (CR). (c) In *spirals* the radius changes linearly from the base to the apex.

AVMR's dimensions

The AVMR's dimensions are important control-parameters for a successful exploration. If the dimensions are too small, the AVMR might start oscillating around the ideal central line; if they are too big, a small error off the ideal line might cause the AVMR to bump against the walls and stop. In Table 2, we summarize the set of straight tubes used for the experiments, and report the results of the exploration: each tube has a length l of 100 voxels, and a radius which changes linearly between three points (starting radius (SR), middle radius (MR), ending radius (ER)). The AVMR's dimensions for these experiments were set to $L=6$ voxels, $W=6$ voxels, and $T=3$ voxels. The speed was set to $v=3$ voxels/step, and the steering angles were constrained to $\Phi \in [-80,80]^\circ$ and $\theta \in [-80,80]^\circ$. In most of the cases in which the diameter went down to 7.5 voxels, the robot could not complete the exploration: this shows that when the robot's width is similar to the tube's diameter, a small error during the exploration causes the robot to bump and stop. In all the other cases, the exploration was successful, the worst-case scenario being the constant radius of 15 voxels: $\mu_{err_cl}=1.64$, $\sigma_{err_cl}=1.24$, $\mu_{err_radius}=1.68$, $\sigma_{err_radius}=1.05$, $\mu_{\%}=97$. In this case, the smallest dimension of the AVMR is 10% of the diameter, and the AVMR starts oscillating during the exploration.

Table 2. Structure of the *straight tubes*: the radius changes linearly between the starting radius (sr), the middle radius (mr), and the ending radius (er) (in voxels).

	Structure			Results				
	sr	mr	er	Central line		Radius		% Covered
				μ	σ	μ	σ	length
stube 1	15	(sr+er)/2	7.5	1.37	0.65	1.72	0.72	97
stube 2	15	(sr+er)/2	5	1.03	0.50	1.59	0.52	97
stube 3	15	(sr+er)/2	3.75	1.00	0.50	1.82	0.80	98
stube 4	3.75	(sr+er)/2	5	-	-	-	-	-
stube 5	3.75	(sr+er)/2	7.5	-	-	-	-	-
stube 6	3.75	(sr+er)/2	15	0.63	0.37	0.66	0.50	98
stube 7	3.75	5	3.75	-	-	-	-	-
stube 8	3.75	7.5	3.75	-	-	-	-	-
stube 9	3.75	15	3.75	0.83	0.39	2.00	1.17	99
stube 10	15	7.5	15	0.67	0.34	1.41	0.61	97
stube 11	15	5	15	0.78	0.38	1.87	0.73	99
stube 12	15	3.75	15	-	-	-	-	-
stube 13	15	15	15	1.64	1.24	1.68	1.05	97
stube 14	7.5	7.5	7.5	0.96	0.64	0.80	0.35	98
stube 15	5	5	5	0.70	0.33	0.89	0.56	96
stube 16	3.75	3.75	3.75	-	-	-	-	-

Results of the exploration: average error and standard deviation (in voxels) for central line detection, radius estimation, and percentage of covered length. Results are not reported for unsuccessful explorations.

AVMR's constraints on steering angles

The AVMR's constraints on steering angles might be useful to incorporate prior-knowledge in the exploration of certain environments (i.e. datasets in which the tube always curves to the right, torus of known curvatures, datasets with noise which should not affect the navigation significantly, etc.). On the other hand, a constraint on the maximum steering angle might cause the robot to bump against the walls in cases with curvatures close to the limit. Considering for simplicity the 2D case (Eqs (1)-(3)), and given a constant angle $\bar{\Phi}$ on the xy local plane, the radius of the circular trajectory is $R = L/\sin(\bar{\Phi})$. In these experiments we constrained $\Phi \in [-30,30]^\circ$ (minimum curvature radius of 12 voxels); U-Tubes were generated with constant radius of 12 voxels, and with different curvature radii (30, 25, 20, and 15 voxels). Dimensions and speed for the

AVMR were the same as used in the previous experiments. Results are reported in Table 3. The exploration failed in the last case (curvature radius of 15 voxels): going slightly off the central line prevents the AVMR to recover and deal with the curve. The other explorations were successful: average error in central line detection $\mu = 0.79$ voxels, $\sigma = 0.04$; average error in radius estimation $\mu = 0.74$ voxels, $\sigma = 0.03$; covered length $\mu = 99\%$, $\sigma = 0.7\%$.

Table 3: Results for *u tubes*: average error and standard deviation (in voxels) for central line detection, radius estimation, and percentage of covered length..

	Central line m (s)	Radius m (s)	% Covered length
U-tube			
Curv. rad. 30	0.77 (0.46)	0.76 (0.46)	98
Curv. rad. 25	0.76 (0.42)	0.75 (0.43)	99
Curv. rad. 20	0.84 (0.43)	0.71 (0.46)	100
Curv. rad. 15	-	-	-
Remove			
2%	0.98 (0.50)	0.72 (0.45)	99
5%	0.99 (0.42)	0.76 (0.46)	98
10%	1.06 (0.49)	0.73 (0.45)	98
15%	-	-	-
20%	-	-	-

Results are not reported for unsuccessful explorations

Robustness to noise

Robustness to noise was tested in a set of experiments. Surface points were randomly removed from the curved part of a U Tube (radius of 12 voxels): the percentage of surface points to be removed varied from 2% to 20%. Results are reported in Table 3: when more than 15% of the surface was removed, the AVMR failed to complete the exploration. In the other cases the exploration was successful: average error in central line detection $\mu = 1.01$ voxels, $\sigma = 0.04$; average error in radius estimation $\mu = 0.74$ voxels, $\sigma = 0.02$; covered length $\mu = 99\%$, $\sigma = 0.4\%$. Figure 5 shows some close-ups of the explorations.

These experiments showed the importance of the sensory system in noisy environments: in particular, both the maximum sensory distance and the density of the

sensors would improve the performances on these datasets, allowing the AVMR to be less sensitive to noise.

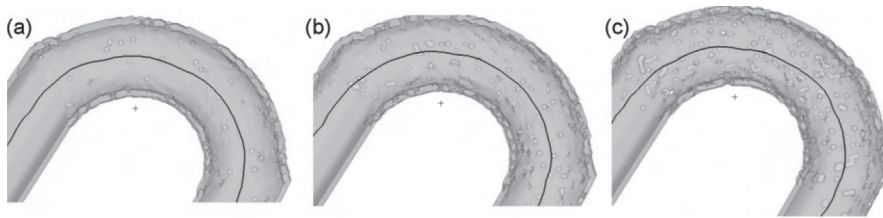


Figure 5. Close-ups on the curved section of the *u tubes* (with detected central line) with increased noise (2%, 5%, and 10% of surface removed).

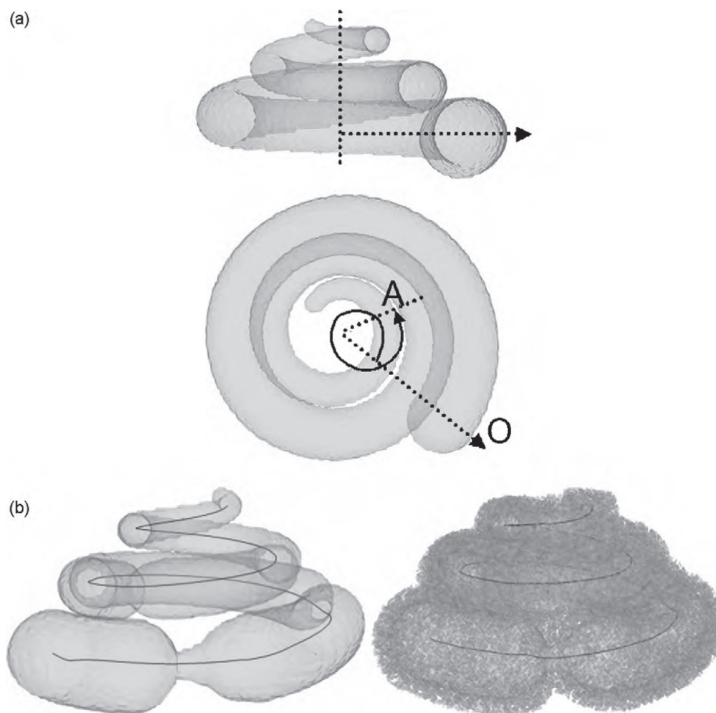


Figure 6. (a) Reference system in spiral datasets and cochleae. Given the origin-axis O , to each point A along the path one can associate an angle ranging from 0 to 900° (two and half turns). (b) Spirals with narrowing and noise, and central line detected by the AVMR. (left) The original spiral of figure 4c is modified by introducing narrowing along the path. (right) Noise is added to the new spiral in different levels and ways (see section 3.4 for details).

Spiral datasets

In the first experiment, a spiral was generated with a radius linearly changing from 13 voxels, down to 3 voxels, over a length of almost 480 voxels (see figure 4c): we evaluated the average error for central line detection, the radius estimation, and the covered length at 630° from the starting point (see figure 6a). In the second experiment we modified the spiral introducing narrowing along the way (figure 6b). Finally, noise was introduced on this last spiral: 30% of surface points were randomly re-displaced, with a displacement varying from 1 to 5 voxels farther away from the surface (see figure 6b). Results are reported in Table 4.

Table 4: Results for *spirals*: average error and standard deviation (in voxels) for central line detection, radius estimation, and percentage of covered length at a defined distance.

	Central line m(s)	Radius m(s)	% Covered length
Spiral	1.20 (0.57)	0.64 (0.39)	103
Sp.-narrowings	1.36 (0.48)	0.97 (0.80)	105
Sp.-incr-area-1	1.49 (0.57)	0.69 (0.74)	108
Sp.-incr-area-2	1.71 (0.50)	0.65 (0.73)	108
Sp.-incr-area-3	1.60 (0.57)	0.64 (0.79)	106
Sp.-incr-area-4	1.64 (0.53)	0.59 (0.69)	106
Sp.-incr-area-5	1.44 (0.51)	0.80 (0.77)	109
Average	1.49	0.71	106
St. dev.	0.18	0.13	1.97

Results are not reported for unsuccessful explorations.

Final considerations on the AVMR's properties

The results on synthetic data pointed to some important issues one should consider when designing the AVMR. The ideal cross-sectional dimensions of the robots should be about 50% of the structure's diameter: a smaller robot might oscillate too much while a bigger robot might bump against the walls and stop. The maximum steering angle is an important tool to incorporate prior knowledge on the anatomical structure. Finally, the appropriate trade-off between computational performances and robustness to noise should be found: increasing the number of sensors and the maximum distance sensed by the sensors makes the AVMR less sensitive to noise, although it increases the computational load.

Application to the micro-CT datasets

We applied the AVMR to the exploration of eight human cochleae. The cochlea, or inner ear, is a spiral organ located in the petrous bone, and responsible for the conversion of sound vibrations into action potentials on to the auditory nerve. Cochlear dysfunction at the level of the hair cells might lead to sensorineural hearing loss or deafness. In case of bilateral severe-to-profound hearing loss or total deafness, cochlear implants (CIs) can be used to improve this condition: an electrode array with several contacts is implanted in the cochlea, and connected to a receiver/converter unit (implanted under-skin) which converts air vibrations into electrical stimuli [18]. The cochlea has a tonotopic organization representing high frequencies at the base and low frequencies at the apex. Since different electrode contacts along the implant respond to different frequencies, the insertion depth of the electrode array will ultimately determine the speech perception outcome. Differences in size and form of the cochlea will influence the tonotopic organization. A great variability of cochlear length between subjects has been reported. [19,20] Since sound frequencies are mapped along the cochlea relatively to its length, [21] both researchers and surgeons share a great interest in the assessment of the individual cochlear length.

As a first step in this direction, we analyzed eight datasets acquired through micro-CT (see figure 7a): images were acquired on a high-resolution (*in vivo*) micro-CT scanner (Skyscan-1076, Aartselaar, Belgium) resulting in an isotropic $17\ \mu\text{m}$ resolution (more information on the acquisition protocol can be found in [22]). The high resolution images provided by this technique are essential to validate any analysis tool. A summary of the micro-CT characteristic, as well as the parameters set for the AVMR, are reported in Table 5 (because of the high dimensions of the datasets, we sub-sampled the data to an isotropic resolution of 0.07 mm). The multi-slice micro-CT scans (see figure 7a) provide us with orthogonal slices of the cochlea which are not suitable for a thorough exploration. The spiral-like shape of the cochlea requires a fully 3D approach, based on the entire volume rather than on subsequent 2D slices.

Before performing any analysis, one needs to introduce a coordinate system on each cochlea, as shown in figure 7b: first, a z vector is identified along the bony pillar of the cochlea; then, an *origin axis* is defined as perpendicular to the z vector and passing through the round window of the cochlea. Any location along the cochlea is uniquely identified by the cumulative angle from the *origin axis* (as previously described for the

spiral synthetic environments, figure 6a). Given a coordinate system, the corresponding cochlea dataset could be re-sliced at pre-defined angles; thus, a new set of slices were obtained in which an experienced head and neck radiologist could manually delineate the center of the canal (central path) used for validation.

Using semi-automatic 3D segmentation tools [23], an expert was asked to segment the original datasets and create the binary environments needed for the exploration (see figure 7a). Starting and ending points for explorations were identified manually: the AVMR could successfully explore all the datasets, detecting the central line, evaluating the length of the structures, and estimating the radius at each location. The length detected manually was compared to the one detected by the robot at 630° (see figure 6a)¹: the average error was below 4% of the length (see figure 8).

Table 5: Characteristics of the micro-CT cochlea datasets and parameters for the AVMR.

Datasets	
dimensions x-y-z (voxels)	178-169-114
resolution x-y-z (mm/voxel)	0.07-0.07-0.07
Robot	
dimensions L-W-T (mm)	0.5-0.2-0.2
speed (mm/step)	0.07
Φ range (= θ range) ($^\circ$)	[-35,35]
max_dist_s	1.5

For the AVMR, max_dist_s refers to the maximum distance the sensors can propagate.

1. Electrodes are usually implanted up to one and half turns, which equal 540 degrees. Thus, 630 degrees is a sufficiently distant point for comparison.

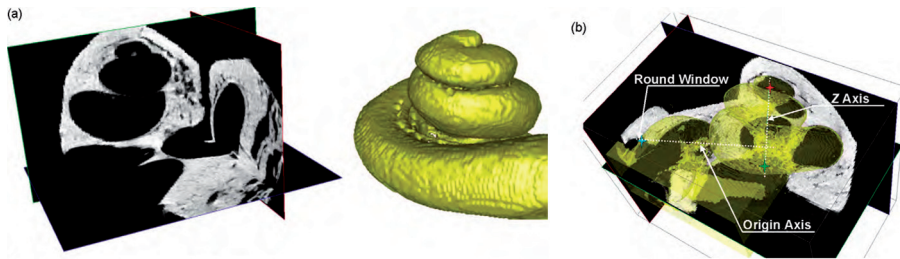


Figure 7. (a) (*left*) A micro-CT dataset of a cochlea: the lumen where the electrode is to be inserted has a low density in the images. (*right*) Results of 3D semi-automatic segmentation. (b) The origin axis of the coordinate system in the cochlea is perpendicular to the z vector, and passing through the *round window*.

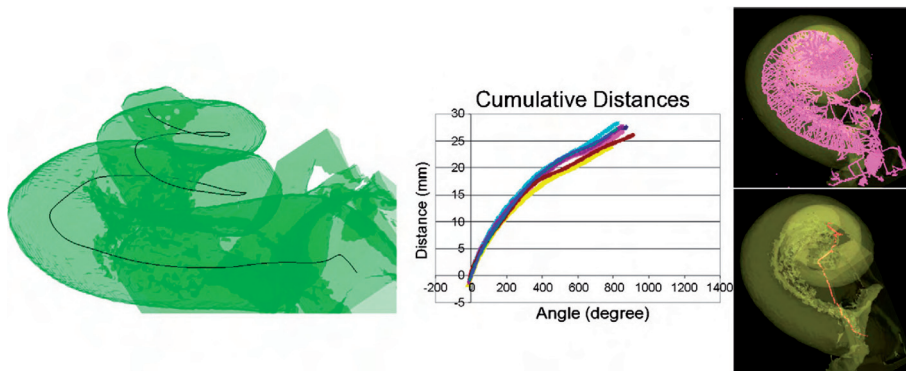


Figure 8. (*left*) Example of central line detected in one of the cochleae: the uniqueness and smoothness of the trajectory are inherited qualities of the nonholonomic constraints. (*Center*) Cumulative lengths for the 8 cochleae. The plots show the cumulative length at increasing angles: the lengths at 630° are used for the comparison with manually delineated central lines. (*Right*) Example of how a simple skeletonization and pruning approach might lead to a wrong central line: the skeleton (*Top*) is made of several small branches (due to noise in the cochlear surface) which need to be pruned; nevertheless, simply choosing for the shortest path from the starting point to the target point does not provide the desired central line.

Discussion and conclusions

The concept of a virtual mobile robot exploring 3D medical image datasets represents the main novelty of our work. By merging together robotics, artificial intelligence, and medical image analysis, we aim at autonomous explorations of virtual anatomical structures. This work has presented our preliminary results.

Using the AVMR for virtual endoscopy and quantitative analysis presents several advantages. Uniqueness, smoothness, and connectivity are reported to be among the most important factors in central line detection [24-26]. The final trajectory obtained by the AVMR is always unique, in contrast to what happens with skeleton-based technique: thus, there is no need to prune the output to remove spurious side branches (see figure 8). The smoothness of the central line and its continuity are granted by the nonholonomic constraints: the AVMR could never jump from one location to another, nor perform abrupt changes in its direction. Being provided with a virtual camera, internal views are immediately available during the exploration. The interaction with the system is highly intuitive: the AVMR can be stopped at any time to better explore the surrounding through the camera. Providing quantitative information is essential. The module for radius-fitting makes use of the AVMR's local direction to guess the best orientation of a cylinder to be fitted: while looking for cylinders in 3D, not having to test for different orientations clearly improves the performances. Previous works in literature have highlighted the importance of combining prior-knowledge of the environment with local information [27,28]: using only local information (i.e. the gradient) fails when the signal-to-noise ratio is not sufficiently good. The AVMR makes use of local information while sensing its surrounding. Prior-knowledge is integrated in the system in two ways. By setting up the structural and kinematics constraints properly, one can limit the AVMR to explore only corridors of a certain size, to perform curves with certain curvatures, be less sensitive to noise, etc. A second way to introduce global knowledge could be through the NFC. In its original design [9], the RNN was followed by a second (smaller) feed-forward neural network (ORNNN) responsible for defuzzifying the output membership functions into the desired direction: if such a network is introduced in the system, it could be trained by an expert who would guide the AVMR through particular environments.

Several synthetic environments were generated to analyze how the key parameters of our system influence the final performances of an exploration. Dimensions clearly

determine the minimum corridors the AVMR can move through: by analyzing the results on *Straight Tubes*, we found out that the best dimensions for the robot's thickness/width should be about 50-60% of the diameter. The length of the AVMR should be set considering the curvatures in the dataset as well as the localized noise (openings): the shorter the robot, the easier it will be to go through highly curved corridors; on the other hand, too short a robot will be more easily affected by localized noise in the structure. Constraining the maximum steering angle could have beneficial effects in noisy datasets, as well as in constantly curved ones: in cases like the spiral (or the cochlea), if the AVMR is provided with unlimited sensory distance, the final trajectory might be closer to the internal wall. When the AVMR is close to a curve, i.e. to the left, the frontal sensors will detect much more space on the left side than on the right one: as a consequence, the NFC will try to correct for this by forcing the AVMR further to the left. Limiting the maximum sensing distance, and/or the maximum steering angle can prevent this behavior. The density of sensors is another important tradeoff: increasing the number of sensors increases the computational time, but provides the robot with a finer representation of its surrounding, improving robustness to noise. Finally, speed has an effect on the smoothness of the final path: we found experimentally that setting the speed at half the length of the AVMR per step is a good choice. Tuning the system to work in different environments proved to be an easy task. All the parameters are intuitive and directly related with the structure one wants to analyze. The performances for central line detection were very satisfactory, the average error being always below 2 voxels, even when extreme noise was introduced (as for the spirals), and being below 1 voxel in most of the other cases. Also the estimation of the radius proved robust and accurate.

In cochlear implants, the patency and morphology of the cochlea is studied with computer tomography and magnetic resonance imaging. Both imaging modalities render complementary information: whereas CT visualizes bony details and surgical landmarks, MRI provides excellent soft tissue characterisation [29]. The 2-dimensional representation of these data however does not display the height of the cochlear spiral and thus the length of the cochlear spiral cannot be determined accurately. Computer aided reconstructions made from histologic sections, CT and/or MRI-scans [30-33] have been described to improve presurgical planning and quantitative study of anatomical structures. Ketten et al. [33] calculated the cochlear canal length assuming that the

Archimedian spiral provides the single closest fit of any regular curve for the midline of the average human cochlear canal. In our work, we analyzed micro-CT datasets as a first step towards the validation of CT measurements.

The manual analysis of micro-CT cochleae is a tedious and time-consuming task. It requires going through hundreds of slices to identify contours, central positions, etc. Alternatively, one could reduce the number of slices and interpolate between them: even in this case, a manual analysis over only 30 slices took in average one hour per dataset. Being able to autonomously explore such environments is of great benefits. By just giving starting and ending positions, the AVMR could successfully analyze the eight cochleae, providing results comparable to those obtained manually, and also estimating the changes in radius along the path (considering both semi-automatic segmentation and AVMR analysis, the required time per cochlea went down to about 15 minutes). Although not in the scope of this paper, the exploration with the AVMR allowed us to perform further analyses: once the central path is detected, the cochlea can be straightened into a tube. In the re-sliced dataset, different sections of the cochlea (i.e. scala tympani, scala vestibuli) are easier to identify automatically and analyze in further explorations. Micro-CT datasets are not directly applicable in clinical routine; nevertheless, a thorough analysis of the cochlea's anatomical variations in high-resolution images will allow a comparison with results obtained in corresponding CT and MR datasets, a necessary step for the validation of any study based on clinical CT.

While navigating through an organ, the AVMR decides what are the boundaries of the structure by using a global threshold on the intensity (this is true also for pre-segmented datasets, where the intensity is binary): we are investigating how to introduce a more local knowledge in the segmentation by means of a fuzzy classifier trained on gray-value intensities. Still, it is important to point out that the distinction between navigation in binary or in gray-value images lies on a thin line: any approach based on intensity levels goes down, sooner or later, to what is lumen and what is not. Another issue related with navigation is the behavior in branching points: as currently implemented, the AVMR considers branches as noise/openings and follows one trying to be affected as little as possible by the other: although useful in certain applications (i.e. analysis of one side of the carotid arteries), for other applications we are designing new navigation tools able to detect branches, duplicate the robot, and continue the exploration in parallel. Modules for novelty detection will also be added: the AVMR should be trained in normal environment (i.e. normal carotid arteries) and then highlight new sensor information

(e.g., stenosis or aneurysms): studies on novelty filters for mobile robots are abundant in literature (i.e. [34]), which could turn the AVMR into a security agent able to highlight abnormal situations in a given environment. Finally, a few words on the medical datasets presented in this manuscript. The limited number of micro-CT cochleae is due to the rather unexplored field: only few research centers have recently started investigating the properties of the cochlea, thanks to advances in micro-CT technologies. The interest in the field is high because of the impacts the results will have on surgical implants based on clinical CT imaging. In the future, we are planning to use the AVMR to bridge the gap between post-mortem micro-CT and clinical CT images. Moreover, the qualitative comparison with other methods presented in this manuscript should be completed with a quantitative comparison with other approaches for central line extraction: nevertheless, the comparison of our results with the manually delineated central line has already proved the good performances of our approach.

Acknowledgment

This work was supported by the Technology Foundation STW (project number 06122), and by Medis medical imaging systems bv, Leiden, The Netherlands (www.medis.nl).

References

1. Truyen R, Deschamps T, Cohen L. Clinical evaluation of an automatic path tracker for virtual colonoscopy. In: Niessend W.J, Viergever M.A., editors. *Lecture Notes in Computer Science*, Springer 2208, Utrecht, Netherlands 2001:169–76.
2. Kiraly A, Helferty J., Hoffman E, McLennan G, Higgins W. Three-dimensional path planning for virtual bronchoscopy. *IEEE Trans. Med. Imaging* 2004; 23(11):1365–79.
3. Haigron P, Bellemare M, Acosta O, Goksu C , Kulik C, Rioual K et al. Depth-map-based scene analysis for active navigation in virtual angioscopy. *IEEE Trans Med Imaging* 2004; 23(11):1380–90.
4. Wahle A, Olszewski M, Sonka M. Interactive virtual endoscopy in coronary arteries based on multi-modality fusion. *IEEE Trans Med Imaging Virtual Endosc* 2004; 23(11):1391–403.
5. Marquering H, Dijkstra J, de Koning P, Stoel B, Reiber J. Towards quantitative analysis of coronary cta. *The Int J Cardiovasc Imag* 2005; 21 (1):73–84.
6. Rentschler M, Dumpert J, Platt S, Ahmed S, Farritor S, Oleynikov D. Mobile in vivo camera robots provide sole visual feedback for abdominal exploration and cholecystectomy. *Surg. Endoscopy* 2006; 20:135–8.
7. Thongchai S, Suksakulchai S, Wilkes D, Sarkar N. Sonar behavior-based fuzzy control for a mobile robot. In: *IEEE Proceeding of International Conference on Systems, Man, and Cybernatics*, volume 5, Los Alamitos, Ca; 2000 p 3532–7.
8. Braunstingl R, Sanz P, Ezkerra J. Fuzzy logic wall following of a mobile robot based on the concept of general perception. In: *Proceedings of the 7th International Conference on Advanced Robotics (ICAR)*. Spain: Sant Feliu de Guixols;1995, p 367–76
9. Ng K, Trivedi M. A neuro-fuzzy controller for mobile robot navigation and multirobot convoying. *IEEE Trans Sys, Man, Cybernet B: Cybernet* 1998; 28(6):829–40.
10. Scorcioni R, Ng K, Trivedi M, Lassiter N. Monif: a modular neuro-fuzzy controller for race car navigation. In: *IEEE International Symposium on Computational Intelligence in Robotics and Automation (CIRA 1997)*, Washington:, IEEE Computer Society Press;199, p. 74–79.
11. Zimmer U, von Puttkamer E. Realtime-learning on an autonomous mobile robot with neural networks. In: *Proceedings Euromicro '94*; 1994, p.40-4.
12. Chatila R, Lacroix S, Betge-Brezetz S, Devy M, Simeon T. Autonomous mobile robot navigation for planet exploration - the eden project. In: *IEEE International Conference on Robotics and Automation*. Washington: IEEE Computer Society Press; 1996.
13. Duckett T, Nehmzow U. Self-localisation and autonomous navigation by a mobile robot. In: *Proceedings of UK 99 on Towards Intelligent Mobile Robots (TIMR)*, Bristol, UK, Manchester University Technical Report UMCS-99-3-1, ISSN 1361-6161; 1999.
14. Thrun S. A lifelong learning perspective for mobile robot control. *Proceedings of the IEEE/RSJ/GI International Conference on Intelligent Robots and Systems*, vol. 1, 1994, p. 23–30.
15. Admiraal-Behloul F, Lelieveldt B, Ferrarini L, Olofsen H, Geest Rvd, Reiber J. A virtual exploring mobile robot for left ventricle contour tracking. *IEEE-International Joint Conference on Neural Networks (IJCNN2004)*, Budapest, IEEE Computer Society Press (Washington) 2004; 1:333–338.

16. Wang X, Tang Z, Tamura H, Ishii M, Sun W. An improved backpropagation algorithm to avoid the local minima problem. *Neurocomputing* 2004; 56:455–60.
17. Rabbani T, Heuvel Fvd. Efficient hough transform for automatic detection of cylinder in point clouds. ISPRS WG III/3, III/4, V/3 Workshop, Laser scanning 2005, Enschede, The Netherlands, 2005.
18. Zeng F. Trends in cochlear implants. *Trends in Amplification* 2004; 8(1):1–34.
19. Sato H, Sando I, Takahaschi H. Sexual dimorphism of the human cochlea - computer 3d measurement. *Acta Oto-Laryngologica* 1991; 111:1037–40.
20. Ketten D, Vannier M, Skinner M, Gates G, Wang G, Neely J. In vivo measures of cochlear length and insertion depth of nucleus cochlear implant electrode arrays. *Ann Otol Rhinol Laryngol* 1998; 107:1–16.
21. Sridhar D, Stakhovskaya O, Leake P. A frequency-position function for the human cochlear spiral ganglion. *Audiol Neurotol* 2006; 11(1):16–20.
22. Postnov A, Zarowski Z, de Clerk N, Vanpoucke F, Offeciers F, van Dyck D et al. High resolution micro-ct scanning as an innovatory tool for evaluation of the surgical positioning of cochlear implant electrodes. *Acta Oto-Laryngol* 2006; 126(5):467–74.
23. Admiraal-Behloul F, van den Heuvel D, Olofsen H, van Osch M. Fully automatic segmentation of white matter hyperintensities in mr images of the elderly. *Neuroimage* 2005; 28(3):607–17.
24. Tschirren J, Palágyi K, Reinhardt J, Hoffman E, Sonka M. Segmentation, skeletonization, and branchpoint matching - a fully automated quantitative evaluation of human intrathoracic airway trees. In: Goos G, Hartmanis J, van Leeuwen J, editors. *Medical Image Computing and Computer-Assisted Intervention (MICCAI'02)*, Springer Berlin (Heidelberg), vol LNCS 2489, Tokyo, Japan, 2002; p. 12–9.
25. Tran S, Shih L. Efficient 3d binary image skeletonization. In: *Proceedings of IEEE Computational Systems Bioinformatics Conference Workshop (CSBW'05)*, Washington: IEEE Computer Society Press; 2005, p 364–72
26. Yang Y, Zhu L, Haker S, Tannenbaum A, Giddens D. Harmonic skeleton guided evaluation of stenoses in human coronary arteries. In: Duncan JS, Gerig G, editors, *Medical Image Computing and Computer-Assisted Intervention (MICCAI'05)*, Palm Springs, California, volume LNCS 3749, Springer-Verlag, Heidelberg; 2005, p. 490–7.
27. Passat N, Ronse C, Baruthio J, Armspach J, Maillot C. Magnetic resonance angiography: From anatomical knowledge modeling to vessel segmentation. *Med Image Anal* 2006; 10:259–74.
28. Hassouna M, Farag A, Hushek S, Moriarty T. Cerebrovascular segmentation from tof using stochastic models. *Med Image Anal* 2006; 10:2–18.
29. Trimble K, Blaser S, James A, and Papsin B. Computed tomography and/or magnetic resonance imaging before pediatric cochlear implantation? developing an investigative strategy. *Otol. Neurotol* 2007; 28(3):317–24.
30. Bartling S, Peldschus K, Rodt T, Kral F, Matthies H, Kikinis R, Becker H. Registration and fusion of ct and mri of the temporal bone. *J Comput Assist Tomogr*, 2005; 29(3):305–10.
31. Qiu M, Zhang S, Liu Z, Li LTQ, Li K, Wang Y, et al. Visualization of the temporal bone of the chinese visible human. *Surg Radio Anat* 2003; 26(2):149–52.
32. Frankenthaler R, Moharir V, Kikinis R, van Kipshagen P, Jolesz F, Umans C, et al. Virtual otoscopy. *Otolaryngol Clin Norh. Am* 1998; 31(2):383–92.

33. Ketten D, Skinner M, Wang G, Vannier M, Gates G, Neely J. Abstract in vivo measures of cochlear length and insertion depth of nucleus cochlear implant electrode arrays. *Ann Otol Rhinol Laryngol Suppl* 1998; 175:1–16.
34. Marsland S, Shapiro J, Nehmzow U. A self-organizing network that grows when required. *Neural Netw* 2002; 15:1041–58.

8

Anatomic Considerations of Cochlear Morphology and its Implications for Insertion Trauma in Cochlear Implant Surgery

BM Verbist, L Ferrarini, JJ Briare, A Zarowski, F Admiraal-Behloul,
H Olofsen, JHC Reiber, JHM Frijns

Otology & Neurotology 2009; 30(4): 471-7

Abstract

Hypothesis: The goal of this study is to analyze the 3-dimensional anatomy of the cochlear spiral and to investigate the consequences of its course to insertion trauma during cochlear implantation

Background: Insertion trauma in cochlear implant surgery is a feared surgical risk, potentially causing neural degeneration and altered performance of the implant. In literature, insertion trauma is reported to occur at specific locations. This has been ascribed to surgical technique and electrode design in relation to the size of the scala tympani. This study investigates whether there is an underlying anatomic substrate serving as a potential source for insertion trauma at these specific locations.

Methods: The 3 dimensional path of the cochlear spiral of 8 human temporal bones was determined by segmentation, skeletonization, distance mapping, and wave propagation technique applied on microcomputer tomography (CT) images. Potential pressure points along this path were estimated with linear regression.

Results: The cochlear lumen shows a noncontinuous spiraling path leading to potential pressure points during cochlear implantation at the basilar membrane in the region of 180 to 225 (12-14mm) and 725 degrees (22-26mm) and at the floor of the scala tympani around 0 to 90, 225 to 270 and 405 to 450 degrees.

Conclusion: Our data favour the idea that the intrinsic 3-dimensional cochlear morphology contributes to the risk for insertion trauma during cochlear implantation at specific locations.

Introduction

All currently available commercial cochlear implants (CIs) use an array of electrode contacts mounted on a silastic carrier, which is surgically inserted into the scala tympani (ST) via the round window or a cochleostomy created nearby. The electrode array typically extends for some 20-28 mm from the cochleostomy, depending on device used. Some electrode arrays are “straight” in that, after insertion, they tend to lie along the lateral wall of the ST, whereas other “perimodiolar” designs incorporate a pre-curved shape such that, after insertion, they are located along the medial wall, that is, closer to the target neural elements (spiral ganglion neurones).

It is well known that opening of the cochlea and insertion of the array causes damage to the cochlear structures, the effects of which are most obviously observed as deterioration of residual (acoustic) hearing thresholds. This is clearly an area of concern, and a considerable number of studies have focused on insertion trauma in cochlear implant surgery. The major concern is that damage to sensitive cochlear structures might cause degeneration of spiral ganglion cells, as has been shown in animal studies. [1,2]

Although the effect of trauma in human cochleae is largely unknown, it seems reasonable to believe that preservation of neural structures is critical for both short- and long-term performance. In profoundly deaf individuals, loss of any residual functioning hair cells is probably of little consequence. However, relatively serious damage, particularly involving rupture of the basilar membrane, also produces death of spiral ganglion cells and displacement of the array may result in undesirable modification of the match between the tonotopic orientation of the array and the organ of Corti. In the case of electric acoustic stimulation - a method that combines electric stimulation of high frequency portions of the cochlea with amplified acoustic stimulation of low-frequency hearing – cochlear trauma will contribute significantly to success or failure of intra-operative hearing preservation. [3,4] Taking into consideration that many infants and young children receive a cochlear implant, it must be ensured that neural degeneration is minimized. Current devices are anticipated to remain functional for many years, but for these recipients revision surgery must be expected at some stage in their life. Reimplantation would be expected to be problematic if the original implantation has caused damage to the cochlear structures.

Alternative therapies, such as stem cell therapy are also currently under development and it is likely that the less damage has been done, the better the chances of benefit from these new techniques will be.

To minimize trauma to the basilar membrane, the osseous spiral lamina, the spiral ligament, and Reissner membrane modern electrode designs have incorporated vertical stiffness of the electrode carrier whereas horizontal movements are kept more flexible. In this way, upward excursion of the electrode array is reduced. Despite these adjustments, insertion trauma is repeatedly reported to occur at specific locations, notably at the base [5,6], at approximately 180 degrees [7-10] and in deep insertions of more than 400°. [11-13] Trauma at the base has been related to surgical technique [6,14,15], whereas a mismatch in electrode array size and volume of the scala tympani might cause trauma at the upper levels [11]. Studies of the detailed anatomy of the scala tympani have previously focused on the height, width and cross-sectional area [16-19] of the scala tympani, with variable figures reported. Hatsushika et al. [19] reports a rapid decrease of dimensions within the first 1.5mm from the round window, followed by a gradual reduction. Others have reported non-monotonic tapering with some expansions of the scala tympani along its path.

As an electrode array is inserted, it will tend to follow the lateral wall of the ST much of the time. At some points, it may also contact the superior surface of the ST (i.e., vicinity of the basilar membrane) or the floor of the ST, but is presumably less likely to impact the medial wall. There may be irregularities along any of these surfaces, but it seems logical to assume that significant trauma is most likely as a result of contact with the basilar membrane, where membrane rupture and/or electrode excursion out of the ST will have major consequences.

Little is known about the rising course of the cochlear spiral. In this study we will investigate the steepness of the cochlear spiral based on micro-computed tomographic (CT) images, to test the hypothesis that irregularities in the rising course will occur at similar points to those reported to produce resistance during surgical insertion. The goal of this study is to see whether this anatomical substrate might be an underlying cause of insertion trauma in cochlear implantation.

Materials & Methods

Micro-computed Tomography of Temporal Bones

Eight human temporal bones have been harvested and preserved in formalin. The bony labyrinths were isolated from the temporal bones, hereby reducing the volume of the specimens to approximately 2-3 cm³. To increase the contrast between the intracochlear structures and to visualize the membranes, the perilymph was gently removed through a small hole drilled at the cochlear apex and through a micropuncture in the round window membrane. The bones were then wrapped in parafine foil to prevent drying and then imaged. A SkyScan-1076 micro-CT scanner (Aartselaar, Belgium) was used. This scanner is optimized for in-vivo imaging of small animals. The X-ray source and detector are rotating around the object. The scanner provides a resolution of up to 9 microns (pixel size of the detector) and has a 5 μm air-cooled X-ray source. The imaging time was approximately 2 hours. Acquired projections were reconstructed as virtual slices using Feldkamp algorithm. 3-D models were built from the obtained cross-sections by Skyscan software packages. Each reconstruction set consisted of approximately 750 slices of 1000 x 1000 pixels with a resolution of 17.7 μm.

Image Processing and Central Path Measurements

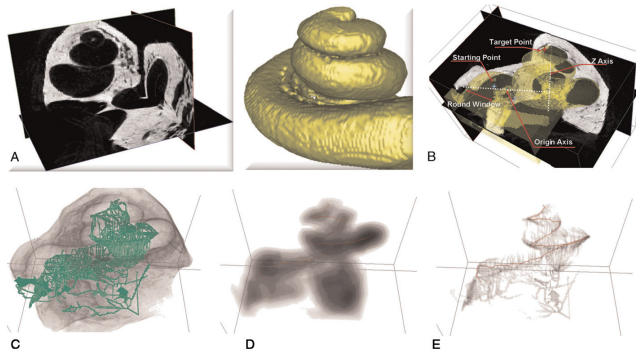


Figure 1. (A), Given the sub-sampled microCT dataset, a 3-D region growing is applied to segment the cochlear canal. (B), A local coordinate system is given. (C), The skeleton presents several side branches because of the surface irregularities. (D), In distance map, each voxel is associated with its distance to the closest surface points. (E), A wave-prop applied to the skeleton and modulated by the distance map provides the final central path.

We applied 3-dimensional (3-D) segmentation of the cochlear lumen in all 8 datasets. The very high resolution of each dataset would severely limit the computational performances of the automatic segmentation. Thus, as a first step, each dataset was down-sampled to an isotropic resolution of 0.07 mm. Subsequently, a simple 3D region growing algorithm was used to segment the cochlear lumen (figure 1A). Starting from a voxel within the cochlear lumen, the algorithm segments the cochlea by including all neighboring voxels with the same intensity as the starting voxel. A radiologist with expertise in head and neck imaging visually checked all the results, to guarantee the correctness of the final segmentation.

A 3-D coordinate system was applied with the x- and y- plane parallel to the basal turn and the z-axis positioned in the center of the modiolus (figure 1B). The z-axis was defined by two points, marked in the center of the modiolus. Next, the starting and target positions for exploration of the cochlear spiral path were manually identified. The target position was placed at the apex of the cochlea. The starting point was defined in the center of the cochlear duct at the level of the anterior border of the round window. A line from the intersection of the z-axis and the basal turn to this starting point defined the x-axis. This approach is similar to the method described by Skinner et al. [20] used to evaluate insertion depths of cochlear implants.

To detect the central path, a combination of well-known image processing techniques was applied. First, the skeleton of the segmented cochlear duct was evaluated (figure 1C): [21-23] the boundaries of the segmented cochlea were eroded until only a skeleton consisting of 1-dimensional branches was left (figure 1C). The skeleton of such anatomic data can be extremely noisy due to irregularities on the surface. Our goal was to find the *central* path along the cochlear turns within this skeleton, which links the starting point at the round window with the target point at the apex. First, to get rid of the noise, a distance map was evaluated: minimum distances of each skeleton voxel from the surface were assessed. Thus, the most central voxels within the skeleton showed a longer distance to the closest surface points than the more peripheral voxels within the skeleton (figure 1D). Finally, the wave-prop technique [24] was applied to remove the side branches and find the central path. A wave is propagated through the skeleton starting at the voxel closest to the starting point: at each location, the wave propagation velocity is modulated by the distance map of the corresponding voxel. The greater the distance from the surface of the skeleton; thus, the more central the voxel, the faster the wave could propagate. Therefore the fastest path from the starting point to

the target location reveals the spiral central path (figure 1E). Longitudinal and angular measurements of the central luminal path were obtained and the coordinates (x , y , z) of each point were stored for further analyses.

Data Analysis

The aim of the analysis was to determine the most likely positions at which a cochlear implant might induce pressure on cochlear structures, such as the basilar membrane and the wall of the scala tympani. The pressure points on cochlear structures during electrode insertion could be caused by deviation of the cochlear duct from a smooth trajectory. With a rapid increase in vertical elevation of the cochlear lumen, the orientation of the array will be altered: because of the interaction between the tip of the electrode array and the floor of the scala tympani the tip will bend upwards. If the vertical elevation drops the implant will adjust its course as a result of pressure against the basilar membrane (figure 2). To localize the potential pressure points of the cochleae under study the z -coordinate profiles of the central paths were analyzed. Skinner et al. [25] has reported that the centroid line falls approximately at the junction of the basilar membrane and osseous spiral lamina. The direction followed by a cochlear implant during insertion was estimated by a linear regression line, measured over a distance of approximately 2 mm along the cochlear lumen, from a certain point within the cochlea to the basal end of the cochlea. The optimal direction for the implant to follow from this point onward was estimated by a linear regression line from that point towards the apex. The difference between the two slopes was used as an estimation of the 'bend' that the implant needs to make at that point in the cochlea. This bending profile shows clear maxima. These are used to define the bending points, that is, the points where the implant makes the largest vertical changes in direction during insertion. Figure 3 shows a detail of the z -coordinate profile of one cochlea illustrating the linear regression lines at four bending points. The symbols indicate a pressure point against the basilar membrane (\square) or the floor of the scala tympani (\circ).

The course of the path was expressed in function of longitudinal distance. At the bending points recalculations towards angular cochlear coordinates were performed. The analysis was automated using Matlab (MathWorks, Inc. Natick, MA, USA) with curve fitting toolbox. Statistical analysis was performed with probability measures.

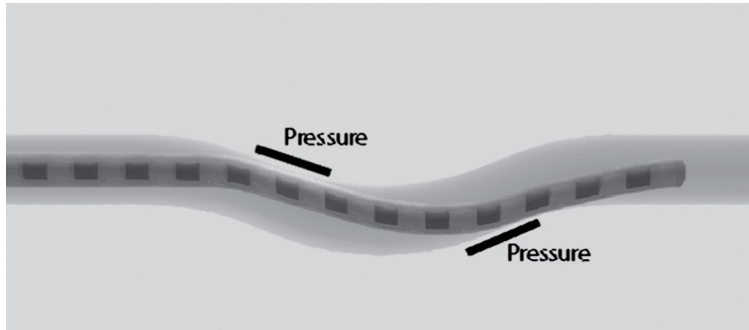


Figure 2. Schematic drawing of the ST illustrating the potential effects of changes in the course of the upward spiraling cochlea on a cochlear implant electrode array during insertion. A downward slope will redirect the course of the implant because of pressure at the upper limit or basilar membrane. A steep upward slope will provoke the tip of the electrode to press against the floor of the scala tympani and bend upwards.

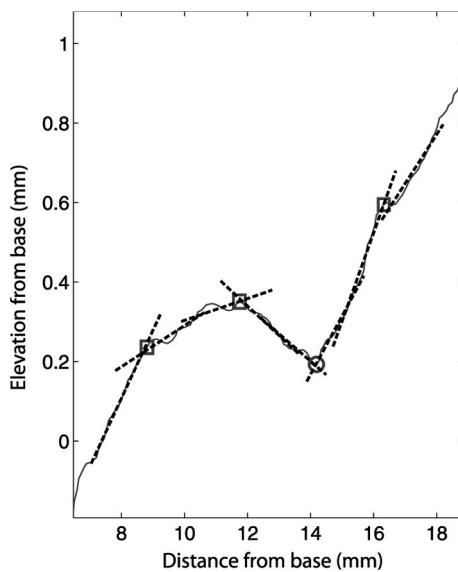


Figure 3. z -coordinate profile of 1 cochlea (A) : the course of the central luminal line is expressed in function of longitudinal distance (x -axis). The *dashed lines* represent the linear regression lines to the base and to the apex of four bending points. The *squares* indicate downward pressure points at the basilar membrane, the *circles* stand for pressure against the floor of the scala tympani.

Results

Figure 4 shows the elevation of the central luminal path as a function of the longitudinal distance from the round window as measured in the 8 different datasets. Overall, it is clear that the steepness of the cochlear spiral was not continuous. Taking the plot of the first data set as an example a gradual downward slope was evident within the first 5 mm from the round window. Visual assessment of the 3D microCT dataset (figure 5) showed that this was correlated to the morphology of the proximal cochlear lumen which has a bulbous aspect and tapers rapidly within its first millimeters, causing a short rise followed by a decline. At the most inferior point of this decline linear regression analysis revealed a pressure point at the floor of the scala tympani. The path then continued in an upward slope until approximately 10mm from the round window. At this point, another but less pronounced descent of the slope was observed. Further along the path, at approximately 15mm from the round window a sudden increase in elevation was detected, corresponding to the visually observed steep slope at the junction between the first and the second turn and towards the apex.

Certain similarities in the shape and pattern of the central luminal paths in 8 different bones, as shown in Figure 4, strongly suggest that these potential pressure points occur more frequently at certain specific points along the cochlear lumen. Figure 6 shows the occurrence of bending points on the floor of the scala tympani (A and C) and at the basilar membrane (B and D), measured as frequency within bins of 45 degrees. For the latter, 6 out of 8 bones revealed 1 downward bending point at 180 to 225 degrees, corresponding to a surgical insertion depth of approximately 12 to 14mm. Of the remaining two bones, one showed a bending point at 170 degrees, and the other showed no pressure point in this vicinity.

In half of the bones, a second area of pressure points towards the basilar membrane was seen in the very apex (at the level of 725 degrees or 22-26mm). Several upward bending points occurred at the proximal cochlear canal (0-90 degrees) in all 8 bones. A single bending point per bin was found at 225-270 degrees in 6 cochleae and another one at 405 to 450 degrees in 5 datasets.

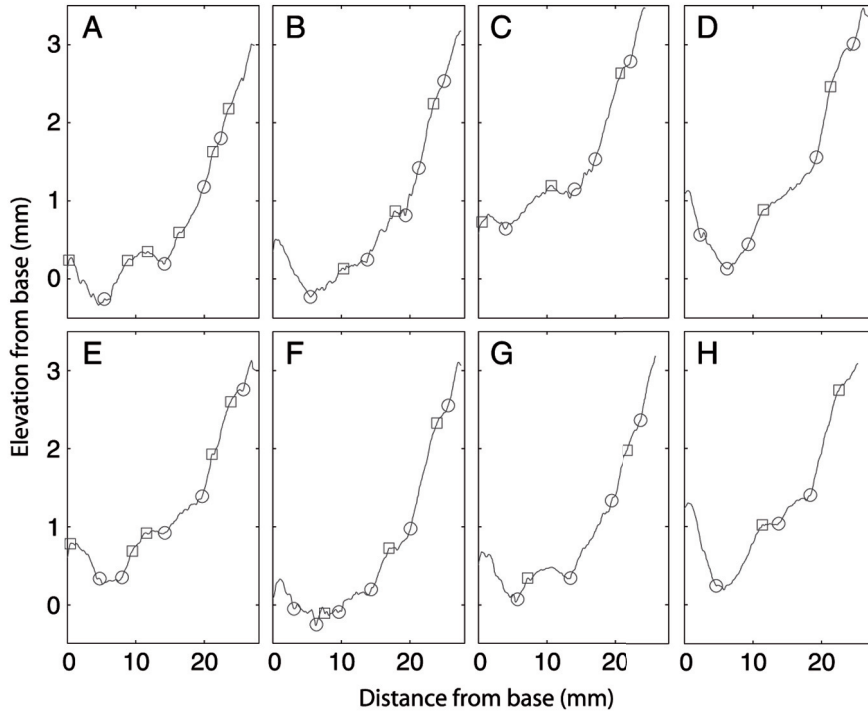


Figure 4. The z -coordinates of the central luminal path along the cochlea in mm are shown in 8 different micro CT datasets. In all temporal bones a similar pattern of a proximal short rising and descending slope, followed by a rising path with changes in steepness along its course is seen.

One bone showed a pressure point at the upper edge of this interval; in two other bones, no pressure point was discerned in or around this interval.

The finding that multiple temporal bones consistently exhibit a bending point at specific angular bins (180-225, 225-70 and 405-450 degrees) turned out to be highly statistically significant (with $p < 0.00001$). The details of the statistical analysis are shown on the Otology and Neurotology resource webpage (Supplemental Digital Content 1). This statistical finding on the distribution of areas of increased pressure along the BM and ST confirms the visual impression on the graphs in Figure 4.

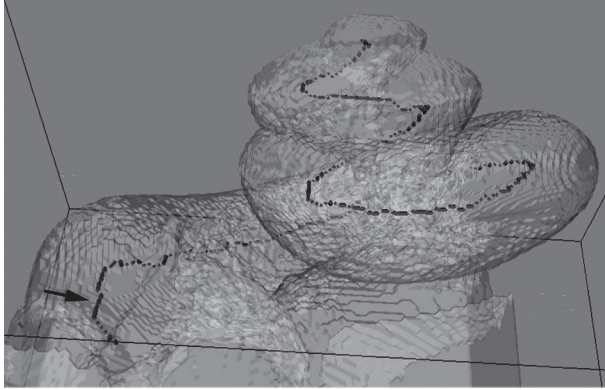


Figure 5. Semitransparent 3-D segmentation of the cochlear duct: the central luminal line is shown (arrow). In the most proximal bulbous part of the cochlear duct the path shows a short rise followed by a downward slope until the cochlear duct tapers. On its further course a decline is seen in the second half of the first turn. On the junction with the second a steep slope is seen, which flattens again in the second turn.

Discussion

Insertion trauma during cochlear implantation is an important and extensively studied complication because of its potential impact on the short term as well as for long-term speech performance. Insertion trauma is repeatedly reported to occur at three specific locations: at the base of the basal turn of the cochlea, [5,6] at approximately 180 degrees [7-10] and in deep insertions over 400 degrees. [11-13] This corresponds well with the findings of bending points and therefore potential pressure points along the cochlear spiral reported in this study. The assumption is made that the course of the basilar membrane follows the course of the cochlear lumen. This approach was taken because future clinical application in CT scans will also be at the level of the total cochlear lumen, as the basilar membrane cannot be discerned at those images. Detailed analysis of our data in regard to the position of the BM in relation to the central path has been performed based on the diameter of the scala tympani as part of a study where clinical CT and micro-CT data are compared in detail and will be reported separately. It confirmed a rapid decrease of dimensions in the proximal basal turn as reported by Hatsushika et al. [19] In agreement with findings of Skinner et al. [25] who showed a

close relationship between the centroid line and the basilar membrane, only minimal fluctuations of the BM in relation to the central path were seen. At the level of highest risk for insertion trauma (180-500 degrees) the fluctuations do not exceed 10% of the total diameter of the ST.

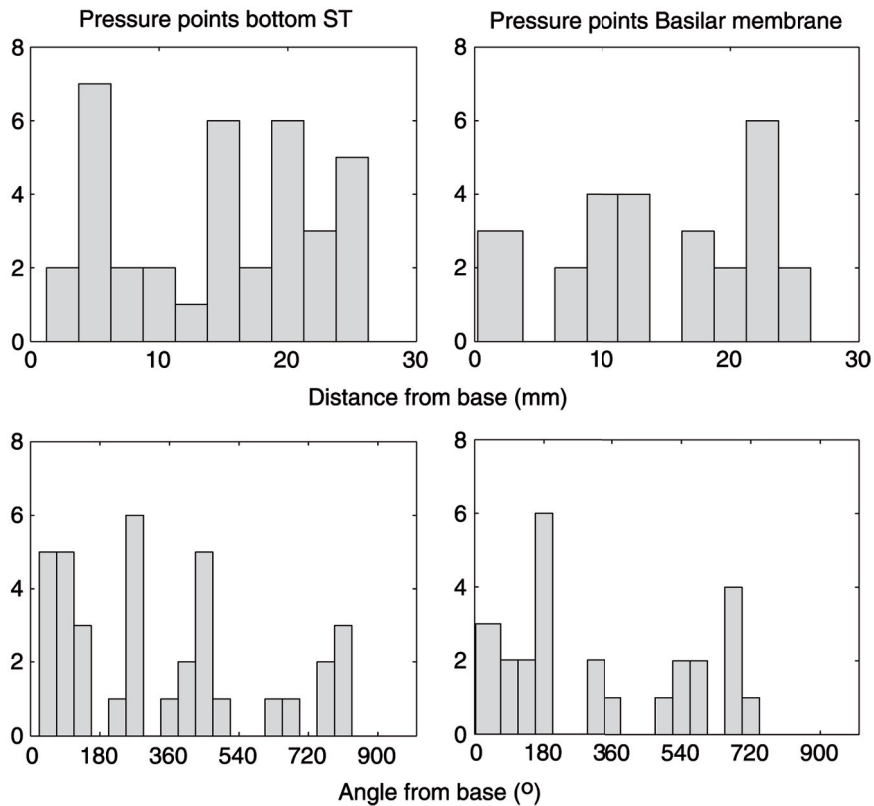


Figure 6. Histograms of the occurrence of pressure points at the floor of the scala tympani and the basilar membrane: the changes in z along the cochlea as a function of length of the center path were used to calculate the histograms for both distance from round window and angle. The angular bins had a width of 45 degrees.

In agreement with those of previous reports, our data show a short rise followed by a downward slope of the central luminal line at the most proximal part of the basal turn,

following the intrinsic morphological features of the proximal cochlear lumen. As shown in Figure 5, this part of the cochlea has a bulbous appearance, followed by tapering of the lumen. This tapering is mainly induced by a downward slope of the upper part of the cochlear lumen and will cause the central luminal line to descend. Therefore, an inserted electrode array is likely to encounter a pressure point at the basilar membrane and to a lesser extent to the floor of the scala tympani. Modifications of the surgical approach have been proposed to decrease the risk for trauma: [6,14] creating a cochleostomy by removal of the floor of the niche, combined with a superior-to-inferior insertion angle has been favored over an anterior cochleostomy. By the inferior approach and downward pointing the electrode array is directed in line with the longitudinal axis of the cochlea and avoids damaging the basilar membrane at the short descending slope in the proximal cochlea. Huttenbrinck et al. [5] reported that damage at the base is more likely to occur after forced deep insertion. It seems likely that in this case the increased strain to the pressure point at the floor of the scala tympani puckers up and pushes the electrode array upward through the fragile basilar membrane.

Within the second half of the basal turn a pressure point at the basilar membrane is found at 180 to 225 degrees or 12 to 14 mm shortly thereafter, followed by a pressure point to the floor of the scala tympani. Most likely, the implant will follow its straight course along this short dip with the risk of piercing the basilar membrane. This has been reported more often for implants with small-sized electrode carriers than for large sized ones. [8-10] If the array passes this region without damaging the basilar membrane the electrode array presumably contacts the floor of the scala tympani which is more resistant to trauma. It is not clear whether the increased vertical stiffness present in some electrodes prevents upward motion at this point or if it increases the risk for basilar membrane trauma just before this point at 180 to 225 degrees.

At the junction between the second and apical turn an increase in steepness of the spiraling cochlear canal is seen, resulting in pressure points on the floor of the scala tympani at the level of 405 to 450 degrees or at 18- to 22-mm distance from the round window. In surgical reports it is often described that a resistance is felt during insertion within the first turn of the cochlea at approximately 17 to 21 mm. [26,27] Insertion trauma at this level has been ascribed to the decrease in size of the scala tympani and the concomitant mismatch of the electrode array. However in the human scala tympani a plateau [17] or even increase in height of the scala tympani [16,18,19] has been found at the junction between basal and middle turn of the cochlea. Therefore to us it seems

likely that not only the actual size of the scala tympani but also its course within a 3-D environment might be an underlying factor for insertion trauma in cochlear implantation at this level.

These findings may have implications to future electrode designs. The downward slope within the second half of the basal turn and the changes of steepness along the cochlear spiral question the advantages of vertical stiffness within the electrode tip. Possibly a long and soft tip would be more appropriate to follow the cochlear slopes. It seems plausible that arrays with smaller electrodes would pass the regions of pressure points more easily.

Evaluation of cochlear trauma in patients has been assessed by fusion of clinical imaging datasets to a single template unimplanted ear scanned with micro computed tomography and orthogonal-plane fluorescence optical sectioning microscopy. The latter was used to determine the midmodiolar axis (z-axis in the 3-D cochlear coordinate system). [20]

Our results however show individual differences of cochlear morphology in the 8 specimens. This indicates that the z-coordinate should be applied individually to achieve accurate estimations of basilar membrane trauma.

Conclusion

Insertion trauma due to cochlear implantation has repeatedly been reported to occur at the base, at approximately 180 degrees and in deep insertions of more than 400 degrees. Our data favor the idea that the intrinsic cochlear morphology with its non-continuous spiraling path contributes to the risk for trauma at these specific locations. To determine the exact position of a cochlear implant within its 3-D environment, an individually appointed z-coordinate has to be applied before accurate estimations of BM perforation can be made on the basis of pre- and post-operative multislice CT scans.

Reference List

1. Leake PA, Hradek GT, Snyder RL. Chronic electrical stimulation by a cochlear implant promotes survival of spiral ganglion neurons after neonatal deafness. *J Comp Neurol* 1999;412:543-562
2. Rebscher SJ, Snyder RL, Leake PA. The effect of electrode configuration and duration of deafness on threshold and selectivity of responses to intracochlear electrical stimulation. *J Acoust Soc Am* 2001;109:2035-2048
3. Adunka O, Kiefer J. Impact of electrode insertion depth on intracochlear trauma. *Otolaryngol Head Neck Surg* 2006;135:374-382
4. Saitoh M, Ueda H, Yanagita N. Changes in cochlear function after double-membrane rupture in the guinea pig. *Hear Res* 1997;104:147-154
5. Huttenbrink KB, Zahnert T, Jolly C, Hofmann G. Movements of cochlear implant electrodes inside the cochlea during insertion: An X-ray Microscopy study. *Otol Neurotol* 2002;23:187-191
6. Oleary MJ, House WF, Fayad J, Linthicum FH. Electrode Insertion Trauma in Cochlear Implantation. *Ann Otol Rhinol Laryngol* 1991;100:695-699
7. Nadol JB, Shiao JY, Burgess BJ, et al. Histopathology of cochlear implants in humans. *Ann Otol Rhinol Laryngol* 2001;110:883-891
8. Richter B, Aschendorff A, Lohnstein P, Husstedt H, Nagursky H, Laszig R. The Nucleus Contour electrode array: A radiological and histological study. *Laryngoscope* 2001;111:508-514
9. Wardrop P, Whinney D, Rebscher SJ, Roland JT, Luxford W, Leake PA. A temporal bone study of insertion trauma and intracochlear position of cochlear implant electrodes. I: comparison of Nucleus banded and Nucleus Contour (TM) electrodes. *Hear Res* 2005;203:54-67
10. Tykocinski M, Saunders E, Cohen LT, et al. The Contour electrode array: Safety study and initial patient trials of a new perimodiolar design. *Otol Neurotol* 2001;22:33-41
11. Wardrop P, Whinney D, Rebscher SJ, Luxford W, Leake P. A temporal bone study of insertion trauma and intracochlear position of cochlear implant electrodes. II: Comparison of Spiral Clarion (TM) and HiFocus II (TM) electrodes. *Hear Res* 2005;203:68-79
12. Aschendorff A, Klenzner T, Richter B, Kubalek R, Nagursky H, Laszig R. Evaluation of the HiFocus (R) electrode array with positioner in human temporal bones. *J Laryngol Otol* 2003;117:527-531
13. Eshraghi AA, Yang NW, Balkany TJ. Comparative study of cochlear damage with three perimodiolar electrode designs. *Laryngoscope* 2003;113:415-419
14. Briggs RJS, Tykocinski M, Stidham K, Roberson JB. Cochleostomy site: Implications for electrode placement and hearing preservation. *Acta Otolaryngol* 2005;125:870-876
15. Adunka OF, Pillsbury HC, Kiefer J. Combining perimodiolar electrode placement and atraumatic insertion properties in cochlear implantation - fact or fantasy? *Acta Otolaryngol* 2006;126:475-482
16. Zrunek M, Lischka M, Hochmairdesoyer I, Burian K. Dimensions of the Scala Tympani in Relation to the Diameters of Multichannel Electrodes. *Arch Otorhinolaryngol* 1980;229:159-165
17. Wysocki J. Dimensions of the human vestibular and tympanic scalae. *Hear Res* 1999;135:39-46
18. Walby AP. Scala Tympani Measurement. *Ann Otol Rhinol Laryngol* 1985;94:393-397

19. Hatsushika S, Shepherd RK, Tong YC, Clark GM, Funasaka S. Dimensions of the Scala Tympani in the Human and Cat with Reference to Cochlear Implants. *Ann Otol Rhinol Laryngol* 1990;99:871-876
20. Skinner MW, Holden TA, Whiting BR, et al. In vivo estimates of the position of advanced bionics electrode arrays in the human cochlea. *Ann Otol Rhinol Laryngol Suppl* 2007;197:2-24
21. Tschirren J, Palagyi K, Reinhardt J, Hoffman E, Sonka M. Segmentation, skeletonization, and branchpoint matching - a fully automated quantitative evaluation of human intrathoracic airway trees. Vol. LNCS 2489, Tokyo, Japan: Medical Image Computing and Computer-Assisted Intervention (MICCAI 2002) 2002.
22. Tran S, Shih L. Efficient 3d binary image skeletonization. *Proceedings of IEEE Computational Systems Bioinformatics Conference Workshop (CSBW 2005) 2005*: 364-372.
23. Yang Y, Zhu L, Haker S, Tannenbaum AR, Giddens DP. Harmonic skeleton guided evaluation of stenoses in human coronary arteries. *Med Image Comput Comput Assist Interv Int Conf Med Image Comput Comput Assist Interv 2005*;8:490-497
24. Marquering HA, Dijkstra J, de Koning PJH, Stoel BC, Reiber JHC. Towards quantitative analysis of coronary CTA. *Int J Cardiovasc Imaging* 2005;21:73-84
25. Skinner MW, Ketten DR, Holden LK, et al. CT-derived estimation of cochlear morphology and electrode array position in relation to word recognition in nucleus-22 recipients. *JARO* 2002;3:332-350
26. Gstoettner W, Plenk H, Franz P, et al. Cochlear implant deep electrode insertion: Extent of insertional trauma. *Acta Otolaryngol* 1997;117:274-277
27. Kennedy DW. Multichannel Intracochlear Electrodes - Mechanism of Insertion Trauma. *Laryngoscope* 1987;97:42-49

9

Cochlear Morphometry based on 3-dimensional Image Exploration: a MicroCT-MSCT study

BM Verbist, L Ferrarini, JJ Briaire, F Vanpoucke, F Admiraal-Behloul,
H Olofsen, JHC Reiber, JHM Frijns

Abstract

Hypothesis: The goal of this study was to develop an easily applicable method for direct 3D measurements of the cochlear dimensions, both longitudinal and cross-sectional, given a set of micro CT and clinical multidetector row CT (MSCT) images. Such a technique would be a valuable addition to cochlear implant (CI) candidate pre-operative evaluation.

Background: Estimations of cochlear length are of interest when planning CI surgery. Length measurements can influence the choice of a particular electrode array, cochleostomy location and insertion depth, and cross-sectional measurements are important to prevent insertion trauma. In addition to surgical planning, the dimensional information can be helpful during post-operative fitting of the device, as the frequency band assignment in the CI can then be adjusted based on knowledge of the natural tonotopy of the ear, which is dependent on the cochlear length and the electrode locations.

Methods: Eight isolated human temporal bones were scanned by microCT and multidetector row CT. An image processing technique was developed that is able to extract length and diameter measurements using an automatic segmentation approach. This technique was applied to the microCT and MSCT data sets. To validate the reliability of the image processing algorithm, the outcomes were compared to manual contouring measurements in microCT.

Conclusion: Good estimations of cochlear dimensions can be obtained in MSCT datasets of isolated human temporal bones by automatic segmentation.

Introduction

The study of cochlear morphology is of great interest in cochlear implant (CI) research. In recent years investigations have highlighted the variability in outcomes in terms of speech perception, [1] improvement of sound and music perception [2] and the development of electric acoustic stimulation (EAS) for patients with residual low frequency hearing. [3] New electrode designs and modifications of surgical technique and speech processing strategies have contributed to improvement in these outcomes.

Based on animal studies [4,5] trauma to the cochlea during implant electrode insertion is thought to cause degeneration of spiral ganglion cells, leading to deterioration of (residual) hearing. Since there is evidence that intracochlear trauma increases with deep insertions [6] preoperative information about the individual length and diameter of the scala tympani would be helpful in estimating the optimal insertion depth and precise knowledge of the cochlear size could potentially minimize insertion trauma. This information could help the surgeon in selecting the optimal electrode design for a specific patient, with regard to the diameter and length of the electrode array.

Another factor that might influence speech perception outcomes is appropriate matching of the longitudinal distribution of frequency bands along the electrode array with the positions of “characteristic frequencies” along the cochlea. Greenwood characterized the physiological tonotopic organization of the basilar membrane mathematically and concluded that frequency distribution could be predicted from the length for any individual cochlea. [7,8] This formula has become a commonly accepted method for estimation of characteristic frequency-versus-length relationships in cochlear implantation. The Greenwood function implies that for a particular characteristic frequency the distance from the round window is a proportion of the total cochlear length along the basilar membrane. As there are individual differences in cochlear length, patient-specific knowledge about the cochlear morphology could be beneficial.

For many years, variability in cochlear dimensions could only be studied using *post mortem* histological methods. In these studies several techniques have been used to estimate the cochlear dimensions, i.e. 2D reconstruction (measuring marked points in one plane), the surface specimen technique evaluating the inner ear directly under a microscope, and 3D reconstruction techniques [9-11] allowing measurements regardless of the angle at which the specimen was cut. Possible sources for error with these techniques are under-estimations of the length due to the cutting or viewing angle

and damage or shrinkage during the histological processing. This results in differences in length of about 13% between 2D reconstruction and 3D reconstruction techniques and approximately 5% between surface specimen technique and 3D reconstruction techniques.

Estimation of the 3D cochlear morphology *in vivo*, however, still remains a challenging task. Ketten, Skinner and co-workers [12,13] were the first to perform measurements in spiral CT images of human subjects. Using experimental software, they reconstructed CT-images to create sub-millimetre resolution images with 100 μm isotropic voxels. Their method for estimating cochlear length was based on fitting a mathematical function (Archimedian spiral) onto 2D CT mid-modiolar images. The principal assumption made in this approach is that the cochlear spiral has a common configuration, whereas the spiral length is individual-specific. The cochlear length was defined as the length of the centroid of the cochlear canal bony margins from the beginning of the first turn. The hook region was measured directly and added to the distance. Cochlear diameter was taken as the distance from the modiolus to the centroid line and the axial height was defined as the modiolar axis length.

Escudé and co-workers developed an indirect method of estimating the cochlear size. [14] Since for the Archimedian spiral, the radius of curvature is related to the overall length of the spiral, [12,15] they investigated the possibility that the length of the cochlea could be predicted by measuring the maximum diameter of the basal turn at the round window. Their histological studies confirmed that this basal diameter shows a significant correlation with the length of the Organ of Corti (OC) and the spiral ganglion (SG). [11]

Our goal was to develop an easily applicable method for direct 3D measurements of the cochlea in clinical multidetector row CT (MSCT) images obtained as part of the pre-operative assessment of cochlear implant candidates. To avoid time consuming manual measurements we chose to use an automatic approach based on state-of-the-art image processing algorithms. The length metric does not rely on a mathematical function fit. It is non-parametric, and therefore potentially more accurate, as the path tracing technique can account for geometries that deviate from a mathematical spiral. Both length of the cochlear lumen and diameter of the scala tympani can be included in the analysis.

As this metric is different from that used in previous studies, and the resolution of clinical CT imaging is limited, we validated the new method on isolated temporal bones by comparing the findings using clinical CT with those using microCT. MicroCT is a relatively new *in vitro* technique which can provide high resolution imaging of the

endocochlear soft tissue structures without affecting the integrity of the temporal bone. [16]

Materials & Methods

Materials

Cylindrical blocks of 8 adult human temporal bones containing the cochlea were prelevated and stained/fixed in formalin. The specimens were scanned using microCT (Skyscan-1076, Aartselaar, Belgium) and multidetector row computer tomography (MSCT) (Aquilion-64, Toshiba Medical Systems, Otawara, Japan). MicroCT rendered isotropic datasets with a voxel-size of 17 μm . The high resolution allows visualization of the scala tympani and scala vestibuli, the osseous spiral lamina, the basilar membrane and the spiral ligament, though Reissner's membrane, separating the scala media from the scala vestibuli, is not consistently seen. MSCT was performed with clinical scan parameters as listed in Table 1. [17]

Table 1. MSCT scan and reconstruction parameters

Acquisition parameters	
Tube voltage	120 kV
Tube current	200 mA
Rotation time	0.5s
Beam collimation	4X0.5 mm
Pitch factor	0.75
Scan Field of view	240 mm
Reconstruction parameters	
Slice thickness	0.5 mm
Reconstruction interval	0.1 mm
FOV	30 mm

Image processing

Automatic segmentation in MSCT and microCT

Automatic 3-dimensional segmentation of all datasets was obtained. To increase the computational efficiency of the automatic segmentation in microCT, the datasets were

sub-sampled to an isotropic resolution of 70 $\mu\text{m}/\text{voxel}$. The datasets were reconstructed along the plane of the basal turn of the cochlea (perpendicular to the modiolus), and imaged in 3 orthogonal planes. Using a 3D growing algorithm, all voxels belonging to the total cochlear spiral were extracted, a voxel within the cochlear lumen was chosen and all voxels with similar density were included in the segmentation. The result of such segmentation on one temporal bone is shown in Figure 1. Visual inspection of the segmented structure was performed by a head and neck radiologist. If voxels outside the cochlear lumen were included either the algorithm was re-applied on another voxel (with a slightly different density) or those voxels were manually removed.

Manual contouring in microCT

Manual contouring of the microCT datasets was performed as follows: The microCT datasets were rotated and aligned along the plane of the basal turn of the cochlea (perpendicular to the modiolus). With research software, at every 30 degrees, starting from the middle of the round window, radial 2D sections were made perpendicular to the lateral wall of the cochlea. In each of these sections contours of the bony labyrinth, scala tympani, scala vestibuli including scala media and Rosenthal's canal were drawn by a human expert. In addition, the medial and lateral end-points of the osseous spiral lamina and the tympanic, medial and vestibular end points of the spiral ligament were marked (figure 2). This analysis was successfully performed in all eight bones for the first 1.75 turns of the cochlea (up to 630°).

Cochlear morphometry

3D coordinate system

In order to perform measurements, a 3D coordinate system was introduced. The x - y plane was placed through the basal turn of the cochlea. The z -axis runs through the center of the modiolus. This is consistent with the 3-dimensional cylindrical coordinate system formulated by an international consensus panel. [18] The zero angle of the x -axis was chosen at the center of the cochlear lumen, at the level of the anterior margin of the round window. This is in accordance with the cochlear framework described by Skinner et al. [19] and as such the starting point could be placed in the center of the cochlear lumen.

Longitudinal measurements using micro CT and CT

In order to obtain length measurements in the automatically segmented datasets, skeletonization and wave propagation techniques were applied [20-23] to detect the spiraling central luminal line of the total cochlear lumen (i.e. bony labyrinth). A detailed description of this technique has been published separately. [24] Additionally, the lateral and medial wall lengths were determined. These measurements facilitate prediction of the position of a perimodiolar electrode array, designed to lie along the medial wall, or of a straight electrode design, usually positioned along the lateral wall.

The medial and lateral wall lengths were evaluated with two different techniques (figure 3). In method 1, the estimated cochlear radii at the medial and lateral wall were used to assess locations along the medial and lateral paths. To achieve this, small cylinders were fitted to the cochlea at certain points along the central path. By this, the radius could be obtained perpendicular to the medial and lateral walls as the maximal distance from left to right. This method may render slight underestimations of the true length. Therefore a second method was applied, in which locations along the paths were evaluated using the surface of the segmented lumen, reducing the risk of underestimation. For the central path, the starting and end points were manually identified at the x-axis (angle 0°) and at the apex of the cochlea respectively.

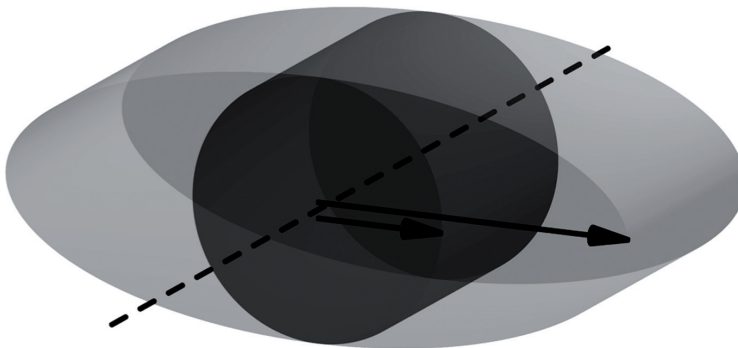


Figure 3. Length measurements of the medial and lateral wall of the cochlea with 2 different methods: in method 1 small cylinders were fitted to the cochlea at certain points along the central path. The medial and lateral paths were obtained at the maximal distance from the central luminal line, measured perpendicular to the medial and lateral walls (short arrow). This method may render slight underestimations of the true length. In the second method the locations along the paths were evaluated using the surface of the segmented lumen (long arrow).

Cross-sectional measurements using microCT and CT

Cross-sectional measurements were obtained in the automatically segmented datasets. The total diameter of the cochlear lumen was derived from the estimated radius evaluated by method 1 (as described above) using both microCT and CT. To obtain cross-sectional measurements of the scala tympani and vestibuli, the microCT datasets were re-sliced using the position and orientation of the center line: the spiral structure was straightened to a tubular structure, in which the scala tympani and scala vestibuli could be easily segmented with the same 3D growing algorithm used to extract the cochlear spiral (figure 4). Results were checked visually by an experienced head and neck radiologist. On each slice, perpendicular to the osseous spiral lamina and basilar membrane, circles were fitted to the cochlear lumen and the two scalae (figure 4b). The minimum radius of these circles was used as a measure of the diameters of the scala tympani and scala vestibuli respectively.

Based on this, the following were derived: (1) the ratio of the total diameter measured using CT and microCT and (2) the ratio between the diameter of the scala tympani and the total lumen of the cochlea from micro CT.

Results

Longitudinal measurements using micro CT and CT

Three-dimensional segmentation of the cochlear duct was successfully applied in all datasets.

For microCT the length of the central luminal path was $28.7 \text{ mm} \pm 3.3 \text{ SD}$ (range 25.0 - 35.1 mm). The lateral wall measured $42.0 \text{ mm} \pm 6.6 \text{ SD}$ (range 36.1 - 57.1 mm) using method 1 and $47.8 \text{ mm} \pm 6.3$ (range 42.3 - 60.6 mm) using method 2. The length of the medial wall measured with method 1 and 2 was $20.9 \text{ mm} \pm 4.2$ (range 18.0 - 30.3 mm) and $26.9 \text{ mm} \pm 3.7$ (range 23.0 - 33.2 mm), respectively. The cochlear height was found to range from 2.09 - 3.47 mm. In figure 5 and Table 2 the results of the manual contouring based analysis are reported. The cumulative length of the central path of the total cochlear lumen matches the length of the central path of the scala tympani. Both are slightly shorter than the length of the OC (figure 5). Measurements were obtained

up to 1.75 turns. These were used to validate the measurements by segmentation. To enable comparison of the two techniques, all distances obtained on the automatically segmented images were measured up to 630° and the results are shown in Table 2. The differences between longitudinal measurements in segmented microCT and MSCT datasets are graphically illustrated for each temporal bone and in average in figure 6. The deviation percentage was 2.7% of the total measured length for the central luminal path.

For the medial and lateral walls, the deviation percentages varied according to the applied method for path estimation (as described previously): for the medial wall, 21.8% (method 1), and 14.3% (method 2); for the lateral wall, -10.3% (method 1) and -10.5% (method 2). Given the considerable differences for lateral and medial path estimations further analysis was limited to central path measurements. In comparison to manual measurements on microCT, our method showed a mean difference of -0.30 mm (± 0.32 SD) for microCT and 0.31mm (± 0.80 SD) for CT. This corresponds to a bias of -1.37 % and 1.36% respectively.

Table 2. Results of longitudinal measurements (mean and SD) of the central luminal path (CP), medial and lateral wall, based on manual contouring of microCTs and on automatically segmented microCT and MSCT datasets up to 630°.

	Length CP (mm)	Length medial wall (mm)		Length lateral wall (mm)	
Manual microCT	23 (0.6)		15.8 (0.7)		31.4 (0.8)
		method 1	method 2	method 1	method 2
Segmented microCT	22.5 (0.6)	13.6 (0.7)	13.8 (0.7)	31.2 (0.7)	33.2 (1.0)
Segmented MSCT	23.1 (1.2)	17.3 (1.4)	16.0 (1.1)	28.7 (1.3)	30.1 (1.0)

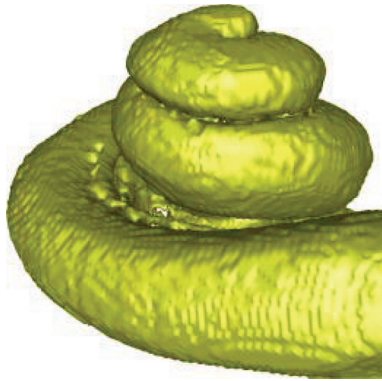


Figure 1. Automatic segmentation applied to a microCT: based on a 3D growing algorithm, in which one voxel within the cochlea is chosen and all neighboring voxels with similar intensity.

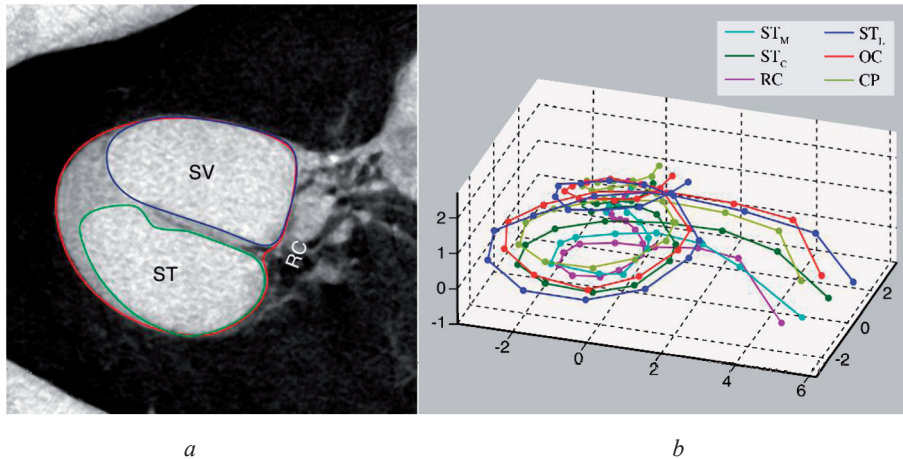


Figure 2. Manual segmentation of microCT datasets: on radial 2D sections contours of the bony labyrinth (red), scala tympani (green) and scala vestibuli (blue) were drawn and the endpoints of the osseous spiral lamina and spiral ligament were marked (a). Based on this a 3D reconstruction of the cochlea was made and length measurements of the cochlear canal (CP: central path), Organ of Corti (OC), Rosenthal's canal (RC) and scala tympani (ST_l : lateral, ST_c : central, ST_m : medial) were performed (b).

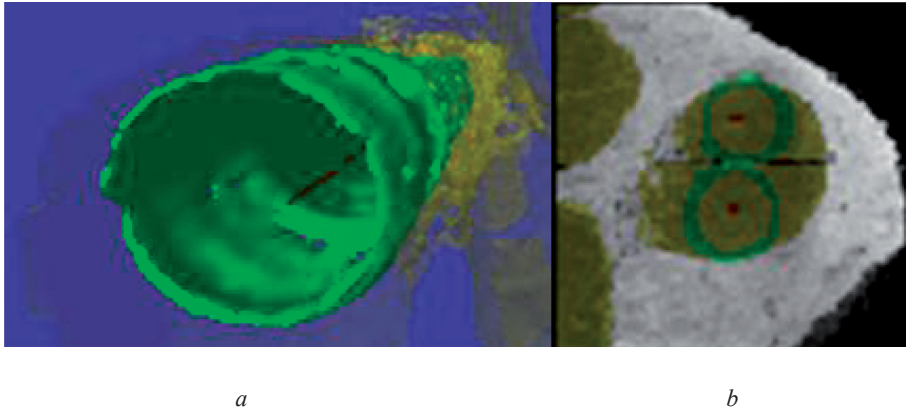


Figure 4. Cross-sectional measurements of the SV and ST: the microCT dataset was straightened to a tubular structure **(a)** and minimal diameters of the scalae where obtained by fitting small cylinders on the segmented scalae **(b)**.

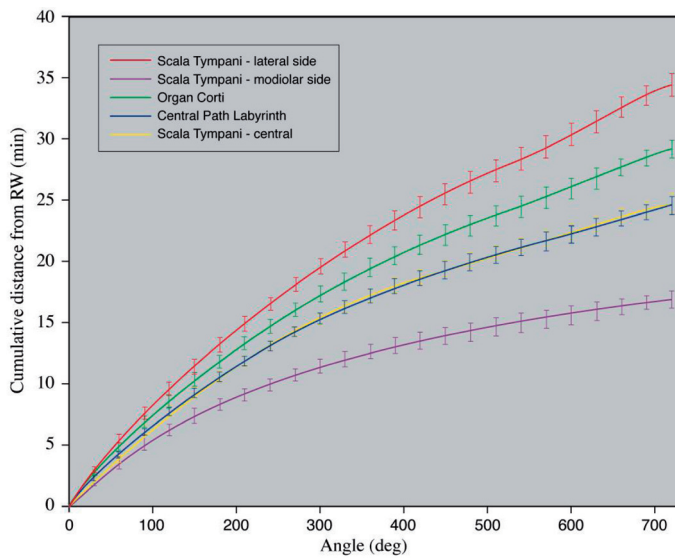


Figure 5. Results of longitudinal manual measurements on 8 microCT datasets: a close relationship between the central path of both the cochlea and the scala tympani and the Organ of Corti is seen.

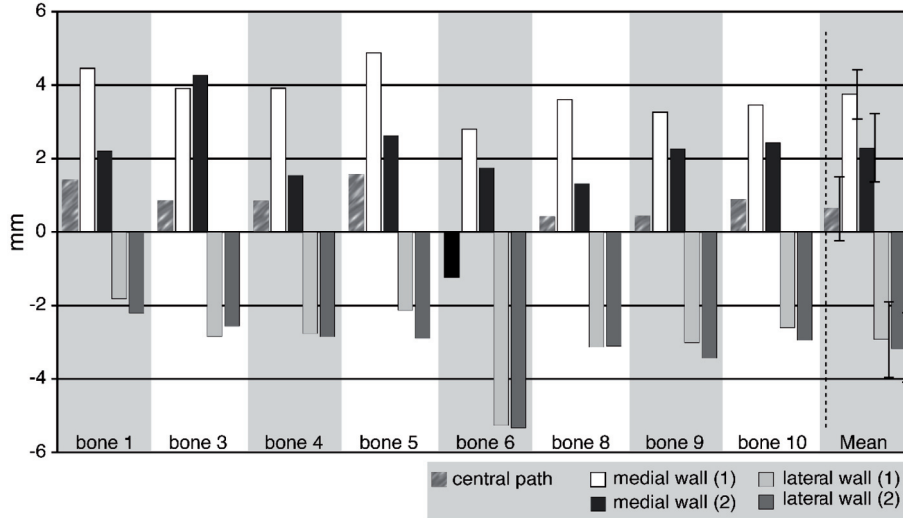


Figure 6. Differences between longitudinal measurements on segmented microCT and MSCT datasets are shown for each temporal bone (1,3,4,5,6,8,9,10) and on average. The results of longitudinal measurements of the central luminal path (CP), medial and lateral wall determined by the estimated radius (method 1) and based on the segmentation (method 2) in MSCT were compared to results from microCT. The difference is expressed in mm (x-axis).

Cross-sectional measurements using microCT and CT

The ratio between the total diameter of the cochlear canal measured with CT and microCT ranges from 0.56 – 0.79 in the basal turn (up to 360°) and reduces to 0.40 more distally, as shown in Figure 7.

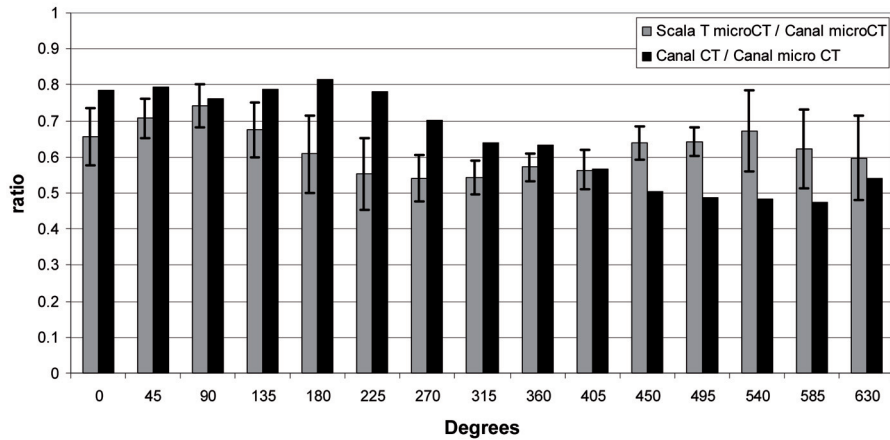


Figure 7. Cross-sectional measurement of the scala tympani: the ratios (0-1.0, x-axis) of the diameter of the scala tympani and the total diameter of the cochlea as measured on microCT (gray) and between the total diameters of the cochlear lumen on MSCT and microCT (black) are shown at intervals of 45° (y-axis). The underestimation of the size of the cochlear lumen is ascribed to lower spatial resolution and blurring and becomes most pronounced in the second turn of the cochlea. The ratio between the diameter of the scala tympani and the total diameter on microCT is relatively stable between 270° and 405°.

Discussion

Analysis of cochlear dimensions (*in vivo*) is hindered by the complex morphology and orientation of the inner ear within the temporal bone and its small dimensions. Furthermore, endocochlear anatomy cannot be visualized in clinical temporal bone imaging. We propose a new method to estimate dimensions of the cochlear spiral and obtain longitudinal and cross-sectional measurements using MSCT. Such measurements would be a valuable addition to preoperative assessment of cochlear implant candidates for individually optimizing the insertion depth and array selection of cochlear implants and possibly also for adjusting cochlear implant mapping.

The results of the measurements from the microCT data confirm the inter-individual differences in cochlear lengths described in the literature and range from 24 - 40.1mm. [9,11-13,25-27]

The ratio between the dimension of the scala tympani and the total cochlear lumen as measured on micro-CT ranges from 0.54 - 0.74 and shows an undulating course with a slight increase and decrease within the first 270°, a relatively constant value up to 405° and again a small increase and decrease between 450 - 630°.

Generally, these cochlear lengths refer to OC lengths. Since the fine intracochlear structures cannot be discerned in clinically used CT scanners, we chose to measure the length along the central luminal line. Skinner [13] has reported that the centroid line falls near the junction of the basilar membrane and osseous spiral lamina and is therefore near, but slightly medial to, the pillar cell mark conventionally used in histological studies. Our findings based on manual contouring of endocochlear structures also illustrate a close relationship and a slightly shorter distance of the centroid line in comparison to the OC (figure 5). The central luminal path measurement therefore represents a useful tool for estimating a patient's cochlear size and to compare these data to histological studies. The variability in lengths emphasizes the importance of such measurements for optimal preoperative planning of cochlear implantations. The optimal insertion depth could be individually estimated preoperatively. By this, performance may be improved and insertion trauma due to deep insertions may be prevented.

The proposed automatic segmentation technique for cochlear morphometry was validated using direct manual micro CT measurements. The high resolution volumetric data rendered by micro CT allows for practically artifact-free preparation and optimal reconstruction planes to obtain reliable measurements. The linear piecewise reconstruction could, however, lead to a subtle underestimation of the distance. Comparison of central luminal line measurements with our proposed method showed a bias of 1.4% in microCT and CT.

When comparing CT and micro CT data, the bias for length measurement increases markedly when looking at the medial or lateral wall of the cochlea. This is ascribed to the fact that given a slice thickness of 0.5 mm in MSCT reconstruction, slight inaccuracies in delineating the walls for segmentation produce a substantial error. Based on this, and the above described close relationship to the OC, we conclude that the central luminal line is, as yet, the better metric for characterizing cochlear length. Direct measurements of the medial and lateral wall length would require CT scans with higher spatial resolution.

In order to prevent insertion trauma, information about the size of the scala tympani could be invaluable. Currently, the basilar membrane cannot be visualized with clinical MSCT scanners. However, having a dataset of eight temporal bones, scanned both with

MSCT and microCT, a predictive measure was looked for. To evaluate whether prediction of the diameter of the scala tympani in patients would be possible, based on cross-sectional measurement of the cochlear lumen, the accuracy of MSCT measurements was compared with microCT. The inherent spatial resolution of the microCT scanner is much better compared to a clinical CT scanner, leading to less image blurring. Blurring results in a shift of the maximum of the signal intensity towards the center position of the canal, [28] which explains a noticeable underestimation of the canal diameter when it is determined from the human CT images. This underestimation becomes most pronounced in the second turn of the cochlea, and has to be taken into account when predicting the size of the scala tympani based on MSCT scans.

Looking at the relationship between the diameter of the scala tympani and the total diameter of the cochlear canal on microCT a variable course is seen along the analyzed proximal 1.75 turns. However, this ratio becomes relatively stable in the second half of the basal turn up to 405°. Thus, based on these results it seems likely that estimations of the size of the scala tympani can be made using CT by measuring the total diameter of the cochlear canal within the second half of the basal turn, provided a correction factor for the underestimation of the total diameter by MSCT is applied: the size of the scala tympani is approximately 0.8 times the total diameter as measured with CT.

The dimensions of the scala tympani will influence both the choice of implant and the operative technique. In patients with small scala tympani, either a short implant or one with small electrode contacts should be used. Furthermore, the surgical approach in such cases might favour a direct round window insertion over a cochleostomy.

This study has shown that non-parametric length measurements of the cochlea can be obtained from clinical MSCT datasets and that the size of the scala tympani can thereby be estimated. These results are promising in regard to inter-individual tailoring of the choice of cochlear implant devices and operative technique based on preoperative CT imaging. Further studies will be undertaken to establish the applicability of this technique *in vivo*.

Conclusions

An automatic method for measurement of cochlear dimensions, including length of the cochlear spiral, is presented, which is applicable to MSCT datasets from isolated

temporal bones. Validation of this method using microCT confirmed accurate estimations of the cochlear dimensions. Comparison to micro CT data shows that cross-sectional measurements of the second half of the basal turn of the cochlea appear to be predictive of the size of the scala tympani. The possibility of preoperatively determining individual cochlear dimensions is potentially helpful in planning cochlear implantation regarding the choice of a particular implant and operative technique, estimation of the optimal insertion depth and prevention of insertion trauma.

Reference list

1. Finley CC, Holden TA, Holden LK, et al. Role of electrode placement as a contributor to variability in cochlear implant outcomes. *Otol Neurotol* 2008;29:920-928
2. McDermott HJ. Music perception with cochlear implants: a review. *Trends Amplif* 2004;8:49-82
3. Turner CW, Reiss LA, Gantz BJ. Combined acoustic and electric hearing: preserving residual acoustic hearing. *Hear Res* 2008;242:164-171
4. Leake PA, Hradek GT, Snyder RL. Chronic electrical stimulation by a cochlear implant promotes survival of spiral ganglion neurons after neonatal deafness. *J Comp Neurol* 1999;412:543-562
5. Rebscher SJ, Snyder RL, Leake PA. The effect of electrode configuration and duration of deafness on threshold and selectivity of responses to intracochlear electrical stimulation. *J Acoust Soc Am* 2001;109:2035-2048
6. Adunka O, Kiefer J. Impact of electrode insertion depth on intracochlear trauma. *Otolaryngol Head Neck Surg* 2006;135:374-382
7. Greenwood D. Critical Bandwidth and Frequency Coordinates of Basilar Membrane. *J Acoust Soc Am* 1961;33:1344-1356
8. Greenwood DD. Critical bandwidth and consonance in relation to cochlear frequency-position coordinates. *Hear Res* 1991;54:164-208
9. Kawano A, Seldon HL, Clark GM. Computer-aided three-dimensional reconstruction in human cochlear maps: Measurement of the lengths of organ of Corti, outer wall, inner wall, and Rosenthal's canal. *Ann Otol Rhinol Laryngol* 1996;105:701-709
10. Takagi AF, Sando I. - Computer-aided three-dimensional reconstruction and measurement of the vestibular end-organs. - *Otolaryngol Head Neck Surg* 1988 Mar;98:195-202
11. Stakhovskaya O, Sridhar D, Bonham BH, Leake PA. Frequency map for the human cochlear spiral ganglion: implications for cochlear implants. *J Assoc Res Otolaryngol* 2007;8:220-233
12. Ketten DR, Vannier MW, Skinner MW, Gates GA, Wang G, Neely JG. In vivo measures of cochlear length and insertion depth of nucleus cochlear implant electrode arrays. *Ann Otol Rhinol Laryngol* 1998;107:1-16
13. Skinner MW, Ketten DR, Holden LK, et al. CT-derived estimation of cochlear morphology and electrode array position in relation to word recognition in nucleus-22 recipients. *JARO* 2002;3:332-350
14. Escudé B, James C, Deguine O, Cochard N, Eter E, Fraysse B. The size of the cochlea and predictions of insertion depth angles for cochlear implant electrodes. *Audiol Neurootol* 2006;11 Suppl 1:27-33
15. Yoo SK, Wang G, Rubinstein JT, Vannier MW. Three-dimensional geometric modeling of the cochlea using helico-spiral approximation. *IEEE Transactions on Biomedical Engineering* 2000;47:1392-1402
16. Postnov A, Zarowski A, De Clerck N, et al. High resolution micro-CT scanning as an innovatory tool for evaluation of the surgical positioning of cochlear implant electrodes. *Acta Otolaryngologica* 2006;126:467-474

17. Verbist BM, Frijns JHM, Geleijns J, van Buchem MA. Multisection CT as a valuable tool in the postoperative assessment of cochlear implant patients. *AJNR Am J Neuroradiol* 2005;26:424-429
18. Verbist BM, Skinner MW, Cohen LT, et al. Consensus panel on a cochlear coordinate system applicable in histological, physiological and radiological studies of the human cochlea. *Otology Neurotol: in press*
19. Skinner MW, Holden TA, Whiting BR, et al. In vivo estimates of the position of advanced bionics electrode arrays in the human cochlea. *Ann Otol Rhinol Laryngol Suppl* 2007;197:2-24
20. J.Tschirren, Palágyi K, Reinhardt J et al. Segmentation, skeletonization, and branchpoint matching - a fully automated quantitative evaluation of human intrathoracic airway trees. In : Goos G, Hatmanis J, van Leeuwen J, editors. *Medical Image Computing and Computer-Assisted Intervention (MICCAI'02)*, Srpinger, Berlin (Heidelberg), vol Vol. LNCS 2489, Tokyo, Japan; 2002: 12-19.
21. Tran S, Shih L. Efficient 3d binary image skeletonization. 364-372. 2005.In: *Proceedings of IEEE Computational Systems Bioinformatics Conference Workshop (CSBW'05)*. Washington: IEEE Computer Society Press; 2005: 364-372
22. Yang Y, Zhu L, Haker S, Tannenbaum AR, Giddens DP. Harmonic skeleton guided evaluation of stenoses in human coronary arteries. In: Duncan JS, Haker S, Gerig G, editors. *Med Image Comput Assist Interv Int Conf Med Image Comput Assist Interv (MICCAI'05)*, Palm springs, California, Vol LCNS 3749, Springer-Verlag Heidelberg 2005;8:490-497
23. Marquering HA, Dijkstra J, de Koning PJH, Stoel BC, Reiber JHC. Towards quantitative analysis of coronary CTA. *Int J Cardiovasc Imaging* 2005;21:73-84
24. Verbist BM, Ferrarini L, Briaire JJ, et al. Anatomic considerations of cochlear morphology and its implications for insertion trauma in cochlear implant surgery. *Otol Neurotol* 2009 Jun;30(4):471-7
25. Ulehlova L, Voldrich L, Janisch R. Correlative study of sensory cell density and cochlear length in humans. *Hear Res* 1987;28:149-151
26. Wright A, Davis A, Bredberg G, Ulehlova L, Spencer H. Hair cell distributions in the normal human cochlea. *Acta Otolaryngol Suppl* 1987;444:1-48
27. Bredberg G. Cellular pattern and nerve supply of the human organ of Corti. *Acta Otolaryngol* 1968;Suppl 236: 1-135
28. Marquering HA, Stoel BC, Dijkstra J, et al. CT blurring induced bias of quantitative in-stent restenosis anlyses. *Proceedings of SPIE Vol 6913 Medical Imaging 2008; conference 6913: Physics of Medical Imaging: 6913-54*

10

Concluding remarks and future perspectives in regard to imaging

Concluding Remarks

The remarkable progress of cochlear implants over the last decades has widely broadened their application. This put higher demands to all people involved in the selection, treatment and rehabilitation of cochlear implant candidates. Just like the development of implants resulted from interplay between physicists and surgeons, scientists and health care providers, the further directions in cochlear implant research and patient care need to be driven by multidisciplinary insights/groups. To enable and encourage such interdisciplinary cooperation a common ground for clear and easy exchange of findings in scientific and clinical studies is mandatory. Consensus meetings and thoughtful deliberations with representatives from different fields helped to crystallize such a common cochlear framework, which was presented in this thesis.

Radiologists may contribute to these further developments as well as to individualized patient care. This thesis focused on the potential of multislice computer tomography for detailed in vivo assessment of both the postoperative condition and preoperative cochlear morphology. The choice for this widely available imaging tool will hopefully enhance the awareness amongst radiologist about their role in the evaluation of cochlear implantees. It bears the possibility to open the door to multicenter studies on large patient groups. However as shown in this thesis current scanners have still shortcomings regarding cochlear imaging. Although scanner resolution has amazingly increased with the last generation CTs, mainstream of medical imaging exploits new technical developments for scanning faster and larger volumes, rather than visualizing small structures in greater detail. To accurately investigate cochlear trauma or to visualize cochlear implants with small electrode contacts and narrow inter-contact distances improved scanner resolution or other imaging techniques will be required. Moreover, modifications of scanner software may become necessary to enable display of metallic electrode contacts and tissues with large differences in density.

Future perspectives in regard to imaging

One of the major remaining challenges with cochlear implantation is to grasp the underlying causes for the large range of outcomes. Patients with similar demographics, medical history, type of cochlear implant and speech encoding strategy may show very

different speech perception scores. In post mortem studies it has been shown that the number of remaining ganglion cells has no relationship or a negative correlation to performance, indicating that performance variability cannot be explained on the basis of cochlear neuronal survival. [1,2] These findings and the fact, that the crude signal that is delivered by a limited number of channels of a cochlear implant can still be perceived as a meaningful auditory perception, gives rise to the supposition that processing the electrical/auditory input at a higher level in the auditory system is a main determinant for the final outcome. Several studies, in congenitally and prelingually deafened persons as well as in adults with later acquired deafness have indeed pointed to a reorganization of the auditory cortex during long lasting auditory deprivation. [3,4] This has been ascribed to the plasticity of the brain leading to colonization of the secondary/associative auditory cortex – normally used for auditory processing and language – by other sensory modalities. It implies that, although the auditory pathway to the primary auditory cortex remains functional, the incoming signals cannot be processed to meaningful sound in the higher order speech and language centers in many cases of prelingual deafness. [5,6] However, successful cochlear implantation in prelingually deaf adults has been demonstrated, but it is still difficult to assess candidacy in such cases. [7]

Magnetic resonance imaging provides a tool for morphologic and functional imaging of these cerebral areas and connections. Further investigations will have to prove whether changes in the functioning of the central auditory pathway might become a selection criterion for cochlear implant candidates. We are currently conducting a fMRI study to investigate phonological representation in both postlingual and prelingual deafened people.

Another important topic of inner ear research is otogenetics. Genetic causes account for about half of all cases of prelingual hearing impairment. The remainder is attributed to environmental factors, such as premature birth, infections or exposure to ototoxic drugs.

But also these have been shown to have genetic associations: eg mitochondrial DNA mutations are thought to underlie aminogluco-side-induced deafness [8] and genetic factors that may influence susceptibility to noise induced hearing loss are being discussed. [9] It is estimated that mutation of any of several hundred genes can result in deafness and to date over a hundred genes and loci have been identified. The aim to protect, restore or regenerate auditory neural function has instigated developments in gene therapy for hearing loss and cell delivery to the cochlea. [10] The role of high resolution computer

tomography scanning (microCT) and high field magnetic resonance systems in the development and monitoring of such treatment will have to be investigated.

The short term effects of surgical mechanical trauma to cochlear anatomic structures as well as the delayed loss of neural elements due to inflammation and other induced cell death pathways after implantation and electrical stimulation have been under investigation for a long time. Nowadays the widened application of cochlear implantation, including children and people with residual hearing, has further increased the alertness to cochlear trauma. Scientific studies and clinical reports emphasize the need for the development of atraumatic electrode designs, altered surgical techniques and thorough training of cochlear implant surgeons. So far such studies have mainly been the domain of histopathologists. Scarce reports describe the use of dynamic videofluoroscopy to investigate device-specific insertion characteristics in isolated temporal bones. [11,12] Cone beam CT of isolated temporal bones has been proven to render similar information concerning the position of the electrode as histological analysis. [13] Recently the application of high resolution micro-CT has been shown to provide practically artifact free images of isolated temporal bones and implanted devices over their total length. [14] Based on such micro-CT images we have investigated cochlear anatomic features, likely contributing to insertion trauma described with current electrodes. These findings may lead to reconsiderations on electrode design in regard to size and flexibility. Now, the challenge of in vivo assessment of cochlear trauma has to be faced. The data presented in this thesis underscore the potential role of radiology in the evaluation of electrode designs and surgical techniques in large cohorts of patients and with correlations to psychophysical data. However, direct visualization of the osseous spiral lamina is still not possible with current imaging techniques. In this thesis we have shown that the size of the scala tympani can be estimated based on the cochlear size and the correct positioning of electrode contacts can be supposed on midmodiolar CT sections. Recently cone beam CT has been reported to be superior to MSCT for in vivo imaging of cochlear implants because of its very high resolution and lower radiation dose. Despite these advantages, also in cone beam CT migration to the scala vestibuli has to be inferred from the position of the electrode contact in relation to the cochlear wall. [15]

Radiologic preoperative assessment of cochlear implant candidates has to be developed further. Whereas the mastoid and middle ear anatomy and anatomic variants are generally reported to guide the surgical approach to the temporal bone, the cochlea is usually only commented on if diseased. However, detailed analysis of the cochlear

anatomy will allow for precise and individualized planning of the insertion depth. We performed ex vivo studies on microCT and CT images confirming interindividual differences in cochlear size and form. Although estimations of length and diameter become within reach, the process is very time consuming and the current resolution of clinical scanners will limit the in vivo application. Further refinements in image processing will be necessary to improve automated segmentation of the inner ear and simplify measurements. Once this is achieved individual optimization of cochlear implantation might improve the outcome of speech perception scores. Furthermore, stock-taking of interindividual differences in cochlear form and size may justify the development of patient-specific electrode arrays in the future.

References

1. Fayad JN, Linthicum FH Jr. Multichannel cochlear implants: relation of histopathology to performance. *Laryngoscope* 2006;116(8):1310-20.
2. Khan AM, Handzel O, Burgess BJ, Damian D, Eddington DK, Nadol JB Jr. Is word recognition correlated with the number of surviving spiral ganglion cells and electrode insertion depth in human subjects with cochlear implants? *Laryngoscope* 2005;115(4):672-7.
3. Teoh SW, Pisoni DB, Miyamoto RT. Cochlear implantation in adults with prelingual deafness. Part I. Clinical results. *Laryngoscope* 2004;114:1536-1540
4. Blamey P, Arndt P, Bergeron F, Bredberg G, Brimacombe J, Facer G, Larky J, Lindström B, Nedzelski J, Peterson A, Shipp D, Staller S, Whitford L. Factors affecting auditory performance of postlinguistically deaf adults using cochlear implants. *Audiol Neurootol*. 1996;1(5):293-306.
5. Teoh SW, Pisoni DB, Miyamoto RT. Cochlear implantation in Adults with prelingual deafness. Part II. Underlying constraints that affect audiological outcomes. *Laryngoscope* 2004;114:1714-9
6. Lee DS, Lee JS, Oh SH, et al. Cross-modal plasticity and cochlear implants. *Nature* 2001;409:149-150
7. Klop WM, Briaire JJ, Stiggebout AM, Frijns JHM. Cochlear implant outcomes and quality of life in adults with prelingual deafness. *Laryngoscope* 2007;117(11):1982-7
8. Bindu LH, Reddy PP. Genetics of aminoglycoside-induced and prelingual non-syndromic mitochondrial hearing impairment: a review. *Int J Audiol* 2008;47(11):702-7.
9. Konings A, Van Laer L, Van Camp G. Genetic Studies on Noise-Induced Hearing Loss: A Review . *Ear Hear*. 2009 Feb 3. [Epub ahead of print]
10. Hildebrand MS, Newton SS, Gubbels SP, Sheffield AM, Kochhar A, de Silva MG, Dahl HH, Rose SD, Behlke MA, Smith RJ. Advances in molecular and cellular therapies for hearing loss. *Mol Ther*. 2008 Feb;16(2):224-36.
11. Balkany T, Eshraghi AA, Yang N. Modiolar proximity of three new perimodiolar cochlear implant electrodes. *Acta Otolaryngol* 2002;122:363-369.
12. Roland TJ. A model for cochlear implant electrode insertion and force evaluation: results with a new electrode design and insertion technique. *Laryngoscope* 2005;115:1325-1339.
13. Husstedt HW, Aschendorff A, Richter B, Laszig R, Schumacher M. Nondestructive three-dimensional analysis of electrode to modiolus proximity. *Otol Neurotol* 2002, Jan;23(1):49-52.
14. Postnov A, Zarowski A, De Clerck N, Vanpoucke F, Offeciers FE, Van Dyck D, Peeters S. High resolution micro-CT scanning as an innovative tool for evaluation of the surgical positioning of cochlear implant electrodes. *Acta Otolaryngol*. 2006 ;126(5):467-74
15. Ruivo J, Mermuys K, Bacher K, Kuhweide R, Offeciers E, Casselman JW. Cone beam computed tomography, a low-dose imaging technique in the postoperative assessment of cochlear implantation. *Otol Neurotol* 2009;30:299-303



Summary

Cochlear imaging in the era of cochlear implantation

From silence to sound

Summary

Cochlear implants are a well accepted treatment for profound hearing loss or deafness and at the time of writing more than 120.000 patients have been implanted worldwide.

In the preoperative assessment of cochlear implant candidates imaging plays an important role to analyze anatomy and rule out pathology that might influence or prevent surgical access and the success of outcome in terms of speech perception. Postoperative imaging is usually done by means of conventional x-rays and allows for confirmation of intracochlear positioning and integrity of the implant. However developments in cochlear implant design, differences in surgical approach and broadening of treatment indications have raised new questions to radiologists, which were the subject of several studies described in this thesis.

In **chapter 1** a short historical overview of the treatment of hearing loss was given. Many years of research have culminated in the development of well functioning cochlear implants. The potential role of imaging in regard to cochlear implantation was described and an outline of this thesis was shown.

In **chapter 2** the value of multi slice computer tomography (MSCT) for postoperative imaging of cochlear implant patients was studied. A data acquisition protocol and a post-processing protocol was presented for optimal visualization of a HiFocus I electrode. Its role in the evaluation of operation technique and electrode design, its potential to improve optimization of the function of the implant and its possible contribution to assessment of cochlear trauma in individual patients was illustrated.

To study the possibility of broad implementation of postoperative imaging by means of MSCT in clinical practice its applicability was tested on different scanners of four major vendors. The results were presented in **chapter 3**: point spread function measurements showed that the inherent resolution of all 4 studied scanners suffices for detailed visualization of the intracochlear electrode array as long as the intercontact distance is minimally 0.70-0.98mm. Qualitative and quantitative measurements on a polymethylmethacrylate phantom containing a curved cochlear implant showed that an extended hounsfieldscale must be available in order to optimally display the implanted cochlea.

Chapter 4 described the application of the above mentioned imaging technique for the assessment of 2 different types of cochlear implants – Clarion CII HiFocus 1 without

and with a positioner - and the correlation of these findings to outcome measures. CT showed a smaller electrode contact-to-modiolus distance proximally as well as a deeper insertion depth in the patient group who received a CI with a positioner. This confirms that the aims of the perimodiolar design are met. Speech perception tests showed a steeper learning curve and significantly better results with the perimodiolar design.

Chapter 5 is a consensus paper presenting an objective cochlear framework that provides a good, consistent method for specifying cochlear anatomy and cochlear implant positioning. It resulted from 2 international, multidisciplinary meetings with leading scientist from the various fields of inner ear research as well as different manufacturers of cochlear implants. Existing cochlear coordinate systems and differences in approach between the subdisciplines were discussed and have led to a common 3-dimensional cylindrical coordinate system that uses the Cochlear View, the plane through the basal turn of the cochlea and perpendicular to the modiolus, as plane of rotation. The z-axis is placed through the center of the modiolus, with its origin at the level of the helicotrema. As zero reference angle, the center of the round window is used.

In **chapter 6** a CT-based cochlear coordinate system, which is easily applicable in a clinical setting, was introduced. This method was shown to enable individualized preoperative and postoperative assessment of cochlear implant patients in a consistent, reproducible manner. Comparison to existing coordinate systems, described by L Cohen et al. [1,2] and M Skinner et al., [3] reflected the common conceptual frame work of these methods. The method fulfilled the requirements set by the international consensus described in chapter 5.

Chapters 7-9 were focused on the imaging analysis of cochlear anatomy, in particular dimensions of the scala tympani and scala vestibuli. Chapter 7 described the development and validation of a method for 3-dimensional medical image exploration by means of an autonomous virtual mobile robot. This technique was then applied to micro-CT datasets of isolated human cochleae. Length measurements along the central path of the cochlea were comparable to manually obtained measurements. Cross-sectional measurements could be obtained after detection of the cochlear central path.

In **chapter 8** the concept of above described virtual cochleoscopy was applied to 8 isolated human temporal bones in order to analyze the 3-dimensional anatomy of the cochlear spiral. A non-continuous spiraling path was found with decreases and increases of elevation at distinctive areas. These findings were correlated to reports on cochlear trauma in the literature. The similarity between the reported intracochlear vulnerable

areas during implantation and the areas of altered steepness lead to the conclusion that the intrinsic cochlear morphology poses a potential risk for insertion trauma.

Chapter 9 studied whether cochlear dimensions could be obtained in image data sets of commercially available and clinically used computer tomography (CT) scanners. For that 8 isolated human cochleae, also studied in the previous 2 chapters, were scanned on a multi detector row CT according to the same clinical acquisition protocol as regular patients are. Based on the formerly described virtual cochleoscopy length and diameter measurements were performed in both micro-CT and CT images. Comparison to manual contouring measurements on the micro-CT datasets proved good estimations of the cochlear dimensions. Inter-individual differences in cochlear size were shown in agreement with reports in literature. This emphasizes the need for a clinical tool to provide information of cochlear morphology in cochlear implant candidates in order to enable interindividual tailoring of the choice of cochlear implant devices and operation technique.

In **Chapter 10** general conclusions are presented and the future role of imaging in the investigation of the auditory pathway by means of functional MRI, as a helpful tool for otogenetic research and in the assesment of insertion trauma is discussed. The potential of imaging to improve patient-specific preoperative planning is reflected upon.

References

1. Cohen LT, Xu J, Xu SA, Clark GM. Improved and simplified methods for specifying positions of the electrode bands of a cochlear implant array. *Am J Otol* 1996;17:859-865
2. Cohen LT, Xu J, Tycocinski M, Saunders E, Raja D, Cowan R. Evaluation of an X-ray analysis method: comparison of electrode position estimates with information from phase contrast X-ray and histology. 5th European Symposium on Paediatric Cochlear Implantation, Antwerp, Belgium 2000.
3. Skinner MW, Holden TA, Whiting BR, et al. In vivo estimates of the position of Advanced Bionics electrode arrays in the human cochlea. *Ann Otol Rhinol Laryngol Suppl* 2007;197:2-24

The background of the page is a complex, abstract pattern of thin, curved lines that create a sense of depth and movement. A prominent circular shape is visible in the upper left quadrant, partially obscured by the lines. The overall color palette is monochromatic, consisting of various shades of gray.

Samenvatting

Cochleaire implantatie is een goed geaccepteerde behandeling voor ernstig gehoorsverlies of doofheid en op dit moment zijn reeds meer dan 120000 patienten wereldwijd geïmplanteerd. Beeldvorming speelt een belangrijke rol in de preoperatieve evaluatie van kandidaten voor cochleaire implantatie: enerzijds voor de beoordeling van de anatomie, anderzijds om pathologie uit te sluiten die de chirurgische benadering bemoeilijkt of de uitkomst voor wat betreft spraakverstaan zou kunnen beïnvloeden. Postoperatieve beeldvorming gebeurt meestal met conventionele röntgenopnamen voor bevestiging van een goede intracochleaire positie zonder beschadiging van het implantaat. Echter, nieuwe ontwikkelingen in het design van cochleaire implantaten, verschillen in chirurgische techniek en uitbreiding van de indicatiestelling hebben nieuwe vragen opgeworpen. Deze vragen hebben geleid tot het uitvoeren van verschillende studies, welke beschreven worden in dit proefschrift.

In **hoofdstuk 1** wordt een kort historisch overzicht gegeven van de behandeling van gehoorsverlies. Vele jaren van onderzoek hebben uiteindelijk geleid tot de ontwikkeling van goed functionerende cochleaire implantaten. De potentiële rol van beeldvorming met betrekking tot cochleaire implantatie wordt beschreven en een overzicht van dit proefschrift wordt gegeven.

In **hoofdstuk 2** wordt de waarde van *multi-slice* computer tomografie (MSCT) voor de postoperatieve beoordeling van cochleair implant patienten aangetoond. Een acquisitie- en postprocessing protocol voor optimale visualisatie van een HiFocus I electrode wordt voorgesteld. De rol van MSCT voor de evaluatie van operatietechniek en electrode design, voor verbetering van de werking van het implantaat en de mogelijke bijdrage in de beoordeling van cochleair trauma in individuele patienten wordt geïllustreerd.

Ter evaluatie van de mogelijkheid tot brede implementatie van postoperatieve beeldvorming met MSCT in de dagelijkse klinisch praktijk testten we deze toepassing op verschillende *multislice* scanners van 4 grote merken. De resultaten worden gepresenteerd in hoofdstuk 3: "point spread functie" metingen tonen aan dat de inherente resolutie van alle 4 scanners voldoende is voor een gedetailleerde afbeelding van de intracochleaire electrode zolang de afstand tussen 2 contacten minimaal 0.70-0.98mm bedraagt. Kwalitatieve en kwantitatieve metingen op een polymethylacrylaat fantoom met een opgekruld cochleair implantaat laten zien dat een uitgebreide hounsfieldschaal noodzakelijk is voor optimale visualisatie van het implantaat en de cochlea.

In **hoofdstuk 4** wordt boven beschreven beeldvormingstechniek toegepast bij patiënten met 2 verschillende types cochleaire implantaten – Clarion CII HiFocus 1 zonder en met positioner – en gecorreleerd met maten van uitkomst. CT metingen tonen een kleinere afstand tussen electrodecontact en de modiolus proximaal evenals een diepere insertie in de patiëntengroep met positioner. Dit bevestigt dat het beoogde resultaat van een perimodiolaire ontwerp wordt bereikt. Spraakverstaantesten tonen een steilere leercurve en een significant beter resultaat met het perimodiolaire ontwerp.

Hoofdstuk 5 is een “consensus paper” waarin een objectief cochleair coördinatenstelsel wordt voorgesteld dat een goede, consistente methode voor beoordeling van de cochleaire anatomie en voor positionering van een cochleair implantaat oplevert. Dit is het resultaat van twee internationale, multidisciplinaire bijeenkomsten met vooraanstaande wetenschappers uit de verschillende gebieden van cochleovestibulair onderzoek alsook vertegenwoordigers van verschillende fabrikanten van cochleaire implantaten. De bestaande cochleaire coördinatenstelsels en de verschillen in benadering tussen de subdisciplines werden besproken en hebben geleid tot een gemeenschappelijk 3-dimensioneel cilindrisch coördinatenstelsel. De Cochlear View, waarbij de cochlea wordt afgebeeld in het vlak van de basale winding en loodrecht op de modiolus, wordt gebruikt als rotatievlak. De z-as loopt door het centrum van de modiolus met de oorsprong ter plaatse van het helicotrema. Het ronde venster dient als 0°-referentiehoek.

In **hoofdstuk 6** wordt een cochleair coördinatenstelsel geïntroduceerd dat gebaseerd is op CT beelden en dat eenvoudig toepasbaar is in een klinische context. Er wordt aangetoond dat deze methode individuele preoperatieve en postoperatieve beoordeling van cochleair implant patiënten op een consistente, reproduceerbare wijze mogelijk maakt. Vergelijking met bestaande coördinaatsystemen, beschreven door L Cohen et al [1,2] en M Skinner et al. [3], geeft het gemeenschappelijke conceptuele kader van deze methoden weer.

Hoofdstuk 7, 8 en 9 zijn gericht op de analyse van cochleaire anatomie met behulp van beeldvorming, in het bijzonder de dimensies van de scala tympani en scala vestibuli. In hoofdstuk 7 wordt de ontwikkeling en validatie van een methode voor 3-dimensionele medische beeldexploratie met een autonome virtuele robot beschreven. Deze techniek wordt vervolgens toegepast op micro-CT datasets van geïsoleerde humane cochleae. Lengtemetingen langs het centrale pad van de cochlea waren vergelijkbaar met manuele metingen. Cross-sectionele metingen konden verkregen worden na detectie van het cochleaire centrale pad.

In **hoofdstuk 8** wordt het concept van de boven beschreven virtuele cochleoscopie toegepast op 8 geïsoleerde humane binnenoren ter evaluatie van de 3-dimensionele anatomie van de cochleaire spiraal. Het resultaat toonde een niet-continue spiraalvorm met sterkere stijgingen of dalingen in bepaalde gebieden. Deze bevindingen werden gecorreleerd met literatuurgegevens over cochleair trauma. De overeenkomst tussen de gerapporteerde kwetsbare gebieden en de gebieden van verandering in steilheid leiden tot de conclusie dat de intrinsieke cochleaire morfologie regionale risico's op insertietrauma verklaart.

In **hoofdstuk 9** wordt onderzocht of cochleaire dimensies verkregen kunnen worden uit datasets van commercieel beschikbare en klinisch gebruikte CT-scanners. Hiervoor werden de 8 geïsoleerde humane cochleae die in de vorige 2 hoofdstukken onderzocht werden, op een MSCT gescand met hetzelfde acquisitieprotocol dat voor patiënten wordt gebruikt. Lengte- en diametermetingen werden uitgevoerd zowel op micro-CT-datasets als op CT-beelden met behulp van de eerder beschreven virtuele cochleoscopietechniek. Vergelijking met metingen na manuele intekening van de omtrek van de cochlea op micro-CT bevestigde goede schattingen van de cochleaire dimensies. De interindividuele verschillen in cochleaire grootte kwamen overeen met literatuurgegevens. Het is dus van belang om over een klinische tool te beschikken die informatie levert over de cochleaire morfologie zodat de keuze van een implantaat en operatietechniek kan worden toegesneden op een individuele patiënt.

In **hoofdstuk 10** worden algemene conclusies gepresenteerd en wordt de toekomstige rol van beeldvorming voor het onderzoek van de auditieve banen met behulp van functionele MRI, als nuttig instrument voor otogenetisch onderzoek en voor de beoordeling van insertietrauma besproken. Het potentieel van beeldvorming ter verbetering van patiënt-specifieke preoperatieve planning wordt belicht.

Referenties

1. Cohen LT, Xu J, Xu SA, Clark GM. Improved and simplified methods for specifying positions of the electrode bands of a cochlear implant array. *Am J Otol* 1996;17:859-865
2. Cohen LT, Xu J, Tycocinski M, Saunders E, Raja D, Cowan R. Evaluation of an X-ray analysis method: comparison of electrode position estimates with information from phase contrast X-ray and histology. 5th European Symposium on Paediatric Cochlear Implantation, Antwerp, Belgium 2000.
3. Skinner MW, Holden TA, Whiting BR, et al. In vivo estimates of the position of advanced bionics electrode arrays in the human cochlea. *Ann Otol Rhinol Laryngol Suppl* 2007;197:2-24

Curriculum vitae

The author of this thesis was born in Tienen, Belgium on August 4, 1970.

After finishing high school at the Onze-Lieve Vrouwecollege in Tienen (1988) she started medical studies at the Catholic University of Leuven, Belgium. Part of the practical training period was spent at hospitals in South Africa. She obtained her medical degree cum laude in 1995. In the same year she entered the radiology residency programme at this University (Prof Dr AL Baert and Prof Dr G Marchal). She became a certified radiologist in July 2000. Since October 2000 she is working at the Radiology department of the Leiden University Medical Center, the Netherlands (Prof Dr JL Bloem). In 2003 she spent a visiting fellowship in Head and Neck radiology with Prof Dr AA Mancuso at the University of Florida, school of Medicine, Gainesville, USA and Dr JL Weissman at the Oregon Health & Science University, Portland, USA. Upon return research projects were performed in close cooperation with the ENT department, which culminated in this thesis. Since 2004 the author is appointed head of Neuro and Head and Neck Radiology at the LUMC.

